UNIVERSITA' DEGLI STUDI DI NAPOLI "FEDERICO II"

DEPARTMENT OF CHEMICAL, MATERIALS AND PRODUCTION ENGINEERING (DICMAPI)

PHD IN "INDUSTRIAL PRODUCT AND PROCESS ENGINEERING"
XXXIII CYCLE

"ENGINEERING PATTERNED AND DYNAMIC SURFACES FOR THE SPATIO-TEMPORAL CONTROL OF CELL BEHAVIOUR"

Supervisor
Ch.mo Prof. Maurizio Ventre
Ch.mo Prof. Paolo Antonio Netti

Coordinator
Ch.mo Prof. Andrea D'Anna

PhD Student
Chiara Cimmino

January 2018 - May 2021

Table of Contents

Aim of the work **8**

1 Introduction * **10**

1.1 The process of cell adhesion 12

1.2 Cell response to static signals 14

1.2.1 Biochemical stimuli 14

1.2.2 Topographical stimuli 15

1.2.3 Mechanical stimuli 18

1.3 Influence of substrate geometry on cellular processes 19

1.3.1 Cell response to dynamic substrate engineering 21

1.3.2 Dynamic display of ligands 22

1.3.2.1 Photo-controlled presentation of ligands 24

1.3.3 Dynamic stiffness 27

1.3.3.1 Photo-controlled material stiffness 27

1.3.4 Dynamic Topographies 29

1.3.4.1 Azopolymers 29

1.3.4.2 Focused Laser Beam 30

1.3.4.3 Photo-controlled substrate topography 32

1.4 Nuclear structure and its role in mechanotransduction 34

1.4.1 Lamins 36

1.4.2 Chromatin assembly 37

1.4.3 YAP activity 39

1.5 Methods for cell mechanical analysis 40

1.5.1 Atomic force microscopy 42

1.5.2 Cell monolayer rheology 44

1.5.3 The magnetic twisting cytometer 44

1.5.4 Particle-tracking microrheology 45
1.5.5 Micropipette Aspiration 46
1.5.6 Microfluidic Chip 47
1.6 Conclusion 48
1.7 References 50

2 Cellular response on static surfaces 65

2.1 Introduction 65
2.2 Results and Discussion 66
2.2.1 Relationship between cell shape and FA assembly 68
2.2.2 Relationship between cell stiffness, FAs and stress fibres assembly 71
2.2.3 Relationship between cell shape and nucleus deformation 74
2.2.4 Cell Mechanics to different indentation 81
2.2.5 Correlation Plots 82
2.3 Conclusion 89
2.4 Experimental Section 91
2.4.1 General Materials 91
2.4.2 Sample Preparation 91
2.4.3 Micropatterning protocol 91
2.4.4 Plating of the cells 92
2.4.5 AFM for Sample Surface Characterization 93
2.4.6 Fixed-cell Staining 93
2.4.7 AFM for Cell Mechanics 94
2.4.8 Analysis of nuclear morphology and FAs Shape 94
2.4.9 Plotting cell/nucleus mechanical properties and Correlation Plot 95
2.5 References 96

3 Cellular response on dynamic surfaces 98

3.1 Introduction 98
3.2 Results and Discussion 100

3.2.1 Pattern Inscription on Azopolymer Substrates 101
3.2.2 Cell mechanic on Dynamic Topographic Patterns 102
3.2.3 Focal Adhesion Remodelling 106
3.2.4 Nuclear Deformation 111
3.2.5 Chromatin assembly 114
3.2.6 YAP and lamin A/C expression 122
3.3 Conclusion 130
3.4 Experimental Section 131
3.4.1 General Materials 131
3.4.2 Dynamic Sample Preparation 131
3.4.3 Micropatterning protocol 131
3.4.4 Plating of the cells 132
3.4.5 Dynamic Topographic Pattern Inscription 132
3.4.6 AFM for Sample Surface Characterization 133
3.4.7 Fixed-cell Staining 133
3.4.8 YAP and Lamins immunostaining 134
3.4.9 AFM for Cell Mechanics 134
3.4.10 Analysis of FAs and nuclear morphology and H3K9, YAP and Lamins fluorescence intensity 135
3.4.11 Correlation Plot 136
3.5 Reference 137
4 Modulation of cell shape 140
4.1 Introduction 140
4.2 Results and Discussion 142
4.2.1 Laser patterning 142
4.2.2 Control of actin network remodelling 144
4.2.3 Focal Adhesion Remodelling 146
4.2.4 Change in the cell mechanics 148
4.2.5 Nuclear Deformation 150
4.2.6 Influence of cell elongation on chromatin assembly 152
4.3 Conclusion and Future prospective 155

4.4 Experimental Section 158
4.4.1 General Materials 158
4.4.2 Dynamic Sample Preparation 158
4.4.3 Micropatterning protocol 158
4.4.4 Plating of the cells 159
4.4.5 Dynamic Topographic Pattern Inscription 159
4.4.6 AFM for Sample Surface Characterization 160
4.4.7 Fixed-cell Staining 160
4.4.8 AFM for Cell Mechanics 161
4.4.9 Analysis of FAs, cytoskeleton, and nuclear morphology 162
4.5 References 163

5 Conclusion 165

Aim of the work

Cell adhesion has a direct impact on focal adhesions (FAs) formation, cytoskeleton arrangement, cell contractility and nucleus shape, which altogether affect several cell functions including morphology, proliferation, migration, and gene expression[1,2]. Therefore, cell adhesion-cytoskeleton assemblies-cell contractility constitute a tripartite module in which changes in one element invariably induce alterations in the other thus affecting cell behaviour.

Most of the current knowledge of cell biology is based on the effects of soluble signals (drugs, small molecules, peptides, proteins, growth factors) on cell behaviour[3]. There are comparatively fewer studies aimed at investigating the effects of insoluble signals, in the form of topographical or mechanical stimuli, on cell functions[4]. Furthermore, as in vivo stimuli change in time and space producing a continuous stream of information to cells, the understanding of how cells integrate and response to dynamic stimuli is extremely interesting and currently absent.

Therefore, my goal was to implement the design concepts and fabrication technologies that allow the developing of engineered platforms capable of delivering spatio-temporal controlled stimuli to study the effects of dynamic signals presentation on cell morphology and mechanics. This work is so based on the evaluation of how the physical properties of the microenvironment, in particular the geometry and nanotopography of the cell substrate, affect the properties of the cytoskeleton assembly that in turn regulate the FAs formation, the polymerization of actin filaments and mainly the nuclear structures and mechanical properties. This study could find effective applications to expand stem cell populations or to guide a homogeneous differentiation or self-renewal in vitro for stem cell-based therapies. Additionally, the results concerning the effect of material signals in changing the epigenetic state could be exploited to describe abnormal nuclear morphology in various diseases such as progeria, cancer, fibrosis, and dilated cardiomyopathy. Moreover, patterned surfaces of prostheses could improve the device integration within the host by targeting the differentiation of specific populations possibly avoiding the use of biochemical supplements.

To take these issues, in **Chapter I**, the main known effects of soluble and insoluble signals on cell behaviour are reviewed, together with the applications of biomaterials as a cell culture platform. The focus will be on the influence of dynamic topographic patterns on cell response and the limitation of proposed static substrates. To conclude this chapter, a brief overview of the nuclear structure and the main methods to measure nuclear mechanical properties will be presented.

Subsequently, in **Chapter II** we focus on a fine evaluation of stem cell adhesion events in response to static micro- and nanometric topographic stimuli. An accurate investigation on how the material signals modulate the measurement of the cell's elastic modulus by altering the structural properties of the cell nucleus and the cellular adhesive contacts was performed. More specifically, the study was focused on how cellular confinement and the nanotopographic patterns dictate and define the FAs formation, spatial positioning and orientation, the formation and organization of actin fibres and the nucleus shape.

Once known the cellular response in static, in **Chapter III** we study the events of cell adhesion in response to topographic stimuli in a dynamic contest. More in details, once proven that dynamic surfaces can control adhesion processes at the subcellular level in time scales compatible with conventional cell cultures, we evaluate how distinct biological responses may occur on different time scales. Light-responsive materials have been particularly suitable for this purpose. In principle, by combining different light-sensitive switches reacting to different wavelengths we fabricate arrays of signals whose display could be controlled in an orthogonal manner, thus increasing the complexity of the system. By applying different materials and innovative imaging techniques we explore the cell-substrate interface and the mechanisms through which cell geometry regulates cell signalling. Subsequently, we wondered whether the exerted topographic signals and the resulting changes in nuclear morphology could have a direct effect on chromatin topology, condensation, and accessibility to stem cell transcription sites.

Finally, we observe that the field of dynamic platforms, realized through confocal microscopy, should potentially contribute to unveil complex biological events such as migration and cell shape changes. So, in **Chapter IV** techniques of manipulation of the living cells shape in real time by using a laser light trigger in a non-invasive spatio-temporal controlled way will be presented. This method has allowed the precise control of specific actin-based structures that regulate cell architecture, nuclear mechanics, and chromatin assembly. In conclusion the directions for future perspective will be summarized.

Chapter 1

1 Introduction *

Abstract: Materials surfaces displaying patterns of adhesive signals are powerful regulators of cell functions and fate. More specifically, micro- and nano-scale signals in the form of patterns of ligands or surface topographies affect focal adhesions formation and dynamics. These, in turn, modulate intracellular signalling pathways ultimately affecting chromatin assembly and gene expression, a process that is commonly referred to as mechanotransduction.

The current knowledge of cell-material signals interaction and reaction is based on static culturing platforms. In this contest, the substrates exhibit patterns of signals fixed in space, not time-varying. However, cells in vivo are usually exposed to time and space changing arrays of signals, which might be biophysical or biochemical. It is the way the cells integrate these dynamic signals that eventually dictate the cell's state. Advancements in fabrication technology and materials engineering have recently enabled the development of culturing platforms able to display patterns of biochemical and biophysical signals whose features change in time and space according to selected programs.

In this chapter, we first introduce the basic mechanism of cell-ECM/material interactions focusing on cell adhesion processes to provide basic guidelines to engineer bioactive platforms able to control cell behaviour. More in details, we present the technical aspects concerning the fabrication of platforms displaying micro- and nano-scale signals to control cell functions, such as adhesion, elongation, morphology, and differentiation. We discuss notable examples of cell interaction with static engineered platforms to provide insights into cell's reactions and responses to specific signal arrangements. Subsequently, we classify the platforms about the external physical-chemical stimuli necessary to actuate the spatiotemporal changes of the signal patterns. We focus on discussing the technical details and performance of dynamic platforms, particularly those in which the light signal determines their variation in time and space. Most of our knowledge on cell material recognition and response to biochemical/biophysical signals arises from studies performed in two-dimensions (2D). Although most cells live in a 3D context in vivo, it is still debated whether adhesion in three-dimensions (3D) is identical to a 2D environment or follows a different route. This notwithstanding, we prefer to focus our attention on 2D systems as the development of dynamic materials is recent and

mostly concerns planar surfaces. Specifically engineered materials proved to be very effective in controlling even complex aspects of cell behaviour including stem cell self-renewal, targeted differentiation, and morphogenesis. These examples have intrinsic usefulness as the outcomes could be exploited in applications such as drug screening, cell-based therapies, and tissue transplantation.
Finally, in the last part of this introductive chapter, we discuss the nuclear structure, its role, and the main techniques to measure its mechanical properties to better evaluate cells behaviour in response to different signals. We also compare the main methods and motivate our choice to use the Atomic Force Microscopy for the experimental section.

**This Chapter is part of a published review: C. Cimmino, L. Rossano, P. A. Netti and M. Ventre. "Spatio-temporal control of cell adhesion: towards programmable platforms to manipulate cell functions and fate".*

1.1 The process of cell adhesion

Cells continually interact with the culturing microenvironment, including material surfaces, through an array of receptors that enable perceiving different chemical/physical signals, such as roughness, hydrophobicity, stiffness, charge and mainly ligand density and distribution. The receptors involved in such a process of recognition are located on the cell membrane and these include the immunoglobulin family of cell adhesion molecules, cadherins, integrins, selectins, and proteoglycans, as well as non-integrin collagen, laminin, and elastin receptors[5,6]. Among these, the transmembrane, heterodimeric integrin receptors have been widely investigated and are recognized as key elements in providing stable adhesion and in initiating biochemical events that eventually affect cell behaviour. Adhesion complexes is the result of the binding of integrins to specific ligands available in the culturing environment. Integrins are constituted by α and β subunits. So far, 18 α and 8 β subunits have been identified that can combine to form 24 different receptors with different binding properties[5]. Combinations of α and β subunits determine the affinity of the heterodimer to a specific ECM ligand. The main types of ligands found in the ECM are laminin, fibronectin, and collagen. Different sequences have been identified to specifically interact with integrins. Among these the RGD, YIGSR, YKVAV, LGTIPG, PDGSR, LRE, LRGDN, and IKLLI were identified in laminin, RGD and DGEA, GFOGER in collagen I and RGD, KQAGDV, REDV, and PHSRN in fibronectin. Before binding to ligands, integrin dimers need to undergo a conformational change (the activation process), which improves affinity towards the ligands and enables the interaction with signalling molecules from the cytoplasmic side. After activations, integrins cluster together in discrete locations of the membrane close to the adhesive surface. According to the availability of ligands and stability of the integrin-ligand complex, the cluster may mature in focal complexes up to micrometric multiprotein entities named focal adhesions (FAs) (**Figure 1.1**). Proteins formed on the cytoplasmic side may stabilize the protein gathering and/or may act as a bridge with the actin cytoskeleton. Activated integrins can engage the actin fibres through cytoplasmic reinforcing proteins such as talin, vinculin and α -actinin. Cytoskeleton generated contractile forces promote FA maturation through a conformational change of cytoplasmic mechanosensitive proteins that modify their functions. For instance, vinculin, which mediates force transmission, becomes activated and more affine to other proteins upon stretching. Similarly, talin exposes cryptic sites that allow additional binding sites for vinculin when stretched by actin transmitted forces[7]. The mechanical coupling between the cytoskeleton and the external surface in contact with the cell enables the perception of biochemical

(ligand density and patterning) and biophysical (topographical and mechanical patterns) signals of the extracellular environment. These signals are then transmitted in the cell through FAs.

Besides fulfilling an important structural role as anchoring points, FAs are also important signalling centres. Several components of, or in intimate connection with, the FAs are important signalling proteins as kinases (FAK, Src) and GTPases (Rho, Rac). Mechanical forces exerted by the actomyosin machinery are transmitted to these proteins and this may alter their activity. This also acts directly on the nucleus because the actin cytoskeleton is connected to the nuclear envelope. Therefore, actin generated forces can deform the nucleus, thus causing a structural modification of the chromatin assembly as well as the accessibility of transcription factors, possibly, altering gene expression[8]. It should be evident at this point those elements affecting cell adhesion (ligand availability and patterning or the transmission of mechanical forces) with biochemical/biophysical signals embossed on material surfaces may enable the activation of intracellular biochemical events ultimately affecting cell behaviour. This process is set out as the material-cytoskeleton crosstalk[4].

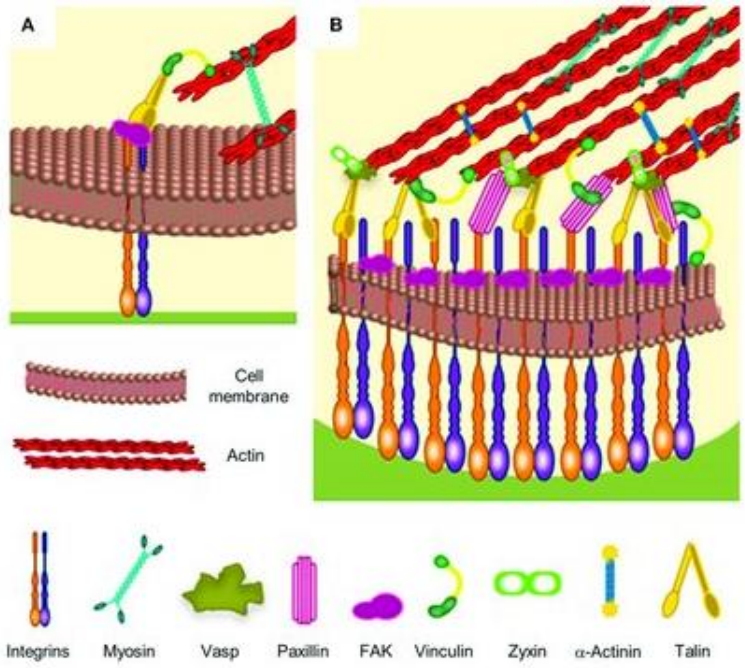

Figure 1.1: *Focal adhesion formation and maturation.* ***(A)*** *Nascent adhesions form the binding of integrins to extracellular ligands. Additional cytoplasmic components, such as talin, FAK and paxillin are recruited to stabilize the ligand-bound clusters. Myosin-generated forces promote conformational changes of talin, which exposes binding sites for vinculin. Stable clusters can grow further by addition of other integrins and cytoplasmic molecules, thus generating a focal complex and then a focal adhesion.* ***(B)*** *The multi-layered structure of a mature focal adhesion comprises proteins with different functions: signalling (integrins, FAK, and paxillin), force transduction (vinculin and talin) and linkers to the cytoskeleton (Vasp, zyxin, and α-actinin). From ref.* [9].

1.2 Cell response to static signals

Static surface engineering consists of ensuring that material features, fixed in space and time, can be tuned to influence FA formation and maturation hence affecting the activity of the signalling proteins or altering the structure and contractility of the cytoskeleton. Today, concepts as ligand density and patterning, topography, roughness, or material stiffness are regarded as crucial factors in affecting various aspects of cell behaviour. For this purpose, several strategies have been developed to control the biochemical and biophysical properties of the culturing material that mostly affect FA formation and growth.

1.2.1 Biochemical stimuli

Proteins or peptides containing cell adhesion motifs can be conjugated to material surfaces via covalent bonding or through physical interactions. Among these, the RGD sequence has been widely investigated[10,11]. Early studies on cell-material interaction aimed to define the optimal density of ligands to enable cell adhesion. From these, it first emerged that this parameter was highly dependent on the cell line. For example, in the case of fibroblasts, it was observed that a minimum RGD density of 1.0×10^{-15} mol/cm^2, corresponding to six ligands/μm^2 and a spacing of approximately 440 nm between peptide ligands, is required for them to diffuse onto glass surfaces, whereas a density of 1.0×10^{-14} mol/cm^2, i.e., 60 ligands/μm^2 and a spacing of 140 nm, is required to promote the formation of focal contacts and stress fibres[12]. Cell adhesion is a spatially discontinuous process occurring on the ventral side of cells, on a limited number of adhesion sites only. The uniform coating of material surfaces cannot address the important question about how individual ligands should be clustered and spaced to initiate the formation of adhesion complexes or promote their maturation. Therefore, micro- and nano-manipulation techniques should be implemented to precisely modulate ligand positioning, clustering, and spacing.

Block copolymer micelle nanolithography is one possible way to localise ligands with high precision over relatively large areas. This technique was exploited to evaluate how individual ligands should be presented, in terms of spacing and density, to promote solid cell adhesion. To this aim, Arnold et al. fabricated nearly perfect hexagonal arrays of 8 nm gold nanoparticles on glass or silicon substrates, in which interparticle spacing was precisely modulated in the 28 nm (high density) - 85 nm (low

density) range[13]. The authors found that adhesion formation required an interligand spacing, in the 58-73 nm range, whereas higher or lower ligand densities caused cells either to adhere too firmly or to remain round, with small FAs, respectively (**Figure 1.2**).

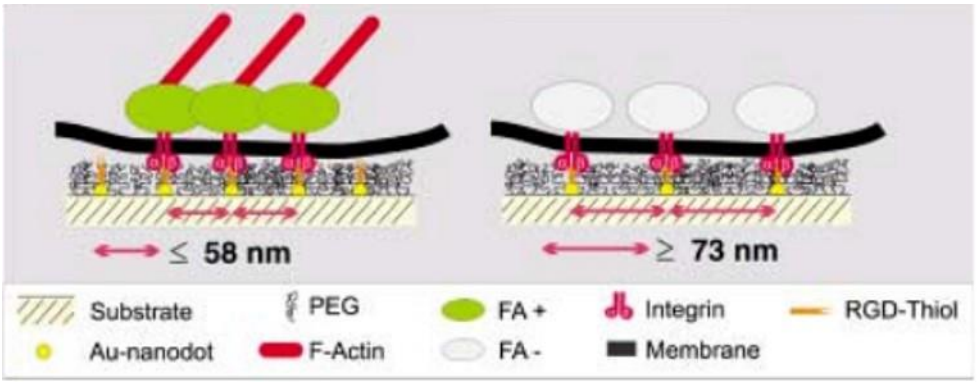

Figure 1.2: *Scheme of the nanopattern-mediated FA formation. A dot-to-dot distance below 53 nm enables integrin clustering, focal adhesion formation, and actin bundling, whereas a separation above 73 nm causes limited cell adhesion owing to impaired integrin clustering. From ref.* [13].

The aim of the ligand patterning is therefore to exert tight control on individual FA position and shape by creating surfaces characterized by submicron-scale zones conducive for FA formation and growth juxtaposed to zoned not allowing integrin engagement.

Since FAs are the pegs over which the cytoskeleton mounts and are therefore responsible for the transmission of forces to the external environment, a legitimate question is whether FA size correlates with the magnitude of contractile forces. Studies conducted in this regard, with the aid of traction force microscopy, reported that such a correlation between the FA area of large FAs (>1 μm) and traction force exists. Indeed, it was observed that FAs exert constant traction stress on the substrate, which is approximately 5.5 kPa[14]. Other reports, however, demonstrated that this correlation is cell line dependent as different cell types exert different traction forces and it is only valid in the initial stage of FA maturation and growth, whereas the stress exerted by mature FAs does not depend on FA size. Besides, FA tension is also position dependent as FAs close to the cell periphery exert higher and widely varying stresses than FAs that are close to the cell centre[15].

1.2.2 Topographical stimuli

In their natural environment, cells are surrounded by a complex microenvironment of defined structures such as fibrils, fibres, pores, and protrusions[16]. The ECM of various native tissues,

including bone, cartilage, nerves, bladder, or blood vessels, are consisted of micro- and nanoscale topographic patterns[17]. Current nano- and microfabrication techniques make it possible to fabricate structures on material surfaces capable of replicating those observed in natural tissues and organs with high precision. Such structured surfaces can be effective in controlling cell confinement and mainly the formation and growth of FAs. Different proteins adsorbed on the topographical pattern resulting in the formation of areas (such as ridge or pillars tops) easily accessible for FA formation, and areas (recesses such as grooves or pits) where the protrusion of the cell membrane cannot penetrate and then FAs cannot form. Optimization of topographical features, in particular topographical dimensions ranging from nanoscale to microscale, is the key strategy to obtain the best cellular performance for various applications in tissue engineering and regenerative medicine. To facilitate appropriate cell confinement, topographic patterns must be designed with dimensions comparable to those of cells (tens of microns). Micrometric patterns influence cell confinement, but do not allow precise control over FA formation and growth since adhesions can form spontaneously in various parts of ridges, grooves or pillars and grow in a way that cannot be precisely defined. In contrast, submicrometric patterns including pits, post, or gratings confine the growth of FAs and limit their formation to the accessible parts of the topographies, i.e. on the pillar top, in the interpit area or on the grid ridges. It is important to note that the accessibility/inaccessibility of certain material regions to cell membrane protrusions are not universal parameters but depend on the shape and size of the topographic feature.

Thorough studies providing what combinations of feature size, height and spacing promote or impair adhesion are still missing as it would require fabricating a very large number of substrates to test. Furthermore, not all cells recognize and respond to topographies in the same manner[18,19]. Notwithstanding this, experimental evidence suggests that critical feature sizes that dramatically affect adhesion exist irrespective of the particular feature type, i.e. pits, protrusions or gratings, and this suggest that possible common mechanisms of cell response to topographies might exist. For example, cells seeded on nanopillars display reduced adhesion when the feature height is above 70 nm, as this dimension seems to be critical in inhibiting integrin clustering[20]. Additionally, small pillar diameters (below 70 nm) and high interpillar spacing (above 300 nm) also reduced cell adhesion, whereas FA formation is restored when spacing is reduced to 70 nm[21,22]. Interestingly, this range of feature spacing is very similar to the values reported in other studies[23,24], so this dimensional range is identified as the upper limit for integrin clustering and FA formation. Micro- and nanoscale pillars and pit arrays can inhibit FA growth in specific directions, thus inducing confinement of both FA

width and length. However, directional guidance on FA growth cannot be readily implemented with these types of patterns.

Studies of cells cultivated on nanopits patterns demonstrated that the size and pitch of the nanopits are key parameters in governing cell adhesion. Arrays of nanopits of 120 nm in diameter 100 nm in depth and 300 nm in spacing arranged in an ordered square or hexagonal lattices confined FA growth in the interpit area, thus preventing extensive FA maturation (**Figure 1.3 A, 1.3 B**) [25].

Micro- and nanoscale gratings, constituted by parallel and alternating ridges and grooves, not only confine FA width, but they allow FAs to grow in a specific direction. Directional growth of FAs strongly affects cytoskeleton assembly as actin fibres are aligned parallel to the pattern direction. This causes the whole cell body to assume an elongated morphology and migrate along the pattern direction, a phenomenon usually referred to as 'contact guidance'.

Like what was discussed for pillars and pits, also in the case of gratings, whether FAs can form on the ridge top only or on the groove bottom depends on the feature geometry of the grating. However, FAs have rarely been observed on the grooves in microscale patterns with groove size 1, 2, or 5μm[26,27].Lamers et al. reported that ridges with lateral size <75 nm allowed integrin bridging of the grooves, therefore clustering of cytoplasmic adhesive proteins that lead to the formation of firm cell adhesions and a slow migratory behaviour. A change in the response of osteoblasts was observed when lateral spacing exceeded 75 nm. In fact, cells were highly aligned in patterns with ridges and grooves of 80 nm in width or on patterns with 50 nm ridges and 100 nm grooves. Conversely, no significant orientation was observed on the inverse pattern, i.e. 100 nm ridges and 50 nm grooves (**Figure 1.3 C**)[28]. To directly visualize FA formation on nanogratings and to investigate how FA confinement affected cytoskeleton assembly, Natale et al. transfected preosteoblasts with plasmids encoding fluorescent paxillin and actin[29]. In the early adhesion events, cells cultivated on parallel arrays of 700-nm wide, and 250-nm deep ridges and grooves formed adhesion complexes randomly and expressed thin actin filaments that did not display a common orientation. However, actin bundles directed in directions different from that of the pattern terminated with single or multiple adhesions that were located on consecutive ridges. These were not able to bridge the gap between ridges to form a single adhesion unit and appeared as a discontinuous and unstable adhesion. They rapidly collapsed under the effect of actin-generated forces, whereas FAs connected to actin bundles oriented parallel to the pattern direction were able to grow and form stable adhesions along the pattern. Actin fibres, nearly parallel to the pattern direction and terminating with dashed adhesion, reoriented along the pattern direction upon contraction. FA remodelling favoured the permanence of an orderly array of

fibres parallel to the pattern direction while the fibres not oriented along the pattern disappeared within few hours post-seeding.

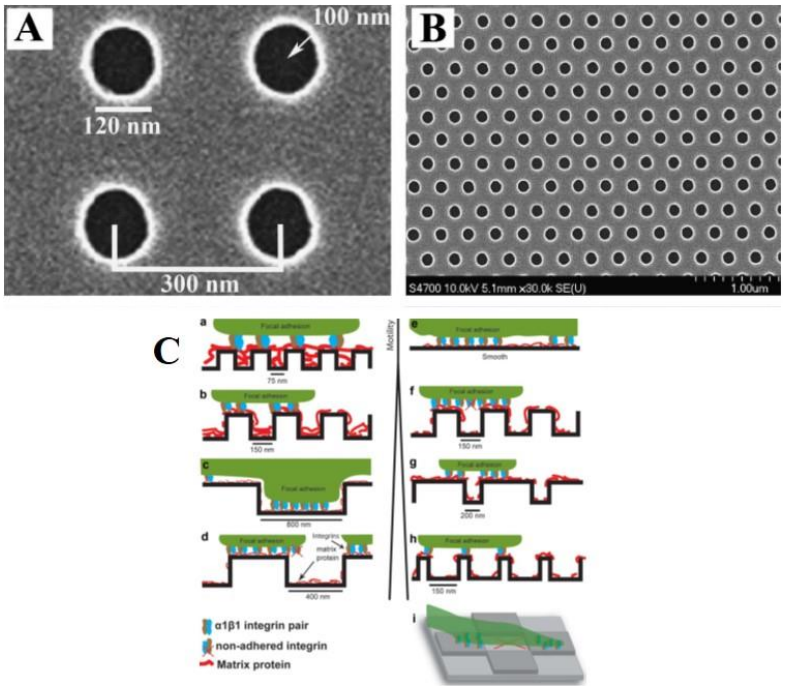

Figure 1.3: *Arrays of nanopits on poly(carbonate) substrates produced by electron beam lithography and injection moulding. Nanopits and interpit dimensions in ordered* ***(A)*** *nanopit arrays,* ***(B)*** *hexagonal arrays. From ref.*[25]*.*
(C) *Hypothesized models to explain the role of focal adhesions and matrix proteins in the response of osteoblasts to groove width and ridge-groove ratio. From ref.* [28]*.*

1.2.3 Mechanical stimuli

In addition to the topography, also the mechanical properties of the substrate, more specifically the stiffness or compliance, strongly impact FA formation, growth, and turnover[2,6].

Different studies confirm that cells on rigid materials (plastics, highly crosslinked elastomers, stiff hydrogels) express long, and wide FAs connected to well-defined actin bundles. Conversely, cells on compliant substrates (scarcely crosslinked elastomers or soft hydrogels) possess punctuate and highly dynamic FAs and a destabilized cytoskeleton[9]. The molecular mechanisms underpinning cell recognition of stiffness are not thoroughly clear as some evidence suggests that different stiffness leads to differences in anchoring densities of proteins, whereas other authors report that cells react to changes in stiffness independently from ligand anchoring[30,31]. However, the extent of contractility generated on either soft or stiff substrates differently activates mechanotransduction events at FA or nuclear level, ultimately affecting cell functions and fate[1].

Various types of platforms have been specifically engineered to investigate the cell sensing and response mechanisms toward stiffness. Among these, hydrogel platforms have been particularly useful for this purpose owing to their simplicity of chemical functionalization and tunability of the cross-linking density. For instance, polyacrylamide (PAM) hydrogels were employed to study cell adhesion, migration, and differentiation in experimental conditions in which stiffness could be varied in ranges like those measured in natural tissues. Notably, cells are likely to exert higher forces on stiff substrates[32]. For this purpose, mature and stable focal adhesions are observed on rigid gels, whereas shorter and more dynamic complexes are observed on soft gels. The cytoskeleton is weakly assembled in the cytoplasm, being predominantly cortical when cells are seeded on soft gels, while on stiff gels larger and well-defined bundles are observed. This behaviour strongly affects the cell mechanical forces that in turn have a large impact on cell proliferation and migration. Higher proliferation rates have been observed on stiffer gels[33]. Moreover, cells migrate with higher speed on soft gels while they are more stationary on stiff substrates[34]. However, these phenomena are strictly related to the culturing conditions and cell types[35]. Interestingly, cells cultured on gels or substrates presenting gradients of stiffness migrate preferentially from the soft to the stiff region, a phenomenon referred to as durotaxis[36].

1.3 Influence of substrate geometry on cellular processes

Cell size and shape are known to affect cell activities such as cell survival, growth, and differentiation[37]. By establishing cell geometry, it is possible to regulate their physiology but the exact biophysical mechanisms that translate changes of the cell geometry into alterations in cell behaviour remain largely unresolved. Using a variety of innovative materials and techniques, it has been shown that cell geometry regulates cytoskeletal contractility, cell stiffness and lipid assembly within the cell membrane. These biophysical changes trigger biochemical signalling events that can also influence stem cells differentiation. In this regard, von Erlach and co-workers studied the behaviour of human mesenchymal stem cells (hMSCs) grown on micropatterned surfaces with fibronectin islands of different geometry (triangular, square, and circular) but with identical surface areas[38]. Cells adhered to fibronectin and showed distinct morphologies and therefore cytoskeletal dispositions according to the geometry of the underlying island (**Figure 1.4 A, B**). Fluorescence intensity heat maps of F-actin and myosin IIa highlighted differences in cell contractility corresponding to different shapes (**Figure 1.4 C**). Analyses of the compliance of living cells performed with atomic force microscopy (AFM)

revealed differences in shape-dependent stiffness. More in details, triangular and square cells appeared more rigid than circular cells.

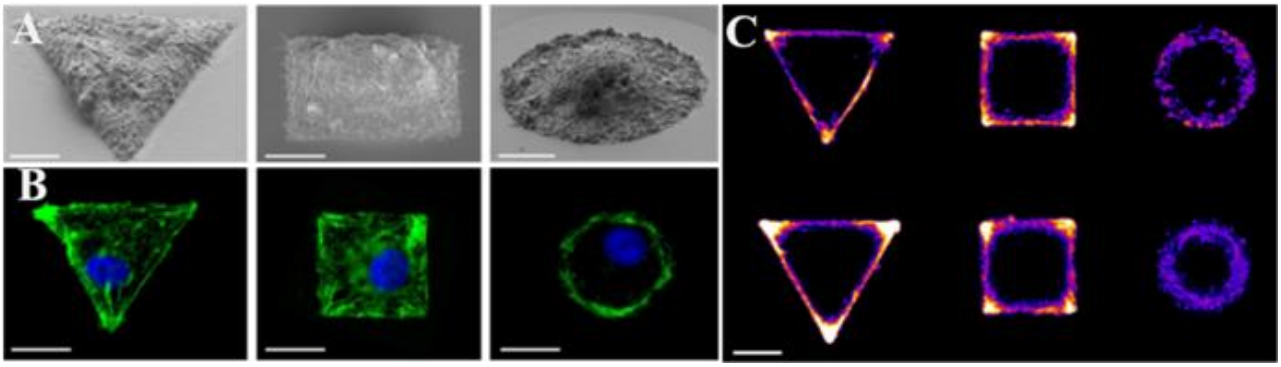

Figure 1.4: *Cell geometry induces changes in cytoskeletal arrangement and cell contractility.* ***(A)*** *SEM representations of hMSCs on micropatterned surfaces.* ***(B)*** *Immunofluorescence images of hMSCs. F-actin (green) and DAPI (blue).* ***(C)*** *Fluorescence intensity maps of myosin IIa and F-actin. Higher intensity is represented by a yellow/white colour. From ref.* [37].

In the same study, the cell geometry contribution to the regulation of stem cell differentiation was also observed. In fact, hMSCs cultivated in mixed adipogenic and osteogenic differentiation medium, on geometries implying low cytoskeletal contractility, differentiated mainly into adipocytes while cells seeded on geometries inducing high cytoskeletal contractility, differentiated into osteoblasts. It is evident that cell contractility does not depend on cell area only, but other geometrical characteristics may affect adhesion and contractility, ultimately influencing fate decisions. Adhesive islands of complex shapes, exhibiting both a global confinement and local (subcellular) curvatures, proved to exert a profound effect on cytoskeletal structures, polarity, and contractility, all of which can impact stem cell fate[39]. hMSCs switched fate decisions when cultivated on micropatterned adhesive islands displaying various areas, aspect ratios, and subcellular curvatures (blunt flower-shapes or pointed star-shapes)[40]. hMSCs on islands of intermediate area (2500 μm^2), which did not drive a specific commitment by themselves but rather generated a heterogeneous adipocytes/osteoblasts cell population, changed their commitment according to the specific shape of the micropattern. More precisely, high aspect ratio rectangular cells, or cell shapes with sharp corners, exhibited larger FAs, promoted a contractile phenotype and osteogenesis. Conversely, cells with blunt edges supported adipogenesis. Therefore, the geometric shape contributes to orchestrate the mechanics and chemistry of the signals that can direct hMSCs to the appropriate destinies.

While methods to control SC differentiation in vitro by modulating cell shape are nowadays well known, less is known about methods to promote SC self-renewal, i.e. a symmetric division in which the two daughter cells maintain undifferentiated characteristics. Understanding how to amplify SCs

in vitro while maintaining their differentiative potential would have a major impact on the effectiveness of cell therapies and tissue engineering approaches. Along these lines, Zhang and Kilian investigated the role of cell shape confinement in the retention of stemness markers[41]. The authors found that hMSCs cultivated on small (1000 μm^2) adhesive islands expressed higher levels of the multipotency markers endoglin and Stro-1 compared to cells cultured on nonpatterned surfaces that persisted also after cell removal from the pattern and culturing on plastic dishes. MSCs adhering on such substrates display a scarcely contractile phenotype and a round morphology that are features observed in in vivo niches. Therefore, maintaining a level of surface adhesion that does not promote excessive spreading and contractility is beneficial for promoting self-renewal. Conversely, increasing adhesion and cytoskeleton activity promotes differentiation. However, to what extent adhesivity or contractility should be modulated to direct SC fate decision (self-renewal or differentiation) is something that has not been fully clarified.

Geometrical constraints imposed on cells also affect local tensile stresses and subsequent alterations in the cytoskeleton and nucleus properties such as mechanical properties, chromatin assembly, nuclear lamin invaginations, and morphological assets[42]. In this regard, Damodaran et al. demonstrated that compression forces on fibroblasts reduced the actomyosin contractility, promoted depolymerization of apical actin filaments, and caused histones deacetylation, thus modifying chromatin condensation, reducing transcriptional activity, and inducing quiescence in fibroblasts[43]. Changes in the physical properties of the nucleus can be induced, in addition to the chromatin reorganization, by alterations in the mechanical properties of the nuclear envelope. For example, Lamin A/C levels in MSC have been observed to increase proportionally to myosin II because of increased substrate stiffness[44].

1.3.1 Cell response to dynamic substrate engineering

Synthetic materials whose chemical and physical properties do not change in time and space are often inadequate to provide a dynamic biophysical stimulation to cells and, therefore, are not able to capture certain aspects of the natural cell environment that regulate complex biological processes such as morphogenesis, growth, and tumorigenesis[45–48]. To investigate and control the natural cell functions, it is necessary to fabricate platforms that enable a fine control on the spatiotemporal presentation of biophysical and biochemical signals. Recent developments in materials engineering have led to a variety of approaches in which material properties can be dynamically and reversibly modified in

response to user-directed stimuli[49,50]. These stimuli that trigger the change might be exogenous, i.e., applied from the outside of the system, or endogenous, i.e., mediated by cells directly. Among the most frequently used exogenous stimuli there are temperature changes, light irradiation, and electromagnetic fields. There are comparatively fewer studies on endogenous stimuli, although being highly promising in terms of on-demand responsive systems. These include, for example, cell-mediated enzymatic reactions. Therefore, the dynamic presentation of signals is performed by responsive platforms specifically engineered to affect cell adhesion through bound biochemical signals or biophysical cues. These need to undergo significant configuration and/or location changes, such that cells can recognize the change and modify their behaviour consequently.

Ensuring specificity, i.e., the material response matches a specific stimulus thus avoiding nonspecific responses, is a fundamental aspect to choose the appropriate stimulus. For instance, light-responsive molecules react to irradiation at specific wavelengths. Similarly, polymers can be synthesized to display conformational changes at specific temperatures. Moreover, the material response to a stimulus may vary significantly depending on the exposure time to the stimulus, time of reaction to on/off stimulus switch, the timeframe in which the transition occurs. However, the stimulus provided must not affect cell viability directly or indirectly by inducing the release of toxic substances from the surface. In this contest, temperature or pH values can be altered only slightly, as too low, or high values are harmful to cell viability. Similarly, light can be used only in a limited range of wavelengths or intensities. Additionally, even in the case that the application of the stimulus is perfectly cytocompatible, the stimulus should not induce a change in cell response per se but rather the changes of the chemical/physical surface properties should be the main responsible for affecting the cell response.

In what follows we present consolidated strategies along with the recent developments for engineering synthetic substrates displaying signals dynamically. More specifically, we focus our attention on signals directly affecting cell adhesion events at different length scales: from a FA to a whole cell level. We, therefore, emphasize the role of dynamic display of biochemical (ligands), topographic and mechanical signals on cell adhesion, spreading, migration and differentiation.

1.3.2 Dynamic display of ligands

As discussed in the previous static section, cell adhesion is strongly affected by the presence of proteins adsorbed on or conjugated to material surfaces. For this reason, it is not surprising that many

dynamic platforms were engineered with the purpose of enabling/disabling the adsorption of adhesive proteins. This can be performed by changing specific chemical/physical surface properties such as wettability, hydrophobicity/hydrophilicity, and surface charge, or altering the composition of the surface through bond cleavage or formation, thus modulating the density of exposed ligands. Similarly, also the display of small adhesive peptide sequences through conformation changes has been a technique successfully implemented.

Self-assembled monolayers (SAMs) have been one among the first and perhaps most studied platforms to enable signal display dynamically. The reason resides in the well-defined chemistry of the surface, the ability to functionalize the surface after it is formed, its compatibility to micropatterning techniques, and transparency for facile investigation. These are molecular assemblies formed by the adsorption of molecular constituents from solution or the gas phase on a solid surface[51]. The molecular structure of the individual building blocks that form SAMs can be divided into three parts: a head that binds to a substrate (generally a metal); a central part acting as a spacer, whose chemical properties determine the interactions with the surrounding molecules and ultimately defining the packing and stability of the monolayer; a tail group which can be inert, bioactive, or susceptible to functionalization. Furthermore, SAMs can be disposed of additional functionalization or patterning after they are formed[52]. In this way, the material surfaces whose composition can be predetermined are characterized by chemical properties that can be considered uniform over relatively large areas. These are fundamental requirements to fabricate artificial platforms to study cell adhesion events or cell response to specific arrangements of ligands in a systematic manner. The most popular examples of SAMs used as cell culture substrates are thiol or silane headgroups derivatives on gold or silicon respectively[53,54]. Oligo (ethyleneglycol) SAMs were used as non-fouling protein surfaces and consequently cell repellent substrates. Alternatively, a broad variety of biomolecules, such as peptide fragments, proteins, antibodies, enzymes, and growth factors, have been used to bioactivate SAM surfaces on active groups present on the tail to promote and evaluate cell adhesion[55]. Juxtaposing protein repellent regions with bioactive ones is a desirable feature to study specific aspects of cell-material interactions. For instance, by conjugating selected adhesion ligands it is possible to study cell-receptor affinity consistently, but in a static conformation. Synthesizing polymer chains constituting the building block of the SAMs in a way that they include elements inducing conformation changes, reactive or labile groups whose activity can be modulated with either endogenous or exogenous stimuli, endow SAMs with dynamic or stimuli-responsive properties. Various types of stimuli can be exploited to perform dynamic change such as electric field, light variation, and temperature changes. In what follows we review the most notable examples of systems

engineered with the aim of controlling the display of adhesive signals dynamically focusing on the use of light stimulus in triggering the events.

1.3.2.1 Photo-controlled presentation of ligands

The use of light as a possible trigger for dynamic surfaces has attracted considerable interests because it enables to achieve fine control over the spatiotemporal changes of material properties. The light (i.e. laser beam) reaches the target immediately and allows to activate/deactivate molecules locally, with a microscale or submicron scale resolution. This is a considerable advantage concerning the temperature, which does not act locally, and to electric fields for which triggering changes of material properties locally could require the use of intermediate steps such as micropatterning or arrays of electrodes. The photochemical reactions can involve two distinct mechanisms: irreversible photocleavage and reversible photoisomerization. An early study of the irreversible photocleavage mechanism was conducted by Nakanishi et al.[56]. Using UV irradiation of a conventional microscope, the authors were able to emboss microscale patterns on alkylsiloxane based SAMs on glass, displaying a photocleavable 2-nitrobenzyl tail group. Coating the photocleavable SAM with bovine serum albumin (BSA) made the surface non-adhesive, thus preventing cell attachment. Exposing the substrate to a 365nm UV radiation caused cleavage of the tail groups and BSA release. Fibronectin supplemented in the medium readily adsorbed on the photocleaved regions only, facilitating adhesion. UV exposure can be performed directly, thus activating a wide area in a short time or can pass through a photomask. In this case, microscale features could be formed enabling to study cell dynamics of well-defined clusters or even of single cells. Following this procedure, HEK293 cells on a square array of 6 μm^2 adhesive spots formed FAs on the patterned islets only whereas they were able to stretch and spread across the non-adhesive areas. These data confirm that photomasking allows achieving sufficient spatial resolution to study cell adhesion at a FA level dynamically.

The same group exploited a similar technique to study cell morphology and membrane extension on the dynamic surfaces[57]. In this case, Pluronic 108 was used as a cell repellent backfill. NIH3T3 cells were first seeded on 25 × 25 μm^2 fibronectin-coated squares and then UV light was irradiated through a photomask to form either a 25 µm or 5 µm wide rectangle adjacent to the original square. In the case of square patterns cells spread over the entire new bioadhesive area, displaying actin bundles with FA oriented at various angles at their termini. Conversely, NIH3T3 cells displayed long protrusion with coaligned FAs and actin bundles when the narrow 5 µm wide stripe was juxtaposed

to the initial square (**Figure 1.5**). Photoactivated desorption of cell repellent compounds therefore possess the great advantage of allowing a greater level of spatial control of the adhesive properties of the substrate.

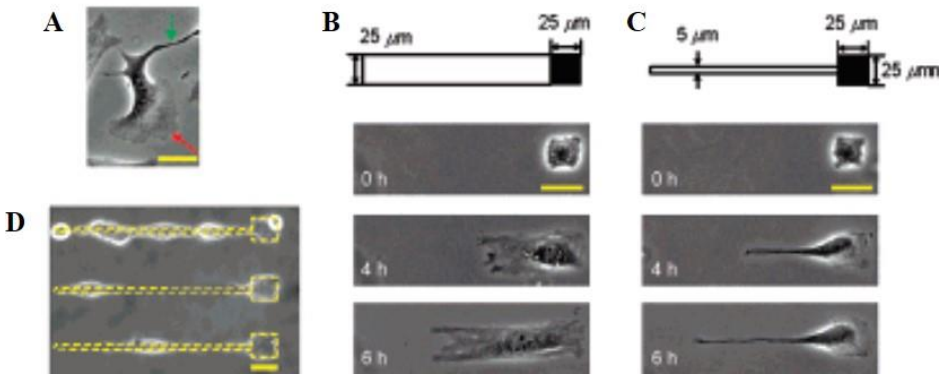

Figure 1.5: *Selective induction of two characteristic protrusions in NIH3T3 cells.* ***(A)*** *Stochastic extension of protrusions led by a lamellipodium (red) and by a filopodium (green) on a fibronectin-coated nonpatterned surface.* ***(B, C)*** *Selective induction of protrusions by illuminating a wide path (b, 25μm) or a narrow path (c, 5 μm) alongside the single cells. In upper figures, primary (black square) and secondary (white rectangle) illuminated regions are illustrated.* ***(D)*** *Cell adhesion onto a substrate where square array spots and paths (5 μm) were illuminated simultaneously. Yellow dotted lines represent the illuminated region. All scale bars represent 25 μm. From ref.* [57].

Cellular and subcellular resolution can be achieved using not only photomasks but also laser beams. For instance, pulsed UV lasers of sufficient power can be employed to ablate the protein-repellent coating of polyethylene glycol (PEG) on an otherwise adhesive substrate[58]. This enables the manipulation of the adhesive properties of individual cells with submicron resolution thus causing alteration in the intracellular architecture in real-time.

Besides the irreversible cleavage of photolabile groups, light irradiation may also drive conformation changes of photosensitive moieties. Displacement caused by the change in molecular conformation can be exploited to alter the chemical-physical properties of material surfaces. For example, spiropyran and azobenzene are two molecules extensively used for this specific purpose[59–61]. In the context of cell adhesion, Higuchi et al. coated glass plates with a copolymer of nitrobenzospiropyran and methyl methacrylate[62]. This copolymer can switch reversibly from a hydrophobic spiro conformation to a hydrophilic zwitterionic merocyanine isomer using irradiation of 365-nm UV light. The authors first demonstrated the reversibility of the transition (which required at least 24 hours in a dark environment) and then proved KUSA-1 cells detachment after 4-minute irradiation with light. Similarly, Edahiro et al. synthesized a photoresponsive cell-culturing surface constituted by a copolymer of N-isopropylacrylamide and nitrospiropyran as the photoresponsive element blended with poly(methyl methacrylate)[63]. CHO-K1 cells persisted on the UV-irradiated regions of the

material, whereas low-temperature washing detached cells. The system proved to be reversible as irradiation with visible light at 400-440 nm and 2h annealing at 37°C released the cells immobilized on the preceding UV exposure.

Concerning azobenzene, the light-induced cis-trans isomerization of its derivatives has been extensively used in biopolymers to change their structure dynamically. Exploiting this peculiar characteristic Auernheimer et al. were able to change the distance and orientation of RGD ligands and, therefore, the ligand availability thus affecting cell attachment on poly(methyl methacrylate)[64]. The authors used 4-[(4-aminophenyl)azo]benzocarbonyl as actuating element that was linked either close to the surface anchor or close to the ligand and these were separated by spacers of different length. Improved adhesion of MC3T3-E1 preosteoblasts was observed for all the spacers used when the azobenzene was in the trans configuration (i.e. after irradiation at 450 nm). Conversely, a general decrease in adhesion was observed when the azobenzene was in the cis state, which caused a spacer shortening and possibly a decreased accessibility to the ligand. A similar approach was pursued by Liu et al. who designed and fabricated mixed SAMs on gold, containing both an azobenzene unit terminated with an RGD peptide and a hexa(ethylene glycol) group that prevents cell attachment[65]. Changing the conformation of the azobenzene units through light irradiation caused the ligand to be either exposed on the surface (in the trans configuration upon UV irradiation) or flip back into the SAM (in the cis configuration after visible-light illumination). The authors demonstrated that the SAM reversibly enabled/impaired adhesion of NIH3T3 in a time frame of a few hours. Also, in this case, changes in the orientation and conformation occurring at the molecular level were sufficient to alter cell adhesion. Adhering cells can be detached by supplementing the culture medium with soluble GRGDS at pH 8.0. In this condition, the soluble ligand competes with the bound one. After detachment azomolecules could be switched to the cis isomer thus hiding the ligand and reducing cell attachment consequently. After irradiating with visible light, azomolecules revert to the trans form, which once again enables cell adhesion. In this case, reversibility is subjected to additional steps therefore this method cannot be considered fully reversible.

The ability of photoactivating cell adhesion via azobenzene moiety enables the fabrication of systems with a wide variety of surface properties represent a valuable approach to finely control cell adhesion and hence cell behaviour in vitro.

1.3.3 Dynamic stiffness

Materials whose mechanical properties can be changed dynamically represent unique platforms to investigate complex biological phenomena such as morphogenesis and wound healing. It is well recognized that the mechanical properties of substrates, in particular their stiffness, potently regulate cell proliferation and differentiation[66]. However, how changes in ECM mechanics accompany or anticipate physiological or pathological states is not entirely clear but developing artificial platforms capable of recapitulating the dynamics of stiffness changes in vitro would be important for the study of such events. Dynamic changes of substrate stiffness usually rely on degradation or crosslinking of hydrogels that can either proceed spontaneously or can be activated by external triggers such as light.

1.3.3.1 Photo-controlled material stiffness

A straightforward method to alter substrate stiffness consists of breaking crosslinks within hydrogel-based support. Reducing the number of crosslinks destabilizes the network while enabling higher molecular mobility. In this regard, Frey and Wang crosslinked a polyacrylamide hydrogel with a photocleavable 4-bromomethyl-3-nitrobenzoic acid group[67]. Upon UV irradiation (at 365 nm) gels softened by ~22% (from 7.2 to 5.5 kPa). NIH3T3 fibroblasts were very sensitive to the UV-induced softening as they rapidly contracted upon irradiation and then they exhibited a prolonged and gradual retraction. As light irradiation may be precisely directed in a specific part of the substrate, the system also enabled to investigate how cells respond to localized softening.

By exploiting photodegradation, Kloxin et al. aimed at addressing myofibroblastic differentiation in response to microenvironment softening[68]. Fibroblast to myofibroblast differentiation is a crucial step in wound healing. Wounds are highly dynamic environments (in terms of biochemical microenvironment, architecture, and mechanical properties) and today the role of biochemical/biophysical signals in governing the dynamics of healing is poorly understood. To this aim, valvular interstitial cells were cultivated on a PEG-based hydrogel containing photodegradable crosslinkers. The photodegradable hydrogel allowed to change moduli in the physiopathologic range within minutes after irradiation with UV light. Cells cultivated for 5 days on stiff (32 kPa) hydrogels displayed the characteristic phenotype of activated myofibroblasts, whereas cells cultivated on soft (7 kPa) gels were in quiescent form. However, the stiff-to-soft transition (3 days on stiff, followed by

2 days on soft) was sufficient to deactivate cells. Besides photodegradable softening, hydrogels can undergo photocrosslinking with subsequent stiffening. Guvendiren and Burdick developed a methacrylated hyaluronic acid (HA)-based gel whose stiffness can be increased through light-mediated radical polymerization[69]. hMSCs were cultivated on soft gels for selected time intervals, after which gels were stiffened by light irradiation. Cells quickly reacted to material stiffening by increasing the spreading area and the expression of contractile forces. Furthermore, early stiffening (i.e., cells exposed to a stiff environment for a long-time frame) promoted osteogenesis, whereas late stiffening promoted adipogenesis. These data demonstrate that timing associated with materials changes acquires a crucial role in defining cell functions. This might include the activation of pathological states for which changes in the ECM mechanics are frequently observed along with the progression of pathologies[70–72].

Not only the absolute magnitude of the stiffness affects fate decisions, but the way the mechanical stimulus is presented plays an important role in regulating the differentiation process. Along these lines, Yang et al. used a photodegradable polyethylene glycol di-photodegradable acrylate hydrogel functionalized with RGD to investigate whether stem cells possess a "mechanical memory"[73]. In other words, they studied if stem cells integrated in time the mechanical stimuli perceived by the microenvironment and made fate decisions based on such a mechanical memory. hMSCs were subjected to mechanical dosing, i.e. they were cultivated on stiff (~10 kPa) substrates for different time intervals (0, 1, 5 or 10 days) and then the substrate was softened down to 2 kPa. hMSCs supplemented with a small dose of mechanical stimulus (1 day) exhibited transient levels of genes involved in osteogenesis. Conversely, an irreversible activation of the differentiation program was observed when cells were cultivated for 10 days on stiff hydrogels before softening. The authors suggested that stem cells do possess a mechanical memory for which YAP/TAZ transcriptional coactivators act as mechanical rheostats since they persist in the nucleus, hence promoting osteogenesis if cells are continually exposed to stiff environments. More recently, hydrogels with reversible mechanical properties were fabricated through modular modifications of HA.

Therefore, hydrogels can be softened and then hardened (or vice versa) through sequential irradiation with adequate wavelengths.

1.3.4 Dynamic Topographies

All typical surface alterations that dynamically change their adhesive properties, including bond breaking/forming, capping/uncapping, conformation changes and protein adsorption/desorption, occur on the molecular level. By dynamic topography, we mean the ability to determine relieves of different shapes and heights, the coordinated movement of molecules, and the addition or removal of material on a micro- or submicrometric scale. To implement the development of the dynamic platforms, it is required to design specific chemical strategies, such as polymer degradation/polymerization or conformational changes, to enable this type of material transformation, which eventually gives rise to topographical features of the desired size in a reasonable time frame. Dynamic topographies act on cell behaviour by influencing adhesion complex dimension as well as their orientation and distribution. Such interactions, indeed, are translated in the generation of differential cytoskeletal stresses transmitted to the nucleus eventually altering gene expression[74]. However, it is necessary that the triggering stimulus preserves cell viability and does not compromise other cellular functions. Also in this section, we will focus on the achievement of dynamic topographies using the light stimulus.

1.3.4.1 Azopolymers

Light-responsive materials are usually classified according to the molecules that compose them to obtain their photoreactive properties. Among the most widely light response materials used like dynamic cell platform, there are azopolymers. These are polymers that contain an azobenzene group within the polymer structure. Azobenzene is an aromatic molecule formed by an azo linkage (N-N) connecting two phenyl rings. Its main characteristic is that it can interconvert between two isomeric states: a metastable cis form and a thermally stable trans configuration when irradiated with light tuned to an appropriate wavelength (**Figure 1.6**).

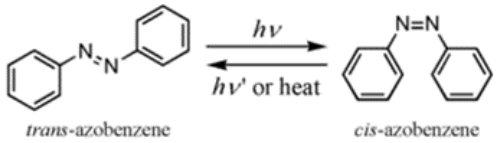

Figure 1.6: *Reversible structural transformations of azobenzene.*

The trans-cis photoisomerizations usually have picosecond timescales[75]. The reverse cis-trans isomerization can be driven by light or it occurs spontaneously in the dark owing to the thermodynamic stability of the trans isomer[76]. Alternatively, azobenzene molecules will thermally reconvert from the cis to the trans configuration with a timescale ranging from milliseconds to hours, depending on the substitution pattern and local environment.

Azobenzene chromophores can be oriented using coherent light. Their molecules preferentially absorb light polarized along their transition dipole axis (long axis of the azo-molecule). The probability of absorption varies as $\cos^2 \alpha$, where α is the angle between the light polarization and the azo dipole axis. The azo-molecules orientated perpendicularly to the light polarization will not absorb. The orientation due to polarized light is reversible; in fact, using a different polarization direction it is possible to modify the direction of the azo-molecules axis. Moreover, circularly polarized light and incoherent and unpolarized light randomize the chromophore orientations[77].

1.3.4.2 Focused Laser Beam

The azo-films exhibit a remarkable surface-mass transport on a micrometric and submicrometric scale when illuminated with proper wavelength laser light[78]. A single Gaussian laser beam can induce an azo-surface deformation, by aligning the azobenzene groups in the direction perpendicular to the polarization of the incident light. Modifying surfaces using this technique results advantageous in comparison to the other photopatterning techniques because:

- The Gaussian beam has a symmetric intensity distribution, which allows it to have a definite reference position[79].
- The intensity distribution and size of a Gaussian laser beam can be explicitly calculated according to the laser propagation theory[80].
- Its non-contact feature allows manipulating the surface of the polymer avoiding probable restraints and defects caused by contact methods (i.e. using a transmission mask).

The mass migration process depends on light polarization, intensity, and wavelength. This was widely verified by Brian et al. who tested the illumination of the polymer surface using a focused light spot. They observed that the focused beam was able to form a hole in correspondence to the centre of the laser spot. Moreover, they proved that the surface deformation was strongly influenced by the polarization of the laser beam. The spot carried out showed two lobes that piled up away from the high-intensity area along the polarization direction conversely these lobes did not appear when using

a circular polarized Gaussian beam (**Figure 1.7 A, B**). Furthermore, the polymer surface deformation induced by a higher intensity polarized Gaussian laser presented a central peak in the surface profile (**Figure 1.7 C**). The real mechanisms to elucidate the appearance of peaks at the centre of regions are not clear, however, this phenomenon may be due to the high intensity photothermal effects and photochemical reaction such as degradation. Photocrosslinking or photothermally induced crosslinking may also occur. These are plausible because the large quantity of energy absorbed from high laser irradiance would result in an increase in the temperature of the material during the exposure. Subsequently, it was proved that the focused laser beam allowed embossing linear pattern by moving the sample concerning the light polarization direction. The lateral size of the induced surface deformation was approximately equal to the diameter of the Gaussian beam (**Figure 1.7 D**)[79].

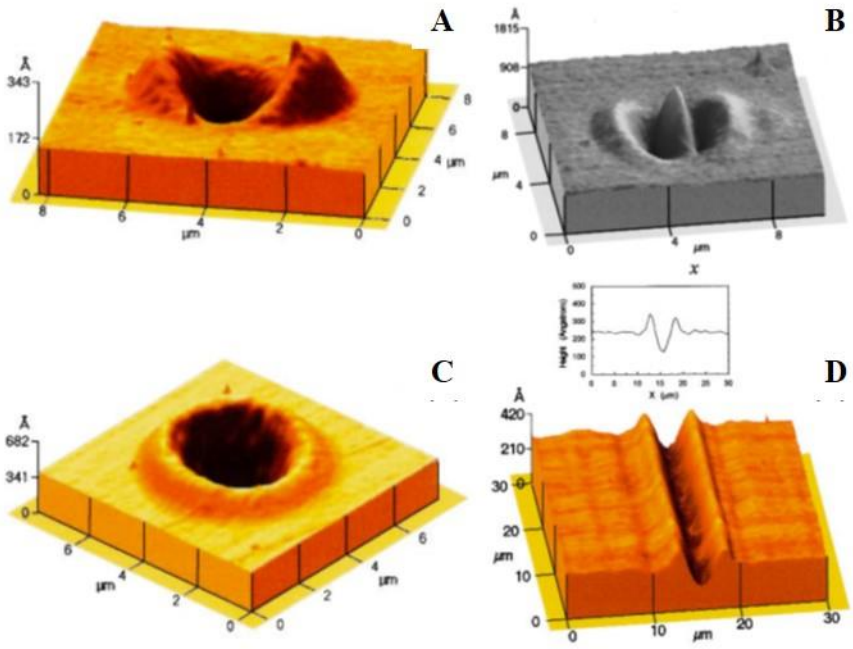

Figure 1.7: *Surface deformation induced by Gaussian beams with* ***(A)*** *low intensity linear polarization;* ***(B)*** *low intensity circular polarization;* ***(C)*** *high intensity linear polarization.* ***(D)*** *Surface deformation induced by a one-dimensional Gaussian beam. From ref.* [79].

The characteristics of the topographic patterns can be changed by adjusting the value of one or more of the following parameters: the thickness of the polymer layer, the temperature, the wavelength, and intensity of the laser beam. In conclusion, by using this technique, it is possible to produce topographic features of different shape on the surface by controlling the position of the sample concerning the focalized laser beam. The mass migration phenomenon can be appreciable by analysing the surface profile with appropriate tools.

1.3.4.3 Photo-controlled substrate topography

Material degradation induced by light irradiation enables embossing topographic structures with a high spatial resolution and regularity. In this regard, Kirschner and Anseth synthesized a photodegradable PEG-based hydrogel by coupling nitrobenzyl-based photodegradable acrylate to PEG-bis-amine and PEG macromer[81]. Irradiating the gel with UV light at 365 nm caused photolabile bond breaking and gel erosion. Using photomasks, the authors were able to direct erosion giving rise to topographic patterns whose depth was proportional to the irradiation time. Furthermore, by directing the laser beam of femtosecond multiphoton microscopes it was possible to emboss multiple patterns on the same gel. Dynamic patterning in presence of cells was observed by cultivating hMSCs on the top of a fibronectin-coated photolabile hydrogel. Microscale channels were imprinted on the gel which caused the cell reorientation and elongation. Afterwards, a grating of regular squares was produced by drawing lines orthogonal to the primary pattern. This restored a symmetric condition that induced cells to acquire a round shape. This platform proved to be highly versatile as it enables writing multiple patterns with different features on the same substrate. Additionally, the patterning procedure along with the hydrogel degradation products does not harm the cell. However, once sculpted hydrogel surfaces cannot acquire the initial shape. This may pose a severe limitation on the reversibility of the system.

Thanks to their ability to change conformation upon light irradiation, azopolymers have been used in various biological applications[82–84]. Azopolymeric patterned films proved to be biocompatible enabling the attachment of different cell types. This paved the way to use patterned light to modify the surface topography of films dynamically. An early attempt to inscribe a topographic pattern on an azopolymeric cell culturing substrate while preserving cell viability was reported by Barillé et al.[85]. The authors reported pattern inscription via irradiation with a two-laser beam interferometric pattern or through molecular self-organization induced by a single beam. PC12 cells reacted to the flat-grooved transition by elongating and aligning along the pattern direction and extending neurites. More recently Rianna et al. investigated the possibility of using a commercial polymer: the poly-(Disperse Red 1 methacrylate) (pDR1m) as a suitable substrate for reversible topographic patterns[86]. Preliminary tests to assess pattern stability under conditions comparable to those experienced during cell culture were performed. Patterns in the form of microgrooves or microgrids were inscribed on films by using an interference pattern of light. Cells were mostly round when cultivated on flat or grid pattern whereas they appeared to be highly elongated and aligned along the direction of linear microgrooved patterns. Circularly polarized light was subsequently used to induce the erasure of the

topographic pattern on pDR1m surfaces, causing a decrease in cell elongation. The FAs length showed no change in the write/erasure cycles, while the FAs orientation was very sensitive to topography. The authors of the same group further elaborated this concept by illuminating the pDR1m with a single-photon laser to study how space-time variations in topographic patterns affected the cell behaviour in real time[87]. A conventional confocal microscope was used to guide the laser beam path to emboss complex patterns on pDR1m thin films with submicrometric resolution. Fibroblasts cells responded to the dynamic patterns by altering their morphology and migration because of the cytoskeleton and focal adhesion reorganization. Furthermore, irradiating the substrate with an incoherent and unpolarized light of a mercury lamp enabled the erasure of topographic patterns on cell-populated pDR1m. The confocal technique, therefore, allows multiple pattern inscriptions and erasure on the same surface simultaneously, so that the isolated cells can be exposed to different topographies in real-time (**Figure 1.8 A**). This simple and versatile method can open the way to an investigation of the complex processes involved in the material-cell interaction (**Figure 1.8 B, C**).

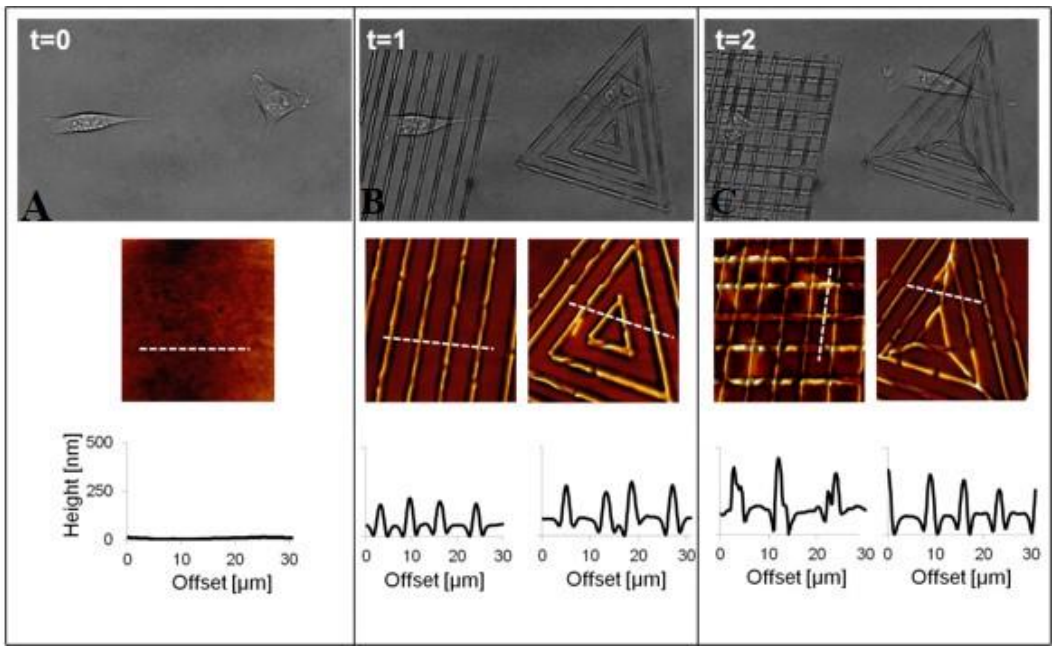

Figure 1.8: Space-time control of the pattern inscription. ***(A)*** *Transmission images of two non-interacting cells on pDR1m flat substrate (t = 0);* ***(B)*** *two different topographic patterns were inscribed using a 514 nm laser, with an inscription time of 30 s (t = 1);* ***(C)*** *after 45 minutes a second topographic pattern was overlapped to the primary one (t = 2). At the bottom of each image is a representative AFM scan and its cross-section profile. From ref.* [87].

More recently, Rossano et al. have exploited this confocal technique to study NIH3T3 fibroblast behaviour in response to dynamic circular topographic patterns. The authors observed that cells reacted to transition from flat to circulars topographies quickly and that patterns of circular ridges 2

μm wide and spaced of 10 μm (10C) most effectively affected cell shape and local orientation. Moreover, the changes in morphology also reflected dramatic changes in cell mechanics and cytoskeletal arrangements. Since stress fibres and FAs cannot grow in a bent fashion, circular topographies proved very effective in destabilizing cytoskeletal structures and hence in decreasing the mechanical properties of cells (**Figure 1.9**). Therefore, this method enabled investigate mechanotransduction events dynamically[88].

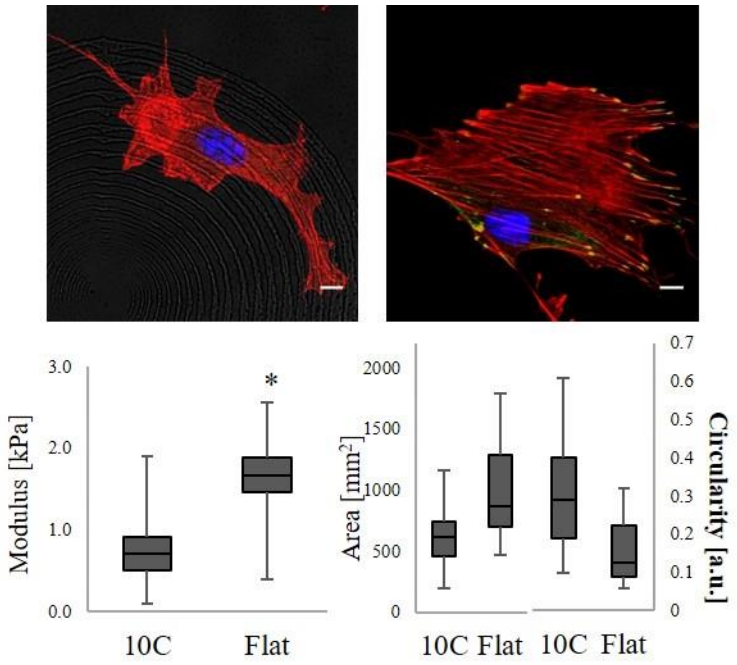

Figure 1.9: *Fluorescent images of fixed NIH-3T3 cells on* ***(A)*** *10C circular pattern or* ***(B)*** *flat surface. Box-and-whiskers plots of* ***(C)*** *the cells' elastic moduli and* ***(D)*** *projected cell area and circularity. Cell cytoskeleton is stained with phalloidin (red), focal adhesions are immunostained for vinculin (green) and nuclei are stained with draq-5 (blue). Scale bars are 20 μm. Asterisks indicate statistically significant difference ($p < 0.05$). From ref.* [88].

1.4 Nuclear structure and its role in mechanotransduction

In this thesis, great attention has been given to the nuclear structure and its mechanical properties when cultured on different micro and nanopatterns. Therefore, huge interest is the biological aspect of the nucleus and its role in the mechanotransduction process. The nucleus is one of the most rigid cell organelles physically connected to the cytoskeleton via lamins and the linker of nucleoskeleton and cytoskeleton (LINC) complex (**Figure 1.10**)[89]. It can be affected by significant shape deformation when mechanically disrupted, triggering multiple gene expression patterns. In fact, by altering cell

morphology, cytoskeletal stresses can reconfigure the spatial organization of chromosomes and may increase the accessibility of molecules that, in turn, affect gene expression to chromatin[90,91]. In this respect, the nucleus plays a fundamental role in cellular mechanosensing due to its ability to deform and react correctly to external mechanical cues guaranteed by the functionality of its load-bearing elements[92]. Recent publications have shown that the nucleus tensional state can be considered a sensor of both cell compression and cell stretching[93]. Indeed, when a cell is spatially constricted, the extent of the nuclear deformation and the consequent stretching of its membrane trigger remodelling of the actomyosin cortex, ultimately leading to an increase in cell contractility[94]. These events, in turn, induce the opening of nuclear pores and access to the nucleus of specific transcription factors (YAPs) that regulate mechanotransduction[95].

The growing evidence supporting the crucial role attributed to the nucleus in terms of mechanosensing has promoted the development of experimental tools capable of detecting cellular responses to controlled nuclear stresses and allowing the functional dissection of mechanotransduction processes[96]. The development of experimental tools capable of detecting cellular responses to controlled nuclear stresses and allowing the functional dissection of mechanotransduction processes represents a multidisciplinary field, combining several technologies in complementary research areas, such as materials science, cellular and molecular biology, and advanced imaging.

The investigation of the mechanical properties of the nucleus is a crucial factor because they change in response to specific states. For example, stem cells nuclei are highly deformable and contain dynamic chromatin[97–99]. Conversely, differentiated cells possess stiffer nuclei and a more stationary chromatin structure[100]. Moreover, the importance of evaluating nuclear mechanical properties has also been strongly observed in the pathological field and it was proven to play a crucial role in the spread of metastases, which cause about 80% of cancer-related deaths[101]. Indeed, during this process, cancer cells acquire a migratory phenotype and then overcome the structural barrier imposed by the surrounding microenvironment (i.e. other cells, the host tissue, blood vessels and the tissue to be invaded).

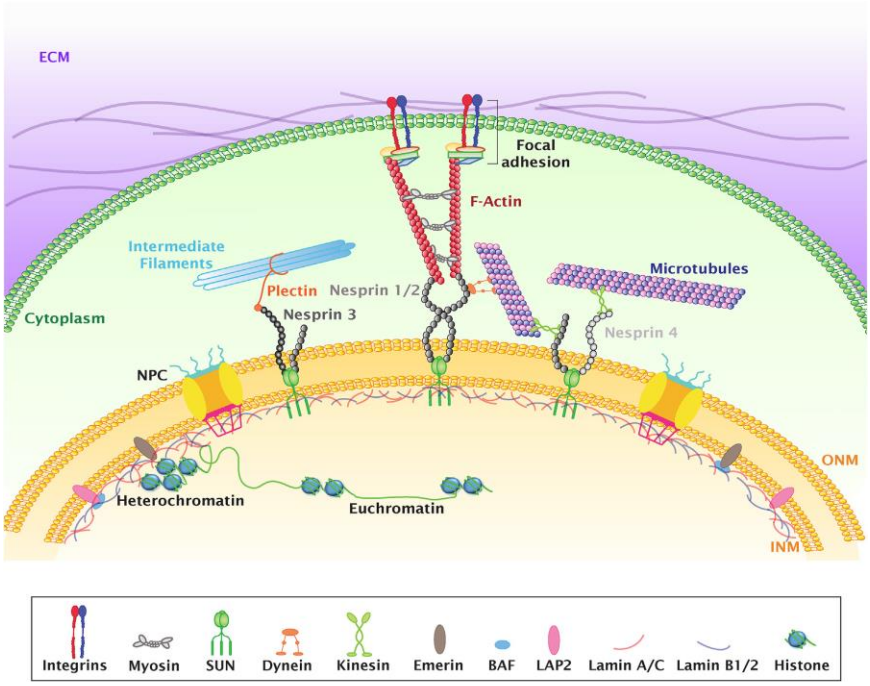

***Figure 1.10:**. Elements of the cytoskeleton and nucleus involved in mechanotransduction. Mechanical forces from the extracellular environment are sensed and transduced by receptors (e.g. integrins) and transmitted across the cytoskeleton network (e.g. actin filaments, microtubules, and intermediate filaments) into the nucleus via the LINC (linker of the nucleoskeleton and cytoskeleton) complex, thereby impacting chromatin organization, gene expression and cell function. Nesprins at the outer nuclear membrane (ONM) interact with cytoskeletal elements whereas Sad1/UNC-84 (SUN) proteins at the inner nuclear membrane (INM) interact with the nuclear lamina and chromatin, enabling force transmission between the cytoskeleton and nucleus. ECM, extracellular matrix; NPC, nuclear pore complex; BAF, barrier-toautointegration factor; LAP2, lamina-associated polypeptide2. From ref.*[102].

1.4.1 Lamins

The nuclear lamina is a dense fibrillar network sited inside the nucleus of most cells. It consists of nuclear intermediate filaments that form a stable structure within the nucleoplasm. It interacts with other nuclear envelope proteins, such as nesprin and SUN[103], chromatin[104] and some transcriptional regulator[105]. More in details, nuclear lamina means the structure comprising two components, lamins and nuclear lamin-associated membrane proteins. The lamins are type V intermediate filaments which can be categorized as either A-type (lamin A, C) or B-type (lamin B1, B2) according to the homology of their DNA sequences, biochemical properties, and cellular localization during the cell cycle. Lamins B1 and B2 have ubiquitously expressed products of independent genes (LMNB1 and LMNB2, respectively), essentials for early development[106,107]. In contrast, the A-type lamins are expressed mainly in differentiated cells, and generally, later in development[108,109]. The latter contribute to nuclear stiffness, integrity, and are involved in nuclear mechanotransduction processes. Therefore, the structural support to the nucleus is provided by lamins A and C that are predominantly relevant in physically connecting the nucleus to the cytoskeleton, allowing a force transmission

between them[110]. Thanks to the LINC complex, external forces applied to a cell are transmitted via the cytoskeleton to the nucleus, giving out nuclear deformations, which can alter chromatin structure and/or change the conformation of nuclear proteins, allowing the activation or repression of some genes[111,112]. In this regard, Swift et al. investigated the expression and phosphorylation state of lamins in response to changes in the mechanical microenvironment[44]. They found out that expression of lamins A and C increased with the substrate stiffness, both in vivo and in vitro. Moreover, softer substrates, corresponding to lower cytoskeletal tension, elicited higher levels of lamin A/C phosphorylation, indicating a more soluble and mechanically weaker lamin network.

We can easily deduce from this experiment that the cells adapt the lamins expression and organization according to the mechanical microenvironment they feel. Lamin can also interact with proteins and chromatin affecting DNA replication, gene expression and chromatin modifications[113].

Another fundamental aspect is that Lamin-deficient cells have been found to be more sensitive to cytoskeletal forces developed during skeletal muscle cell migration and maturation, which caused the exposure of the genetic content to the cytoplasmic DNA nucleases[114]. Mutations in the Lamin gene are the main cause of disorders named laminopathies, which are characterized by the presence of cells with irregular shaped nuclei. Although at least 15 different types of laminopathies exist, which makes them the highest number of diseases related to a single gene mutation[115], it is still unclear how various Lamin mutations cause different, often system-specific, disease phenotypes leading to various muscular dystrophies, lipodystrophies, progeroid syndromes, and many more[116].

1.4.2 Chromatin assembly

Chromatin is a dynamic structure composed of DNA, RNA, and proteins, regulating the expression of the genetic material in the nucleus. During interphase, the chromatin is structurally loose to allow access to RNA and DNA polymerases that transcribe and replicate the DNA. The local structure of chromatin strongly depends on the specific genes present in the DNA. In this respect, regions of DNA containing genes actively transcribed, appearing less tightly compacted and closely associated with RNA polymerases are known as euchromatin, while regions containing inactive genes generally more condensed and associated with structural proteins are known as heterochromatin[117]. Therefore, heterochromatin plays a crucial role in driving the three-dimensional arrangement of the interphase genome, and in preserving genome stability by maintaining a subset of the genome in a silent state. The primary protein components of chromatin are histones, which bind to DNA and function as

"anchors" around which the fibres are wound. Histones are positively charged basic proteins, as they have many basic side-chain amino acids, particularly lysine and arginine. They interact with DNA, which is negatively charged due to the abundance of phosphate groups, to form structures called nucleosomes. Multiple histones, wrapped into a 30-nanometer fibre, consist of nucleosome arrays. Higher-level DNA supercoiling of the 30-nm fibre produces the metaphase chromosome during mitosis and meiosis.

Covalent addition of an acetyl group to the terminal ε-amino group on lysine side chains neutralizes that amino acid's positive charge. For histone residues, this reaction eliminates electrostatic bonds between histones and DNA, reducing the strength of these interactions[118]. The enzymes that contribute to histone acetylation are not highly specific enzymes; they can modify more than one amino acid residue. DNA is then relaxed at that specific point, allowing other proteins or enzymes to interact with it. This process can favour increased accessibility for transcription factors and RNA polymerases[119]. Conversely, removal of acetyl groups by histone deacetylases (HDACs) facilitates decreased chromatin accessibility, as found in heterochromatic regions[120]. Also, lysine deacetylation can do more than restore the positive charge on lysine. For example, deacetylation of histone H3 lysine 9 (H3K9) is a prerequisite for methylation of this residue, which then can serve as a binding site for the chromodomain of heterochromatin protein 1 (HP1), a key protein for the formation, maintenance, and propagation of heterochromatin[121].

In literature, different studies have demonstrated that material signals such as material stiffness, topographic reliefs, or patterns of ligands influence chromatin assembly and mechanics through cytoskeletal structures[44,122]. To gain better insight into the effects of cell shape and cytoskeletal organization on chromatin structure and gene expression, Li et al. cultivated hMSCs on microgrooved PDMS that controlled cell morphology and nuclear shape. The authors investigated whether shape changes affected histone deacetylation (chromatin compaction) activity and histone acetylation (chromatin relaxation)[123]. Cells cultivated on microgrooves exhibited an elongated morphology, reduced histone deacetylation activity, and increased levels of histone acetylation, more specifically histone 3. These results demonstrated that exogenous biophysical signals can be translated directly into biochemical signals within the nucleus.

Moreover, much experimental evidence showed that the cell shape strongly affects histone acetylation, telomere dynamics, and nuclear mechanics through the modulation of the adhesion-dependent actomyosin machinery [8,124,125]. For this purpose, Versaevel et al. forced cells to adhere on rectangular adhesive islands to mechanistically analyse the link between cellular and nuclear polarization. They found that changes in cell aspect ratio generate actomyosin mediated anisotropic

compressive forces acting on the nucleus that induce drastic changes in chromatin condensation and cell proliferation[126].

1.4.3 YAP activity

Yes-associated protein (YAP) is one of the regulatory proteins in the 'Hippo' signalling pathway (first described in Drosophila), which in turn plays a key role in cell proliferation and regeneration[127,128]. At the tissue level, YAP is essential for embryonic development[129,130], organ size control[131] and regeneration, while its downregulation leads to carcinogenesis or other diseases. For this reason, it is considered a potent oncogene, which is overexpressed in various human cancers[132–134].

A growing number of studies reveal that YAP plays a central mechanotransduction role in providing the transcriptional structure of the nucleus with information on the characteristics of the extracellular matrix. Much information is available on YAP's ability to respond to biochemical and mechanical signals[135,136] generated by the elasticity or rigidity of the extracellular matrix. Less information is available on the behaviour of YAP in response to topographic signals provided to the cells. The expression of YAP is generally assessed according to its localization (in the nucleus or cytoplasm). This mechanical regulation requires cytoskeletal integrity[137] and involves different cytoskeletal and adhesive structures: first, myosin, which, respectively, increase and reduce YAP nuclear localization[138], and second, the integrin adaptor protein talin, which unfolds under force and leads to YAP nuclear translocation[95]. Finally, the Linker of the Nucleoskeleton and Cytoskeleton (LINC) complex, the impairment of which decreases nuclear YAP concentration[139].

In response to mechanical stimuli, the amount of YAP protein present in the nucleus correlates with the stiffness of the extracellular matrix. When cells are placed on a soft matrix, cytoplasmic YAP levels increase, and the rate of cell proliferation decreases. Conversely, when cells are placed in contact with a rigid environment, cytoplasmic YAP protein moves into the nucleus and induces cell proliferation[140].

Moreover, YAP may or may not activate the transcription of genes responsible for cell division and apoptosis.

1.5 Methods for cell mechanical analysis

The numerous pieces of evidence highlighting nuclear contribution to mechano-regulation of cell behaviour associated with the rapid growth of bioengineering and materials science prompted the development of strategies to measure nuclear mechanics.

Cells in vivo are continuously subjected to mechanical forces, including shear, compressive, and extensional forces. In turn, mechanical forces play an important role in the regulation of the function and organization of cells, tissues, and organs. The cell modulus is considered a key factor to understand how cells sense these forces exerted by the microenvironment (neighbouring cells and the extracellular matrix)[141]. The cellular response can be viscous, elastic, or viscoelastic. Besides, the recent development of tools for measuring cell mechanics has revealed that changes in cell and nuclear mechanics are the emblem of many human diseases, such as metastatic cancer, cardiovascular disease, inflammation, host-microbe interactions in infectious diseases, and frailty in ageing[142,143].

Today, we can measure the mechanical properties of cells by different methods and we can observe that cell mechanics depends on a multitude of factors such as the level of mechanical stress and rate of deformation to which the cell is subjected, the geometry of the mechanical probe used in the experiments, the probe-cell contact area, the probed location in the cell (e.g., cell cortex, nucleus, lamella, or cytoplasm), and the extracellular context (monolayer of cells versus single cells, adherent versus free-floating cells, etc.). Nuclear mechanical properties (i.e., stiffness, elasticity, viscosity), although characterized through different technologies, are generally measured by analysing stress-strain curves generated through the application of controlled forces or deformations to the nucleus[144].

The most common methods to evaluate adherent cell mechanical properties are atomic force microscopy (**AFM**), cell monolayer rheology (**CMR**), magnetic twisting cytometry (**MTC**), particle-tracking microrheology (**PTM**), micropipette aspiration (**MA**) and microfluidic chip (**MC**). These follow very different operating principles from each other (**Figure 1.11**).

Wu and co-authors conducted an important study on the comparison between different technologies to measure cell mechanics, including AFM, MTC, PTM and CMR[145]. They measured the mechanical properties of the commonly used MCF-7 human breast cancer cells, cultured in the same environmental conditions in vitro. Among the methods tested in this study, AFM provides measurements of Young's modulus (E), whereas MTC, CMR, and PTM all provide measurements of the shear modulus (G). Comparing these different methods, the authors divided the resulting moduli into three different categories: small (produced from PTM), intermediate (produced from AFM with

dull probes, and MTC), and high (produced from AFM with a sharp probe and CMR). Similarly, Pennacchio et al. presented some of the main technological tools used to characterize and perturb the nuclear mechanical state to highlight the growing impact of advanced engineering and imaging techniques to explore the biological relevance of mechanophysical properties of the nucleus[146].

These studies do not cover the whole spectrum of cellular mechanical measurement methods today available. In this regard, several new techniques have recently been developed to measure cell mechanical properties at high speed (10-10.000 cells per second), such as microfluidic-based methods[147] and the optics-based non-invasive Brillouin microscopy method[148]. These methods potentially can provide new avenues to extend cellular mechanical studies to clinically relevant samples.

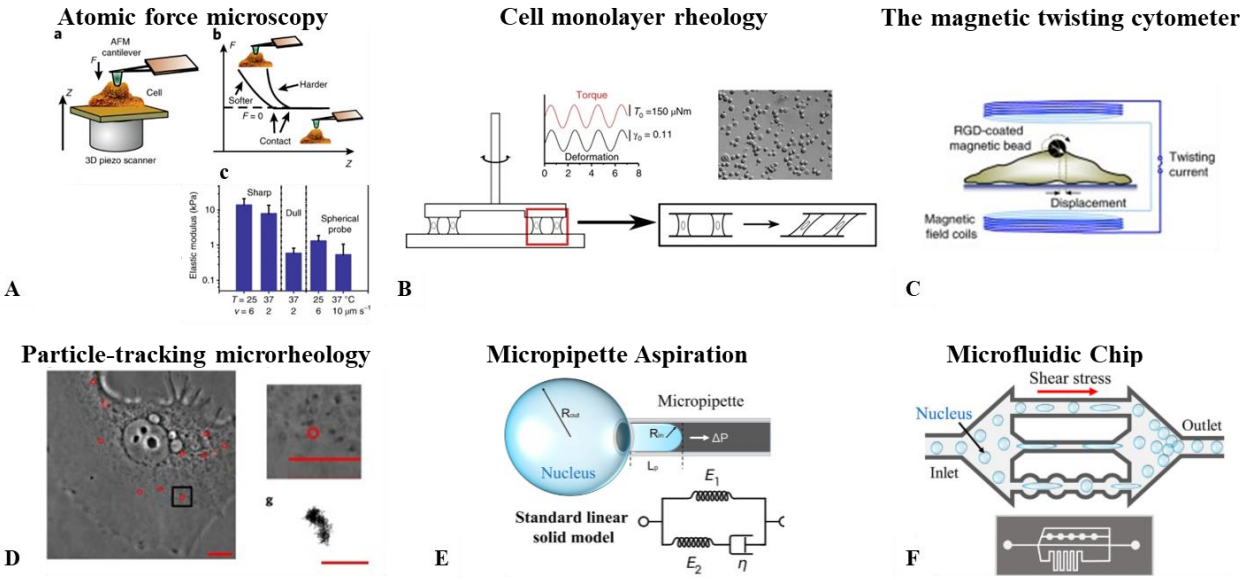

Figure 1.11: *Schematic of the experimental setup:* ***(A)*** *Atomic force microscopy, the most widely used method, can be used for mechanical testing and topological scanning using various cantilevers (with different tip). It enables precise nanoindentation measurements from which nuclear mechanical properties can be derived.* ***(B)*** *Cell monolayer rheology probes cells placed between two plates of a commercial rotational rheometer with a glass sensor and plate-ring geometry.* ***(C)*** *The magnetic twisting cytometer allow to explore force transmission across the cell membrane. It uses an Arg-Gly-Asp-coated ferromagnetic bead bound to the apical surface of the cell.* ***(D)*** *Particle tracking microrheology consists of injecting submicrometric fluorescent beads into the cytoplasm or cell nucleus by ballistic means and then measuring their spontaneous movements inside the cells.* ***(E)****Micropipette aspiration involves aspirating a nucleus into a micro-sized pipette and measuring the length of the nuclei extruded into it to determine the mechanical property.* ***(F)*** *Microfluidic-based platforms provide a high-throughput method for mechanical measurements; they can be customized depending on the need. From ref.* [145].

1.5.1 Atomic force microscopy

AFM-based indentation is commonly used to quantify the mechanical properties of adherent cells at subcellular resolution. It consists of a cantilever of calibrated stiffness that applies a force or deformation at a defined speed onto an adherent cell and, through laser deflection and detection by a photodetector, measures the corresponding resisting force from the deformation of the cell (**Figure 1.11 A**). It is equipped with a 3D piezo scanner that allows measuring x, y, and z displacements of the cantilever relative to the underlying cell.

Since the mechanical properties of cells are heterogeneous and vary considerably from cell to cell it is necessary to carefully choose the probe and the measurement settings by using the AFM. For example, usually higher indentation speeds resulted in higher elastic moduli and vice versa at lower speeds[149]. The choice of the tip is a crucial factor because measurements with different tips give rise to different elastic modulus due to the difference in the physics of the probe-cell contacts. Usually, when cells are indented with a larger probe, AFM measurements are less sensitive to local cell heterogeneity, and the elastic modulus is substantially lower[150]. To sum up, the mechanical properties of cells measured by AFM can differ more than tenfold, depending on the measurement parameters and the probed regions of the cells.

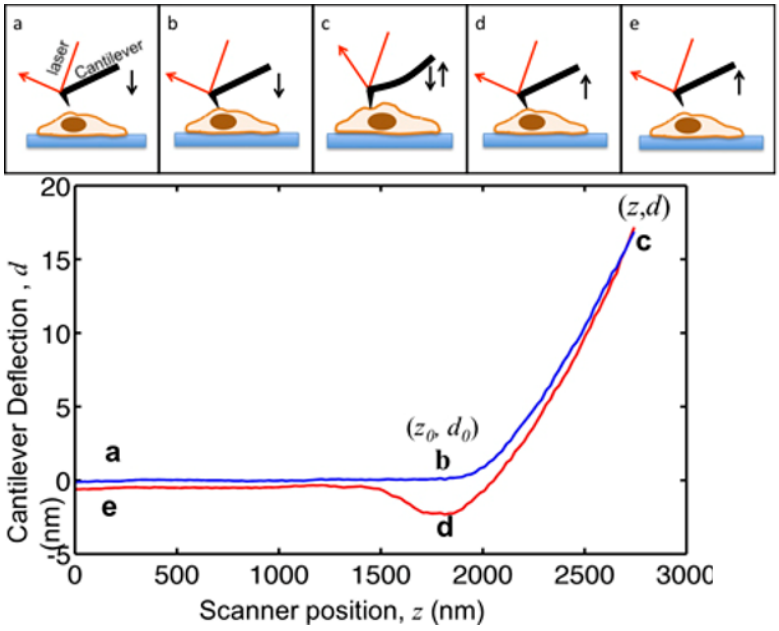

Figure 1.12: *Motion of AFM cantilever driven by the piezo scanner and plot of a representative force curve. From ref.* [151].

Force curves obtained from AFM show the cantilever deflection signal (**d**) and the vertical location of the cantilever (**z**) during the whole process (**Figure 1.12**). The first part of the curve appears as a flat line in the force curve because the tip is still too far away from the sample to perceive any interaction force. Then, the tip may experience observable attractive forces when it is closed to the surface. The tip results to be "in contact" with the sample when repulsive forces are first observed. Cantilever movement continues until a pre-set maximum force is reached (the furthermost point in the force curve), and then reverses the direction of travel and the cantilever is moved away from the sample[152].

More in general, the AFM offers a more efficient non-destructive way to quantitatively estimate multiple properties such as elasticity, viscoelasticity, plasticity, compliance, adhesion force and stiffness. It also provides an immediate overlap with a broad set of topographical information as a function of the specific operational mode used[153]. In this context, indentation represents one of the most interesting methods to investigate and locally measure mechanical properties. It is possible to distinguish between micro and nanoindentation according to the indenter dimensions. In such applications, the tip is pushed further towards the sample until a certain depth called penetration depth. The cantilever bending is monitored by the AFM photodetector system, and thus, the mechanical compliance of the tip-sample contact can be deduced. Cantilever deflection and tip penetration into the sample are usually measured with the Hertzian contact model. This theory is based on geometrical constraints of two spherical shapes in contact under a perpendicular load. Linear elastic deformation of both shapes is assumed with a quadratic pressure distribution along the area of contact. The model assumes that the surfaces in contact are continuous, smooth, and non-conforming; the strains implied in the indentation are small, and both the indenter and the sample can be described as elastic half-space. In the Hertzian theory, surfaces must be adhesionless and frictionless while stiffness homogeneously distributed along with the sample[154].

The AFM is also one of the most used methods now for the mechanical analysis of stem cells. This is mainly because many different techniques to evaluate cell mechanical properties require considerable cell manipulation and so they are not suitable for stem cells. For example, the cyclic application of forces to stem cells can trigger their differentiation, whereas single indentation using AFM involves less cell manipulation, avoiding unwanted differentiation. In this regard, Pillarisetti et al. used the force atomic microscope to show the different mechanical properties between undifferentiated and early differentiating mouse ESCs, not contributing to the differentiation with the measure's methods[155]. The authors observed that after only six days since the inducted differentiation

process started the cell stiffness increased almost doubling with respect to the undifferentiated cells regardless of the cell line.

1.5.2 Cell monolayer rheology

The cell monolayer rheology technique can measure the mechanical properties of a monolayer of isolated cells. It probes cells placed between two plates of a commercial rotational rheometer with a glass sensor and plate-ring geometry, which provides more accurate measurements in the regime of large shear deformations than the conventional plate-plate geometry (**Figure 1.11 B**)[156]. Fibronectin coating of the plates enhances cell adhesion. Cells form a sparse monolayer that can be observed through a microscope during measurements. The ring rotates around its symmetry axis, which leads to simultaneous shear deformation of the cells. Using this technique, at a constant oscillation frequency, MCF-7 cells showed a decrease in shear modulus with increasing amplitude of imposed shear deformation. Conversely, they showed an increase in the shear modulus of the cells with increasing oscillation frequency at a constant strain. Experimental data demonstrate that the elasticity of cells obtained by CMR was close to the elasticity measured by AFM with a conical probe. Adopting this method, it is possible to explore a broad range of cell responses not accessible using other current techniques. Fernandez and co-workers performed harmonic oscillation experiments and step shear or step stress experiments to reveal different viscoelastic regimes[156]. The evolution of the live cells under externally imposed cyclic loading and unloading is also investigated with this strategy.

1.5.3 The magnetic twisting cytometer

The magnetic twisting cytometer (MTC) has proved to be a useful tool for exploring force transmission across the cell membrane and for assessing cell stiffness and its changes.
MTC uses an Arg-Gly-Asp-coated ferromagnetic bead bound to the apical surface of the cell[157]. A controlled homogeneous magnetic field is applied to the cell via magnetic coils, which caused the bead to translocate and rotate (**Figure 1.11 C**). In this way, it is possible to measure the stiffness of cells based on the magnitude of the bead-cell area of contact, the magnetic field applied, and the displacement of the magnetic bead[158]. It is inviting to employ cell mechanical properties obtained with MTC to model cytoskeletal structure, to calculate the transit time of neutrophils through

capillaries, or to predict the deformation of endothelial cells under fluid shear stress. Such models and calculations, however, require reliable and accurate measurements of cell mechanical properties and a basic understanding of the meaning of these measurements. Therefore, it is very important to consider that part of the cell stiffening response may be due to bead inhomogeneity. For this reason, it is necessary to assess all measurement parameters in detail[159].

Recently, Wang et al. showed evidence that forces on the cell membrane can be transmitted directly into the nucleus, inducing structural changes of protein complexes in Cajal bodies by using the optical magnetic twisting cytometry (MTC) for force application and fluorescent resonance energy transfer (FRET) to monitor the dynamics and interaction of various Cajal body proteins[160].

1.5.4 Particle-tracking microrheology

Particle tracking microrheology (PTM) is a powerful technique to measure the mechanical properties of different cellular compartments[161]. This method consists of injecting submicrometric fluorescent beads into the cytoplasm or cell nucleus by ballistic means and then measuring their spontaneous movements inside the cells (**Figure 1.11 D**)[162]. Therefore, the PTM quantifies the local mechanical properties of living cells by monitoring the Brownian movement of individual microinjected fluorescent particles with high space-time resolution. The resulted trajectories are used to calculate the medium-square displacement that characterizes the dynamics of the probe particles.

The standard configuration for particle tracking video microscopy includes a charge-coupled device (CCD) camera connected to a microscope that acquires images of fluorescent molecules or spherical particles. This setup gives access to a wide range of timescales, from high-speed video rate to unbounded long time-lapse acquisition, particularly suitable for the study of biological phenomena.

PTM can probe the mechanical properties of living cells in experimentally difficult but physiological environments, including cells embedded within a 3D matrix, adherent cells subjected to shear fluxes and cells within a developing embryo.

More specifically, two different strategies could be approached: passive and active micro-rheology. In passive micro-rheology particles, trajectories are generated by spontaneous Brownian fluctuations. In active micro-rheology, instead, particle motion is triggered and controlled by external energetic sources such as light or magnetic fields. In these cases, cellular mechanical properties could be evaluated by both following particle trajectories in function of the applied force or by imposing controlled deformations (i.e., optical or magnetic tweezers). Furthermore, magnetic tweezers can also

be used on isolated nuclei to assess nuclear mechanical properties independently from the possible activation of cell surface receptors. In these conditions, a nuclear stiffening was observed in response to force application[163]. Recently, Wang et al. developed a multipole magnetic tweezers system able to finely control nanoparticle trajectories in 3D with a precision down to 0.4 μm. Interestingly, this innovative method allows the discovery of a spatial polarity of nuclear stiffness that correlates with the orientation of cytoskeleton actin filaments[164].

1.5.5 Micropipette Aspiration

One of the oldest techniques to characterize nuclear mechanics in both isolated nuclei and intact cells is micropipette aspiration (MA). By using this method, mechanical properties are evaluated by applying a controlled negative pressure (i.e., aspiration) to the nucleus and measuring its deformation (**Figure 1.11 E**). Pajerowski et al., applying this technique to the entire cell body, discovered a positive correlation between nuclear stiffness and progression of cell differentiation[98]. Moreover, they assessed how chromatin and Lamin differently regulate nuclear rheology and deformability. Subsequently, Neelam et al. employed micropipette aspiration to the whole cell to investigate the structural elements involved in the maintenance of nuclear shape and position in homeostasis[165]. They observed that elastic forces developed in response to mechanical perturbation and necessary to restore initial nuclear position and shape are mainly linked to the action of intermediate filaments network composed by vimentin, Lamin A/C, and SUN-domain proteins. Very recently Wintner et al. evaluated that aberrant nucleus mechanics can alter cell migration through narrow spaces in cancer metastasis and immune response and disrupt the nucleus mechanosensitivity[166]. Using the micropipette aspiration technique, they investigated the mechanical roles of lamins and chromatin to understand the implications of physiological forces on cells and nuclei. The authors presented a viscoelastic model that captures dynamic resistance across different cell types, lamin composition, phosphorylation states, and chromatin condensation.

However, it has been extensively proven that the accuracy of the measurements can be affected by variations in micropipettes, environmental fluctuations, and physiological cell deterioration[167].

1.5.6 Microfluidic Chip

A common limitation among the techniques discussed above is the low throughput, due to their inability to rapidly measure cell mechanical properties within large populations. Advancements in microfluidics have enabled researchers to integrate and develop novel high-throughput systems for cell and nuclear mechanical measurements (**Figure 1.11 F**). Some examples of microfluidic-based methods include deformability cytometry[168]. Using fluid-based deformability cytometry systems, it has been shown that mechanical property measurements can be derived from measuring the transit time through constrictions[169] or cell deformation after hydrodynamic stretching[170]. Another example of a microfluidic-based method includes a recent work in which authors have integrated the Brillouin spectroscopy with microfluidics to use light scattering as a parameter to measure nuclear mechanical properties, providing a non-contact and highly-sensitive method to detect nuclear stiffness[171]. As deformability capacity relates to stiffness and varies among different cell types, this parameter is used as a biomarker or predictor of disease status[98]. By using this technique, cancerous cells resulted softer than non-cancerous cells in several cancer models (e.g. pancreatic and bladder[172]), and more recently, tumour-initiating cells were found to be more deformable than cancer cells that do not display stem cell properties[173]. In addition to mechanical characterization, cell deformability can also be used as a parameter in microfluidic sorting devices to separate cells for further molecular characterization or drug screening applications[174]. Thus, these specialized microfluidic devices display great potential for high-throughput cell mechanical measurements, providing clinically relevant platforms for diagnostic and therapeutic purposes.

1.6 Conclusion

Adhesion mediated signalling regulates various aspects of cell behaviour including proliferation, migration, and differentiation. Cell adhesions have a direct impact on cytoskeleton arrangement, cell contractility and nucleus shape, which altogether affect gene expression and eventually cell functions. Therefore, cell adhesion, cytoskeleton assemblies and cell contractility are considered three closely related parameters in which changes in one element invariably induce alterations in the other thus affecting cell behaviour. Culturing substrates, scaffolds or gels proved remarkable effectiveness in finely modulating even complex biological events. Yet, these culturing systems are mostly known for statically displaying the signal. Static signal platforms have provided tremendous insights in understanding the optimal configurations of signals to be displayed to elicit a specific response. However, in the way they are conceived static platforms cannot be employed to address other relevant questions. As soluble biochemical signals elicit very different cellular responses according to their dose and on the way, they are delivered in time, do biophysical signals behave in the same way? How does the variable spatiotemporal presentation of biophysical signals affect cell behaviour? Does an optimal spatiotemporal presentation of bound signal exist to elicit a specific cell response in the most effective manner? Answering these questions may not only provide valuable insights for the engineering of more effective and versatile culturing systems but might aid in shedding light on intricate biological processes involved whenever modifications in the microenvironment occur, for example in tissue and organ morphogenesis or the development or progress of diseases. Dynamic platforms may certainly contribute to addressing these issues. However, many technical hurdles need to be overcome. First, a fine modulation of adhesion events and exerting a control on the dynamics of specific arrangements of FAs. Such a spatiotemporal resolution in the actuating elements of dynamic platforms has not been achieved yet. Second, dynamic surfaces have reached a level of performances that enables controlling adhesion processes at a subcellular level in time-scales that are compatible with conventional cell cultures. However, different biological response may occur on different time scales, i.e. adhesion take minutes to hours, whereas differentiation occurs in days or weeks. Some triggers are faster than others, but once they are turned “on” or “off” the whole system responds with its kinetics. Therefore, tuning the dynamics of the signal change to that of a specific biological phenomenon may require a careful design of the molecular switch or the integration of various switches. Furthermore, activating and deactivating signal exposure in a completely reversible manner is key central. Non-reversible or partially reversible systems might only partly recapitulate

the dynamic behaviour of the ECM or might not be entirely versatile. Creating complex spatiotemporal patterns of signals requires implementing signal display/conceal in a fast and effective manner. The uncontrolled presence of signal remnants may interfere with the intended signal presentation providing inconsistent results.

Literature data have provided compelling evidence that cell functions and fate are not dictated by a single signal type, but it is rather a complex interplay of multiple signals acting on different length- and time-scales that determines the final cell state[2,175]. To actuate different signal acting at different timepoints, specific switches must be engineered. Photoswitches might be particularly suitable for this purpose. Several molecules have been developed, for example the azoderivatives, whose response may fall within a broad range of wavelengths. In principle, by combining different light-sensitive switches reacting to different wavelengths it would be possible to fabricate arrays of signals whose display could be controlled in an orthogonal manner, thus increasing the complexity of the system. This, however, requires a sapient positioning of light-sensitive elements with non-overlapping absorption spectra.

1.7 References

1. Anderson, H. J., Sahoo, J. K., Ulijn, R. V. & Dalby, M. J. Mesenchymal Stem Cell Fate: Applying Biomaterials for Control of Stem Cell Behavior. *Front. Bioeng. Biotechnol.* **4**, (2016).

2. Dalby, M. J., Gadegaard, N. & Oreffo, R. O. C. Harnessing nanotopography and integrin–matrix interactions to influence stem cell fate. *Nat. Mater.* **13**, 558–569 (2014).

3. Yao, T. & Asayama, Y. Animal-cell culture media: History, characteristics, and current issues. *Reprod. Med. Biol.* **16**, 99–117 (2017).

4. Ventre, M., Causa, F. & Netti, P. A. Determinants of cell–material crosstalk at the interface: towards engineering of cell instructive materials. *J. R. Soc. Interface* **9**, 2017–2032 (2012).

5. Campbell, I. D. & Humphries, M. J. Integrin structure, activation, and interactions. *Cold Spring Harb. Perspect. Biol.* **3**, (2011).

6. Di Cio, S. & Gautrot, J. E. Cell sensing of physical properties at the nanoscale: Mechanisms and control of cell adhesion and phenotype. *Acta Biomater.* **30**, 26–48 (2016).

7. del Rio, A. *et al.* Stretching single talin rod molecules activates vinculin binding. *Science* **323**, 638–641 (2009).

8. Jain, N., Iyer, K. V., Kumar, A. & Shivashankar, G. V. Cell geometric constraints induce modular gene-expression patterns via redistribution of HDAC3 regulated by actomyosin contractility. *Proc. Natl. Acad. Sci.* **110**, 11349–11354 (2013).

9. Ventre, M. & Netti, P. A. Engineering Cell Instructive Materials To Control Cell Fate and Functions through Material Cues and Surface Patterning. *ACS Appl. Mater. Interfaces* **8**, 14896–14908 (2016).

10. Hersel, U., Dahmen, C. & Kessler, H. RGD modified polymers: biomaterials for stimulated cell adhesion and beyond. *Synth. Biomim. Polym.* **24**, 4385–4415 (2003).

11. VandeVondele, S., Vörös, J. & Hubbell, J. A. RGD-grafted poly-l-lysine-graft-(polyethylene glycol) copolymers block non-specific protein adsorption while promoting cell adhesion. *Biotechnol. Bioeng.* **82**, 784–790 (2003).

12. Massia, S. P. & Hubbell, J. A. An RGD spacing of 440 nm is sufficient for integrin alpha V beta 3-mediated fibroblast spreading and 140 nm for focal contact and stress fiber formation. *J. Cell Biol.* **114**, 1089–1100 (1991).

13. Arnold, M. *et al.* Activation of integrin function by nanopatterned adhesive interfaces. *Chemphyschem Eur. J. Chem. Phys. Phys. Chem.* **5**, 383–388 (2004).

14. Balaban, N. Q. *et al.* Force and focal adhesion assembly: a close relationship studied using elastic micropatterned substrates. *Nat. Cell Biol.* **3**, 466–472 (2001).

15. Stricker, J., Aratyn-Schaus, Y., Oakes, P. W. & Gardel, M. L. Spatiotemporal Constraints on the Force-Dependent Growth of Focal Adhesions. *Biophys. J.* **100**, 2883–2893 (2011).

16. Dvir, T., Timko, B. P., Kohane, D. S. & Langer, R. Nanotechnological strategies for engineering complex tissues. *Nat. Nanotechnol.* **6**, 13–22 (2011).

17. Kim, J. *et al.* Designing nanotopographical density of extracellular matrix for controlled morphology and function of human mesenchymal stem cells. *Sci. Rep.* **3**, 3552 (2013).

18. Biela, S. A., Su, Y., Spatz, J. P. & Kemkemer, R. Different sensitivity of human endothelial cells, smooth muscle cells and fibroblasts to topography in the nano–micro range. *Acta Biomater.* **5**, 2460–2466 (2009).

19. Meyle, J., Gültig, K. & Nisch, W. Variation in contact guidance by human cells on a microstructured surface. *J. Biomed. Mater. Res.* **29**, 81–88 (1995).

20. Biggs, M. J. P., Richards, R. G. & Dalby, M. J. Nanotopographical modification: a regulator of cellular function through focal adhesions. *Nanomedicine Nanotechnol. Biol. Med.* **6**, 619–633 (2010).

21. Deok-Ho Kim *et al.* Modulation of Adhesion and Growth of Cardiac Myocytes by Surface Nanotopography. in *2005 IEEE Engineering in Medicine and Biology 27th Annual Conference* 4091–4094 (IEEE, 2005). doi:10.1109/IEMBS.2005.1615362.

22. Lee, J. *et al.* The control of cell adhesion and viability by zinc oxide nanorods. *Biomaterials* **29**, 3743–3749 (2008).

23. Huang, J. *et al.* Impact of Order and Disorder in RGD Nanopatterns on Cell Adhesion. *Nano Lett.* **9**, 1111–1116 (2009).

24. Schvartzman, M. *et al.* Nanolithographic control of the spatial organization of cellular adhesion receptors at the single-molecule level. *Nano Lett.* **11**, 1306–1312 (2011).

25. Biggs, M. J. P., Richards, R. G., Gadegaard, N., Wilkinson, C. D. W. & Dalby, M. J. Regulation of implant surface cell adhesion: characterization and quantification of S-phase primary osteoblast adhesions on biomimetic nanoscale substrates. *J. Orthop. Res.* **25**, 273–282 (2007).

26. Matsuzaka, K., Walboomers, F., Ruijter, A. & Jansen, J. A. Effect of microgrooved poly-l-lactic (PLA) surfaces on proliferation, cytoskeletal organization, and mineralized matrix formation of rat bone marrow cells. *Clin. Oral Implants Res.* **11**, 325–333 (2000).

27. Ventre, M., Natale, C. F., Rianna, C. & Netti, P. A. Topographic cell instructive patterns to control cell adhesion, polarization and migration. *J. R. Soc. Interface* **11**, 20140687 (2014).

28. Department of Biomaterials, Radboud University Nijmegen Medical Centre 309 PB, PO Box 9101, 6500HB Nijmegen, The Netherlands *et al.* The influence of nanoscale topographical cues on initial osteoblast morphology and migration. *Eur. Cell. Mater.* **20**, 329–343 (2010).

29. Natale, C. F., Ventre, M. & Netti, P. A. Tuning the material-cytoskeleton crosstalk via nanoconfinement of focal adhesions. *Biomaterials* **35**, 2743–2751 (2014).

30. Trappmann, B. *et al.* Extracellular-matrix tethering regulates stem-cell fate. *Nat. Mater.* **11**, 642–649 (2012).

31. Wen, J. H. *et al.* Interplay of matrix stiffness and protein tethering in stem cell differentiation. *Nat. Mater.* **13**, 979–987 (2014).

32. du Roure, O. *et al.* Force mapping in epithelial cell migration. *Proc. Natl. Acad. Sci.* **102**, 2390–2395 (2005).

33. Wang, N. & Stamenović, D. Contribution of intermediate filaments to cell stiffness, stiffening, and growth. *Am. J. Physiol.-Cell Physiol.* **279**, C188–C194 (2000).

34. Pelham, R. J. & Wang, Y. -l. Cell locomotion and focal adhesions are regulated by substrate flexibility. *Proc. Natl. Acad. Sci.* **94**, 13661–13665 (1997).

35. Peyton, S. R. & Putnam, A. J. Extracellular matrix rigidity governs smooth muscle cell motility in a biphasic fashion. *J. Cell. Physiol.* **204**, 198–209 (2005).

36. Lo, C.-M., Wang, H.-B., Dembo, M. & Wang, Y. Cell Movement Is Guided by the Rigidity of the Substrate. *Biophys. J.* **79**, 144–152 (2000).

37. Chen, C. S. Geometric Control of Cell Life and Death. *Science* **276**, 1425–1428 (1997).

38. von Erlach, T. C. *et al.* Cell-geometry-dependent changes in plasma membrane order direct stem cell signalling and fate. *Nat. Mater.* **17**, 237–242 (2018).

39. James, J., Goluch, E. D., Hu, H., Liu, C. & Mrksich, M. Subcellular curvature at the perimeter of micropatterned cells influences lamellipodial distribution and cell polarity. *Cell Motil. Cytoskeleton* **65**, 841–852 (2008).

40. Kilian, K. A., Bugarija, B., Lahn, B. T. & Mrksich, M. Geometric cues for directing the differentiation of mesenchymal stem cells. *Proc. Natl. Acad. Sci.* **107**, 4872–4877 (2010).

41. Zhang, D. & Kilian, K. A. The effect of mesenchymal stem cell shape on the maintenance of multipotency. *Biomaterials* **34**, 3962–3969 (2013).

42. Alisafaei, F., Jokhun, D. S., Shivashankar, G. V. & Shenoy, V. B. Regulation of nuclear architecture, mechanics, and nucleocytoplasmic shuttling of epigenetic factors by cell geometric constraints. *Proc. Natl. Acad. Sci.* **116**, 13200–13209 (2019).

43. Damodaran, K. *et al.* Compressive force induces reversible chromatin condensation and cell geometry–dependent transcriptional response. *Mol. Biol. Cell* **29**, 3039–3051 (2018).

44. Swift, J. *et al.* Nuclear Lamin-A Scales with Tissue Stiffness and Enhances Matrix-Directed Differentiation. *Science* **341**, 1240104–1240104 (2013).

45. Bonnans, C., Chou, J. & Werb, Z. Remodelling the extracellular matrix in development and disease. *Nat. Rev. Mol. Cell Biol.* **15**, 786–801 (2014).

46. Frantz, C., Stewart, K. M. & Weaver, V. M. The extracellular matrix at a glance. *J. Cell Sci.* **123**, 4195–4200 (2010).

47. Kular, J. K., Basu, S. & Sharma, R. I. The extracellular matrix: Structure, composition, age-related differences, tools for analysis and applications for tissue engineering. *J. Tissue Eng.* **5**, 204173141455711 (2014).

48. Lu, P., Takai, K., Weaver, V. M. & Werb, Z. Extracellular Matrix Degradation and Remodeling in Development and Disease. *Cold Spring Harb. Perspect. Biol.* **3**, a005058–a005058 (2011).

49. Roy, D., Cambre, J. N. & Sumerlin, B. S. Future perspectives and recent advances in stimuli-responsive materials. *Prog. Polym. Sci.* **35**, 278–301 (2010).

50. Stuart, M. A. C. *et al.* Emerging applications of stimuli-responsive polymer materials. *Nat. Mater.* **9**, 101–113 (2010).

51. Ulman, A. Formation and Structure of Self-Assembled Monolayers. *Chem. Rev.* **96**, 1533–1554 (1996).

52. Mrksich, M. Using self-assembled monolayers to model the extracellular matrix. *Acta Biomater.* **5**, 832–841 (2009).

53. Onclin, S., Ravoo, B. J. & Reinhoudt, D. N. Engineering Silicon Oxide Surfaces Using Self-Assembled Monolayers. *Angew. Chem. Int. Ed.* **44**, 6282–6304 (2005).

54. Schreiber, F. Self-assembled monolayers: from simple model systems to biofunctionalized interfaces. *J. Phys. Condens. Matter* **16**, R881–R900 (2004).

55. Mendes, P. M. Stimuli-responsive surfaces for bio-applications. *Chem. Soc. Rev.* **37**, 2512 (2008).

56. Nakanishi, J. *et al.* Spatiotemporal control of cell adhesion on a self-assembled monolayer having a photocleavable protecting group. *Anal. Chim. Acta* **578**, 100–104 (2006).

57. Nakanishi, J. *et al.* Spatiotemporal Control of Migration of Single Cells on a Photoactivatable Cell Microarray. *J. Am. Chem. Soc.* **129**, 6694–6695 (2007).

58. Vignaud, T., Blanchoin, L. & Théry, M. Directed cytoskeleton self-organization. *Spec. Issue – Synth. Cell Biol.* **22**, 671–682 (2012).

59. Fedele, C., Netti, P. A. & Cavalli, S. Azobenzene-based polymers: emerging applications as cell culture platforms. *Biomater. Sci.* **6**, 990–995 (2018).

60. Klajn, R. Spiropyran-based dynamic materials. *Chem Soc Rev* **43**, 148–184 (2014).

61. Landry, M. J., Rollet, F.-G., Kennedy, T. E. & Barrett, C. J. Layers and Multilayers of Self-Assembled Polymers: Tunable Engineered Extracellular Matrix Coatings for Neural Cell Growth. *Langmuir* **34**, 8709–8730 (2018).

62. Higuchi, A. *et al.* Photon-Modulated Changes of Cell Attachments on Poly(spiropyran- *co* -methyl methacrylate) Membranes. *Biomacromolecules* **5**, 1770–1774 (2004).

63. Edahiro, J. *et al.* In Situ Control of Cell Adhesion Using Photoresponsive Culture Surface. *Biomacromolecules* **6**, 970–974 (2005).

64. Auernheimer, J., Dahmen, C., Hersel, U., Bausch, A. & Kessler, H. Photoswitched Cell Adhesion on Surfaces with RGD Peptides. *J. Am. Chem. Soc.* **127**, 16107–16110 (2005).

65. Liu, D., Xie, Y., Shao, H. & Jiang, X. Using Azobenzene-Embedded Self-Assembled Monolayers To Photochemically Control Cell Adhesion Reversibly. *Angew. Chem. Int. Ed.* **48**, 4406–4408 (2009).

66. Engler, A. J., Sen, S., Sweeney, H. L. & Discher, D. E. Matrix elasticity directs stem cell lineage specification. *Cell* **126**, 677–689 (2006).

67. Frey, M. T. & Wang, Y. A photo-modulatable material for probing cellular responses to substrate rigidity. *Soft Matter* **5**, 1918 (2009).

68. Kloxin, A. M., Benton, J. A. & Anseth, K. S. In situ elasticity modulation with dynamic substrates to direct cell phenotype. *Biomaterials* **31**, 1–8 (2010).

69. Guvendiren, M. & Burdick, J. A. Stiffening hydrogels to probe short- and long-term cellular responses to dynamic mechanics. *Nat. Commun.* **3**, 792 (2012).

70. Berry, M. F. *et al.* Mesenchymal stem cell injection after myocardial infarction improves myocardial compliance. *Am. J. Physiol.-Heart Circ. Physiol.* **290**, H2196–H2203 (2006).

71. Georges, P. C. *et al.* Increased stiffness of the rat liver precedes matrix deposition: implications for fibrosis. *Am. J. Physiol.-Gastrointest. Liver Physiol.* **293**, G1147–G1154 (2007).

72. Krieg, M. *et al.* Tensile forces govern germ-layer organization in zebrafish. *Nat. Cell Biol.* **10**, 429–436 (2008).

73. Yang, C., Tibbitt, M. W., Basta, L. & Anseth, K. S. Mechanical memory and dosing influence stem cell fate. *Nat. Mater.* **13**, 645–652 (2014).

74. Cutiongco, M. F. A., Jensen, B. S., Reynolds, P. M. & Gadegaard, N. Predicting gene expression using morphological cell responses to nanotopography. *Nat. Commun.* **11**, 1384 (2020).

75. Kobayashi, T., Degenkolb, E. O. & Rentzepis, P. M. Picosecond spectroscopy of 1-phenylazo-2-hydroxynaphthalene. *J. Phys. Chem.* **83**, 2431–2434 (1979).

76. Bandara, H. M. D. & Burdette, S. C. Photoisomerization in different classes of azobenzene. *Chem Soc Rev* **41**, 1809–1825 (2012).

77. Han, M. & Ichimura, K. Tilt Orientation of *p* -Methoxyazobenzene Side Chains in Liquid Crystalline Polymer Films by Irradiation with Nonpolarized Light. *Macromolecules* **34**, 82–89 (2001).

78. Jeng, R. J., Chen, Y. M., Kumar, J. & Tripathy, S. K. Novel Crosslinked Guest-Host System with Stable Second-Order Nonlinearity. *J. Macromol. Sci. Part A* **29**, 1115–1127 (1992).

79. Bian, S. *et al.* Single laser beam-induced surface deformation on azobenzene polymer films. *Appl. Phys. Lett.* **73**, 1817–1819 (1998).

80. Bian, S. *et al.* Photoinduced surface deformations on azobenzene polymer films. *J. Appl. Phys.* **86**, 4498–4508 (1999).

81. Kirschner, C. M. & Anseth, K. S. Hydrogels in healthcare: From static to dynamic material microenvironments. *Diam. Jubil. Issue* **61**, 931–944 (2013).

82. Beharry, A. A. & Woolley, G. A. Azobenzene photoswitches for biomolecules. *Chem. Soc. Rev.* **40**, 4422 (2011).

83. Goulet-Hanssens, A., Magdesian, M. H., Lopez-Ayon, G. M., Grutter, P. & Barrett, C. J. Reversing adhesion with light: a general method for functionalized bead release from cells. *Biomater. Sci.* **4**, 1193–1196 (2016).

84. Wei, Y., Tang, Q., Gong, C. & Lam, M. H.-W. Review of the recent progress in photoresponsive molecularly imprinted polymers containing azobenzene chromophores. *Anal. Chim. Acta* **900**, 10–20 (2015).

85. Barillé, R., Janik, R., Kucharski, S., Eyer, J. & Letournel, F. Photo-responsive polymer with erasable and reconfigurable micro- and nano-patterns: An in vitro study for neuron guidance. *Colloids Surf. B Biointerfaces* **88**, 63–71 (2011).

86. Rianna, C. *et al.* Reversible Holographic Patterns on Azopolymers for Guiding Cell Adhesion and Orientation. *ACS Appl. Mater. Interfaces* **7**, 16984–16991 (2015).

87. Rianna, C. *et al.* Spatio-Temporal Control of Dynamic Topographic Patterns on Azopolymers for Cell Culture Applications. *Adv. Funct. Mater.* **26**, 7572–7580 (2016).

88. Rossano, L., Cimmino, C., Cavalli, S., Ventre, M. & Netti, P. A. Regulating Fibroblast Shape and Mechanics through Photoresponsive Surfaces with Concentric Circular Topographic Patterns. *Adv. Mater. Interfaces* **5**, 1800890 (2018).

89. Kirby, T. J. & Lammerding, J. Emerging views of the nucleus as a cellular mechanosensor. *Nat. Cell Biol.* **20**, 373–381 (2018).

90. Iyer, K. V., Pulford, S., Mogilner, A. & Shivashankar, G. V. Mechanical Activation of Cells Induces Chromatin Remodeling Preceding MKL Nuclear Transport. *Biophys. J.* **103**, 1416–1428 (2012).

91. Poh, Y.-C. *et al.* Dynamic force-induced direct dissociation of protein complexes in a nuclear body in living cells. *Nat. Commun.* **3**, 866 (2012).

92. Navarro, A. P., Collins, M. A. & Folker, E. S. The nucleus is a conserved mechanosensation and mechanoresponse organelle: The Nucleus is a Mechanotransduction Organelle. *Cytoskeleton* **73**, 59–67 (2016).

93. Venturini, V. *et al.* The nucleus measures shape changes for cellular proprioception to control dynamic cell behavior. *Science* **370**, eaba2644 (2020).

94. Lomakin, A. J. *et al.* The nucleus acts as a ruler tailoring cell responses to spatial constraints. *Science* **370**, eaba2894 (2020).

95. Elosegui-Artola, A. *et al.* Force Triggers YAP Nuclear Entry by Regulating Transport across Nuclear Pores. *Cell* **171**, 1397-1410.e14 (2017).

96. Ingber, D. E. From mechanobiology to developmentally inspired engineering. *Philos. Trans. R. Soc. B Biol. Sci.* **373**, 20170323 (2018).

97. Meshorer, E. *et al.* Hyperdynamic Plasticity of Chromatin Proteins in Pluripotent Embryonic Stem Cells. *Dev. Cell* **10**, 105–116 (2006).

98. Pajerowski, J. D., Dahl, K. N., Zhong, F. L., Sammak, P. J. & Discher, D. E. Physical plasticity of the nucleus in stem cell differentiation. *Proc. Natl. Acad. Sci.* **104**, 15619–15624 (2007).

99. Talwar, S., Kumar, A., Rao, M., Menon, G. I. & Shivashankar, G. V. Correlated Spatio-Temporal Fluctuations in Chromatin Compaction States Characterize Stem Cells. *Biophys. J.* **104**, 553–564 (2013).

100. Bhattacharya, D., Talwar, S., Mazumder, A. & Shivashankar, G. V. Spatio-Temporal Plasticity in Chromatin Organization in Mouse Cell Differentiation and during Drosophila Embryogenesis. *Biophys. J.* **96**, 3832–3839 (2009).

101. Hamidi, H. & Ivaska, J. Every step of the way: integrins in cancer progression and metastasis. *Nat. Rev. Cancer* **18**, 533–548 (2018).

102. Song, Y., Soto, J., Chen, B., Yang, L. & Li, S. Cell engineering: Biophysical regulation of the nucleus. *Biomaterials* **234**, 119743 (2020).

103. Wilson, K. L. & Berk, J. M. The nuclear envelope at a glance. *J. Cell Sci.* **123**, 1973–1978 (2010).

104. Dechat, T. *et al.* Nuclear lamins: major factors in the structural organization and function of the nucleus and chromatin. *Genes Dev.* **22**, 832–853 (2008).

105. Ho, C. Y. & Lammerding, J. Lamins at a glance. *J. Cell Sci.* **125**, 2087–2093 (2012).

106. Vergnes, L., Peterfy, M., Bergo, M. O., Young, S. G. & Reue, K. Lamin B1 is required for mouse development and nuclear integrity. *Proc. Natl. Acad. Sci.* **101**, 10428–10433 (2004).

107. Coffinier, C. *et al.* Abnormal development of the cerebral cortex and cerebellum in the setting of lamin B2 deficiency. *Proc. Natl. Acad. Sci.* **107**, 5076–5081 (2010).

108. Röber, R. A., Weber, K. & Osborn, M. Differential timing of nuclear lamin A/C expression in the various organs of the mouse embryo and the young animal: a developmental study. *Dev. Camb. Engl.* **105**, 365–378 (1989).

109. Sullivan, T. *et al.* Loss of a-Type Lamin Expression Compromises Nuclear Envelope Integrity Leading to Muscular Dystrophy. *J. Cell Biol.* **147**, 913–920 (1999).

110. Zwerger, M. *et al.* Myopathic lamin mutations impair nuclear stability in cells and tissue and disrupt nucleo-cytoskeletal coupling. *Hum. Mol. Genet.* **22**, 2335–2349 (2013).

111. Lombardi, M. L. *et al.* The interaction between nesprins and sun proteins at the nuclear envelope is critical for force transmission between the nucleus and cytoskeleton. *J. Biol. Chem.* **286**, 26743–26753 (2011).

112. Caille, N., Tardy, Y. & Meister, J. J. Assessment of Strain Field in Endothelial Cells Subjected to Uniaxial Deformation of Their Substrate. *Ann. Biomed. Eng.* **26**, 409–416 (1998).

113. Shumaker, D. K., Kuczmarski, E. R. & Goldman, R. D. The nucleoskeleton: lamins and actin are major players in essential nuclear functions. *Curr. Opin. Cell Biol.* **15**, 358–366 (2003).

114. Earle, A. J. *et al.* Mutant lamins cause nuclear envelope rupture and DNA damage in skeletal muscle cells. *Nat. Mater.* **19**, 464–473 (2020).

115. Schreiber, K. H. & Kennedy, B. K. When Lamins Go Bad: Nuclear Structure and Disease. *Cell* **152**, 1365–1375 (2013).

116. Worman, H. J. Nuclear lamins and laminopathies. *J. Pathol.* **226**, 316–325 (2012).

117. Bizhanova, A. & Kaufman, P. D. Close to the edge: Heterochromatin at the nucleolar and nuclear peripheries. *Biochim. Biophys. Acta BBA - Gene Regul. Mech.* **1864**, 194666 (2021).

118. Kurdistani, S. K. & Grunstein, M. Histone acetylation and deacetylation in yeast. *Nat. Rev. Mol. Cell Biol.* **4**, 276–284 (2003).

119. Shahbazian, M. D. & Grunstein, M. Functions of site-specific histone acetylation and deacetylation. *Annu. Rev. Biochem.* **76**, 75–100 (2007).

120. Richards, E. J. & Elgin, S. C. R. Epigenetic codes for heterochromatin formation and silencing: rounding up the usual suspects. *Cell* **108**, 489–500 (2002).

121. Taddei, A., Maison, C., Roche, D. & Almouzni, G. Reversible disruption of pericentric heterochromatin and centromere function by inhibiting deacetylases. *Nat. Cell Biol.* **3**, 114–120 (2001).

122. Li, Q., Kumar, A., Makhija, E. & Shivashankar, G. V. The regulation of dynamic mechanical coupling between actin cytoskeleton and nucleus by matrix geometry. *Biomaterials* **35**, 961–969 (2014).

123. Li, Y. *et al.* Biophysical Regulation of Histone Acetylation in Mesenchymal Stem Cells. *Biophys. J.* **100**, 1902–1909 (2011).

124. Makhija, E., Jokhun, D. S. & Shivashankar, G. V. Nuclear deformability and telomere dynamics are regulated by cell geometric constraints. *Proc. Natl. Acad. Sci.* **113**, E32–E40 (2016).

125. Roy, B. *et al.* Laterally confined growth of cells induces nuclear reprogramming in the absence of exogenous biochemical factors. *Proc. Natl. Acad. Sci.* **115**, E4741–E4750 (2018).

126. Versaevel, M., Grevesse, T. & Gabriele, S. Spatial coordination between cell and nuclear shape within micropatterned endothelial cells. *Nat. Commun.* **3**, 671 (2012).

127. Meng, Z., Moroishi, T. & Guan, K.-L. Mechanisms of Hippo pathway regulation. *Genes Dev.* **30**, 1–17 (2016).

128. Piccolo, S., Dupont, S. & Cordenonsi, M. The Biology of YAP/TAZ: Hippo Signaling and Beyond. *Physiol. Rev.* **94**, 1287–1312 (2014).

129. Porazinski, S. *et al.* YAP is essential for tissue tension to ensure vertebrate 3D body shape. *Nature* **521**, 217–221 (2015).

130. Varelas, X. The Hippo pathway effectors TAZ and YAP in development, homeostasis and disease. *Development* **141**, 1614–1626 (2014).

131. Zhao, B., Li, L., Lei, Q. & Guan, K. L. The Hippo-YAP pathway in organ size control and tumorigenesis: an updated version. *Genes Dev.* **24**, 862–874 (2010).

132. Moroishi, T., Hansen, C. G. & Guan, K.-L. The emerging roles of YAP and TAZ in cancer. *Nat. Rev. Cancer* **15**, 73–79 (2015).

133. Plouffe, S. W., Hong, A. W. & Guan, K.-L. Disease implications of the Hippo/YAP pathway. *Trends Mol. Med.* **21**, 212–222 (2015).

134. Zanconato, F., Cordenonsi, M. & Piccolo, S. YAP/TAZ at the Roots of Cancer. *Cancer Cell* **29**, 783–803 (2016).

135. Nakajima, H. *et al.* Flow-Dependent Endothelial YAP Regulation Contributes to Vessel Maintenance. *Dev. Cell* **40**, 523-536.e6 (2017).

136. Aragona, M. *et al.* A Mechanical Checkpoint Controls Multicellular Growth through YAP/TAZ Regulation by Actin-Processing Factors. *Cell* **154**, 1047–1059 (2013).

137. Das, A., Fischer, R. S., Pan, D. & Waterman, C. M. YAP Nuclear Localization in the Absence of Cell-Cell Contact Is Mediated by a Filamentous Actin-dependent, Myosin II- and Phospho-YAP-independent Pathway during Extracellular Matrix Mechanosensing*. *J. Biol. Chem.* **291**, 6096–6110 (2016).

138. Dupont, S. *et al.* Role of YAP/TAZ in mechanotransduction. *Nature* **474**, 179–183 (2011).

139. Driscoll, T. P., Cosgrove, B. D., Heo, S.-J., Shurden, Z. E. & Mauck, R. L. Cytoskeletal to Nuclear Strain Transfer Regulates YAP Signaling in Mesenchymal Stem Cells. *Biophys. J.* **108**, 2783–2793 (2015).

140. Benham-Pyle, B. W., Pruitt, B. L. & Nelson, W. J. Mechanical strain induces E-cadherin-dependent Yap1 and -catenin activation to drive cell cycle entry. *Science* **348**, 1024–1027 (2015).

141. Lautenschläger, F. *et al.* The regulatory role of cell mechanics for migration of differentiating myeloid cells. *Proc. Natl. Acad. Sci.* **106**, 15696–15701 (2009).

142. Guck, J. *et al.* Optical Deformability as an Inherent Cell Marker for Testing Malignant Transformation and Metastatic Competence. *Biophys. J.* **88**, 3689–3698 (2005).

143. Bufi, N. *et al.* Human Primary Immune Cells Exhibit Distinct Mechanical Properties that Are Modified by Inflammation. *Biophys. J.* **108**, 2181–2190 (2015).

144. Anselme, K., Wakhloo, N. T., Rougerie, P. & Pieuchot, L. Role of the Nucleus as a Sensor of Cell Environment Topography. *Adv. Healthc. Mater.* **7**, 1701154 (2018).

145. Wu, P.-H. *et al.* A comparison of methods to assess cell mechanical properties. *Nat. Methods* **15**, 491–498 (2018).

146. Pennacchio, F. A., Nastały, P., Poli, A. & Maiuri, P. Tailoring Cellular Function: The Contribution of the Nucleus in Mechanotransduction. *Front. Bioeng. Biotechnol.* **8**, 596746 (2021).

147. Mietke, A. *et al.* Extracting Cell Stiffness from Real-Time Deformability Cytometry: Theory and Experiment. *Biophys. J.* **109**, 2023–2036 (2015).

148. Elsayad, K. *et al.* Mapping the subcellular mechanical properties of live cells in tissues with fluorescence emission-Brillouin imaging. *Sci. Signal.* **9**, rs5 (2016).

149. Huth, S., Sindt, S. & Selhuber-Unkel, C. Automated analysis of soft hydrogel microindentation: Impact of various indentation parameters on the measurement of Young's modulus. *PloS One* **14**, e0220281 (2019).

150. Guz, N., Dokukin, M., Kalaparthi, V. & Sokolov, I. If Cell Mechanics Can Be Described by Elastic Modulus: Study of Different Models and Probes Used in Indentation Experiments. *Biophys. J.* **107**, 564–575 (2014).

151. AU - Thomas, G., AU - Burnham, N. A., AU - Camesano, T. A. & AU - Wen, Q. Measuring the Mechanical Properties of Living Cells Using Atomic Force Microscopy. *J. Vis. Exp.* e50497 (2013) doi:10.3791/50497.

152. Gavara, N. A beginner's guide to atomic force microscopy probing for cell mechanics: GAVARA. *Microsc. Res. Tech.* **80**, 75–84 (2017).

153. Variola, F. Atomic force microscopy in biomaterials surface science. *Phys. Chem. Chem. Phys.* **17**, 2950–2959 (2015).

154. Marrese, M., Guarino, V. & Ambrosio, L. Atomic Force Microscopy: A Powerful Tool to Address Scaffold Design in Tissue Engineering. *J. Funct. Biomater.* **8**, (2017).

155. Pillarisetti, A. *et al.* Mechanical phenotyping of mouse embryonic stem cells: increase in stiffness with differentiation. *Cell. Reprogramming* **13**, 371–380 (2011).

156. Fernández, P., Heymann, L., Ott, A., Aksel, N. & Pullarkat, P. A. Shear rheology of a cell monolayer. *New J. Phys.* **9**, 419–419 (2007).

157. Chalut, K. J., Ekpenyong, A. E., Clegg, W. L., Melhuish, I. C. & Guck, J. Quantifying cellular differentiation by physical phenotype using digital holographic microscopy. *Integr. Biol. Quant. Biosci. Nano Macro* **4**, 280–284 (2012).

158. Remmerbach, T. W. *et al.* Oral Cancer Diagnosis by Mechanical Phenotyping. *Cancer Res.* **69**, 1728–1732 (2009).

159. Fabry, B., Maksym, G. N., Hubmayr, R. D., Butler, J. P. & Fredberg, J. J. Implications of heterogeneous bead behavior on cell mechanical properties measured with magnetic twisting cytometry. *J. Magn. Magn. Mater.* **194**, 120–125 (1999).

160. Wang, N., Poh, Y.-C. & Wang, N. The use of Optical Magnetic Twisting Cytometry and Flourescence Resonance Energy Transfer to quantify force-induced protein dissociation in the nucleus of a living cell. *Protoc. Exch.* (2012) doi:10.1038/protex.2012.012.

161. Wirtz, D. Particle-Tracking Microrheology of Living Cells: Principles and Applications. *Annu. Rev. Biophys.* **38**, 301–326 (2009).

162. Tseng, Y., Kole, T. P. & Wirtz, D. Micromechanical Mapping of Live Cells by Multiple-Particle-Tracking Microrheology. *Biophys. J.* **83**, 3162–3176 (2002).

163. Guilluy, C. *et al.* Isolated nuclei adapt to force and reveal a mechanotransduction pathway in the nucleus. *Nat. Cell Biol.* **16**, 376–381 (2014).

164. Wang, X. *et al.* Intracellular manipulation and measurement with multipole magnetic tweezers. *Sci. Robot.* **4**, eaav6180 (2019).

165. Neelam, S. *et al.* Direct force probe reveals the mechanics of nuclear homeostasis in the mammalian cell. *Proc. Natl. Acad. Sci.* **112**, 5720–5725 (2015).

166. Wintner, O. *et al.* A Unified Linear Viscoelastic Model of the Cell Nucleus Defines the Mechanical Contributions of Lamins and Chromatin. *Adv. Sci.* **7**, 1901222 (2020).

167. Lee, L. M. & Liu, A. P. The Application of Micropipette Aspiration in Molecular Mechanics of Single Cells. *J. Nanotechnol. Eng. Med.* **5**, 040902 (2014).

168. Herbig, M. *et al.* Real-Time Deformability Cytometry: Label-Free Functional Characterization of Cells. in *Flow Cytometry Protocols* (eds. Hawley, T. S. & Hawley, R. G.) vol. 1678 347–369 (Springer New York, 2018).

169. Ye, T., Shi, H., Phan-Thien, N., Lim, C. T. & Li, Y. Numerical design of a microfluidic chip for probing mechanical properties of cells. *J. Biomech.* **84**, 103–112 (2019).

170. Gossett, D. R. *et al.* Hydrodynamic stretching of single cells for large population mechanical phenotyping. *Proc. Natl. Acad. Sci.* **109**, 7630–7635 (2012).

171. Zhang, J., Nou, X. A., Kim, H. & Scarcelli, G. Brillouin flow cytometry for label-free mechanical phenotyping of the nucleus. *Lab. Chip* **17**, 663–670 (2017).

172. Ermis, M., Akkaynak, D., Chen, P., Demirci, U. & Hasirci, V. A high throughput approach for analysis of cell nuclear deformability at single cell level. *Sci. Rep.* **6**, 36917 (2016).

173. Babahosseini, H., Ketene, A. N., Schmelz, E. M., Roberts, P. C. & Agah, M. Biomechanical profile of cancer stem-like/tumor-initiating cells derived from a progressive ovarian cancer model. *Nanomedicine Nanotechnol. Biol. Med.* **10**, e1013–e1019 (2014).

174. Hvichia, G. E. *et al.* A novel microfluidic platform for size and deformability based separation and the subsequent molecular characterization of viable circulating tumor cells. *Int. J. Cancer* **138**, 2894–2904 (2016).

175. Murphy, W. L., McDevitt, T. C. & Engler, A. J. Materials as stem cell regulators. *Nat. Mater.* **13**, 547–557 (2014).

Chapter 2

2 Cellular response on static surfaces

2.1 Introduction

The transmission of mechanical forces from the extracellular matrix (ECM) to the nucleus, through the cytoskeleton, alters the nuclear mechanics and architecture and this, in turn, affects the cell's ability to respond to its mechanical microenvironment by regulating important nuclear functions. Geometrical constraints imposed on cells affect local tensile stresses and subsequently cause alterations in the cytoskeleton and nucleus properties including mechanical properties, chromatin assembly and nuclear morphology.

By performing micropatterning experiments in static, we can clarify how the physical properties of the microenvironment impact the properties of nuclei by regulating the mechanisms through which mechanical forces are transmitted directly and indirectly from the ECM to the nucleus.

To this aim, we fabricated engineered material surfaces with tailored adhesive characteristics to evaluate stem cells behaviour in a deterministic manner. In this chapter, we explore how the material signals modulate the measurement of the cell’s elastic modulus by altering the structural properties of the cell nucleus and the cellular adhesive contacts (FAs). More specifically, we observe how cellular confinement and the nanotopographic patterns dictate and define the FAs formation, spatial positioning and orientation, the formation and organization of actin fibres and the nucleus shape.

2.2 Results and Discussion

Both exogenous forces and cytoskeleton generated ones, alter the properties of nuclei through perinuclear stress fibres that transmit mechanical stresses from FAs to the nuclear envelope. The complex interaction between cell adhesion and intracellular mechanics is particularly interesting to understand how stem cells integrate biophysical stimuli from the surrounding environment and convert them in biochemical events.

To modulate the stem cell adhesion, shape, and mechanical properties, we used the UV-deep light micropatterning technique (μCP) to fabricate culture substrates with specific microscopic features (**Figure 2.1 a**). This technique is characterized by a high resolution of printing in a cost-effective manner. Although the μCP of the adhesive island provides global control of the macroscopic cell shape, it exerts not many effects on the spatial positioning of FAs, as they can form in random positions and the resulting cytoskeleton organization can evolve unpredictably. On the contrary, topographic patterns of nanometric size may display conducive zones for FAs formation and growth juxtaposed to non-conducive ones. The nanopatterning techniques allow achieving a tighter control on FAs positioning, but exert a limited confining effect on the cell shape. Summarizing, adhesive islands confine cell spreading into specific areas, whereas the nanotopographic patterns enable FAs establishment and growth at specific locations. Hence, with the combination of micro-and nanopatterning techniques we can achieve adequate confinement of the cell shape and the control of FAs dynamics, thus the cytoskeleton arrangement and mechanical identity of the cells. Moreover, the use of adhesive islands able to control and to modulate cellular shape is also a useful tool to keep cells isolated and to prevent cell-cell contact as junctions are known to alter FAs and cytoskeleton assembly[1].

The used polycarbonate substrates were classified as flat or nanopatterned. The nanopatterned surfaces in turn were divided into two different types. One composed of parallel and straight channels with a groove and ridge width of 0.7 μm, which we call "**0.7**", and the other composed of parallel and straight channels with a groove and ridge width of 0.35 μm, which we call "**0.35**" (**Figure 2.1 c**). On each of the three types of substrates presented (flat, 0.7 and 0.35), we created adhesive islands (surface area=1300 μm^2) of four different geometries (**Figure 2.1 b**): rectangular and elliptical which we will henceforth call "anisotropic", and circular and square which we will call "isotropic".

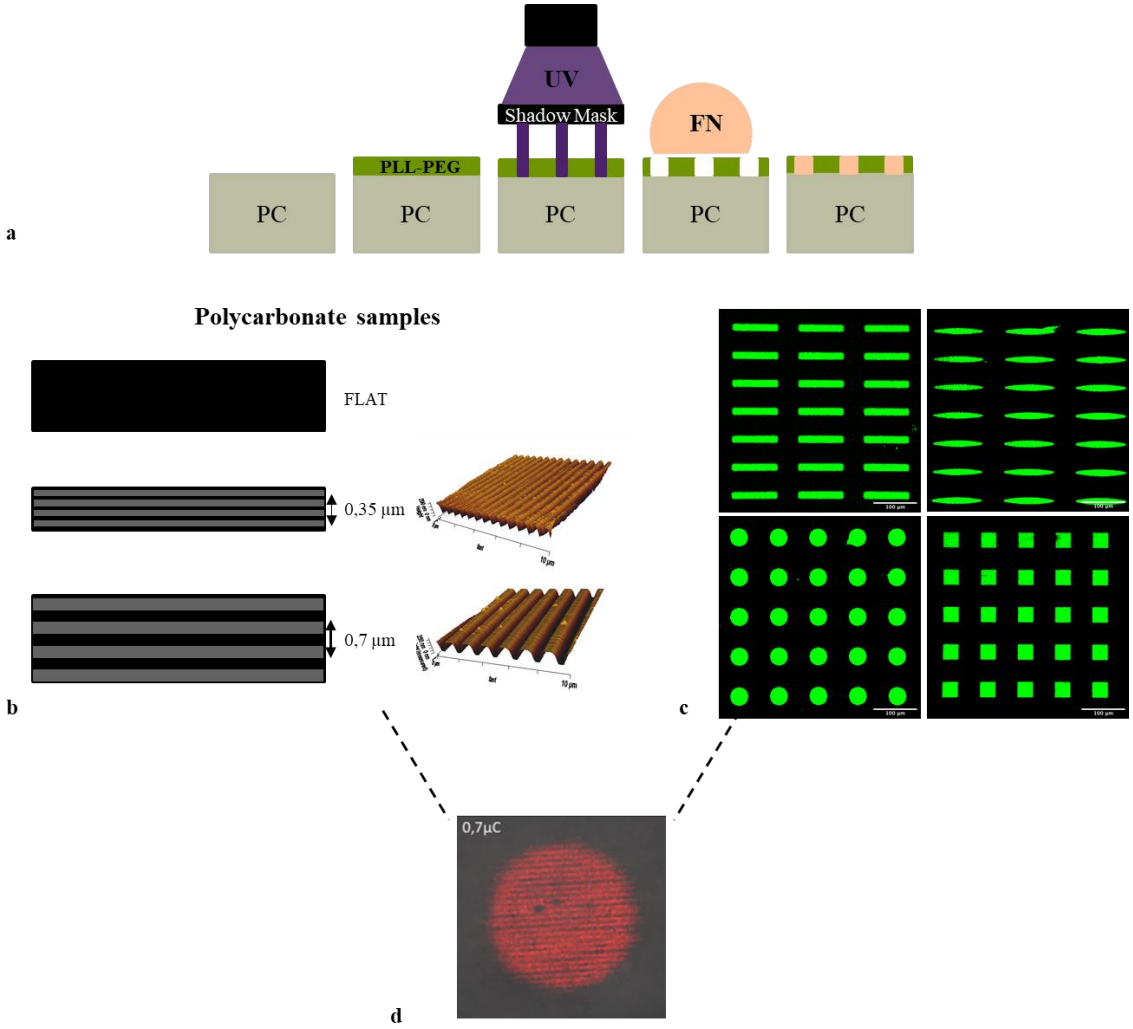

Figure 2.1: (a) *Graphical representation of the micropatterning technique (µCP). Polycarbonate (PC) substrates were incubated with poly-L-lysine-g-poly(ethylene glycol) (PLL-PEG) and illuminated with deep UV light through a photomask. The activated side was then incubated with fibronectin (FN) prior to seeding.* ***(b)*** *Flat and nanopatterned polycarbonate substrates. The nanopatterned surfaces were composed of parallel and straight channels with a groove and ridge width of 0.35 and 0.7 µm.* ***(c)*** *Adhesive islands (surface area=1300 µm^2) of four different geometries rectangular, elliptical, square, and circular.* ***(d)*** *Example of a circular adhesive island fabricated on a 0.7 nanopatterned polycarbonate substrate.*

ASC52telo (hTERT immortalized adipose derived Mesenchymal stem cells) in passages four to eight were cultured on either anisotropic or isotropic flat and patterned substrates for 24 hours and subsequently are fixed and stained for FAs proteins (vinculin), for cytoskeleton (phalloidin) and for the nucleus (DAPI). These were analysed using conventional immunofluorescence and confocal microscopy imaging is employed to obtain clear high-resolution images of the cells (**Figure 2.2**).

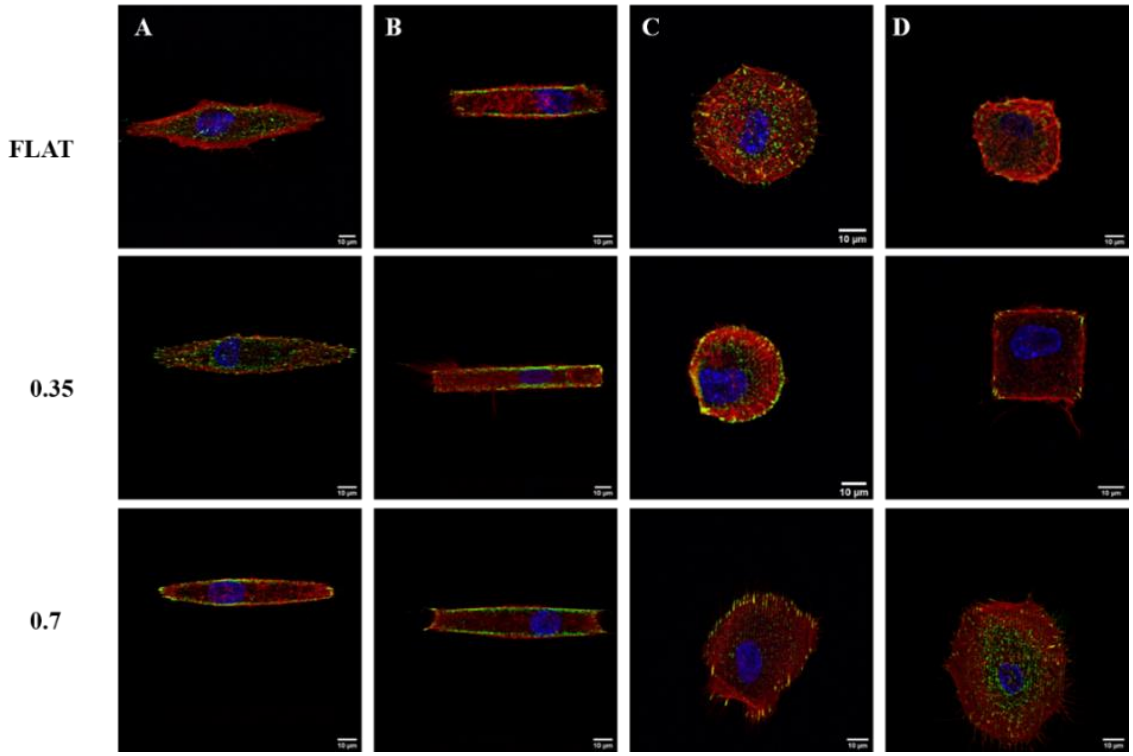

Figure 2.2: (A) *elliptical,* ***(B)*** *rectangular,* ***(C)*** *circular and* ***(D)*** *square cells fixed on flat and with nanopatterns* ***"0.35"*** *and* ***"0.7"*** *substrates. Cell cytoskeleton is stained with phalloidin (red), focal adhesions are immunostained for vinculin (green) and nuclei are stained with DAPI (blue). Scale bars are 10 µm.*

2.2.1 Relationship between cell shape and FA assembly

In this phase of the research, we aim to define how adhesive islands having predetermined shapes, sizes and flat/nanopatterned substrates generate specific spatial assemblies of FAs. Micropattern experiments provide information on the quantitative as well as the qualitative aspect of the FAs.

Previous studies have shown that local forces exerted by stress fibres in stationary cells are related to FAs area[2]. Therefore, we examined how the cell shape changes might affect the spatial organization and extent of vinculin-containing FAs. Qualitatively, the FAs were found to be homogeneously distributed along the periphery of circular cells, whereas they were brighter and concentrated in the corners of square cells. On the elongated patterns, FAs were mostly found on the extremities (**Figure 2.3 a**). These observations indicate gradual but distinctive changes in the spatial distribution of FAs in response to cell shape changes. After quantification of vinculin areas, we found that the FAs area (**Figure 2.3 b**) and FAs length (**Figure 2.3 c**) increased with the extent of cell elongation from isotropic to anisotropic shapes. This behaviour suggests that the overall tension per cell increases with cell elongation. Moreover, we observed that cell cultured on anisotropic micropatterns formed FAs

coaligned with the micropattern major axis (lower angle values) whereas on the isotropic ones, FAs resulted randomly oriented along the cellular body (**Figure 2.3 d**). Additionally, we observed that nanogrooves also impact the formation of the FAs even if adhesive islands provide global control of cell shape. Non-confined cell (ctrl) cultured on nanopatterned surfaces, possessed longer FAs than the flat case (**Figure 2.3 c**). In particular, the FAs formed on 0.7 substrates were statistically longer than those on 0.35 substrates, which in turn were longer than those measured on flat substrates. However, FAs of cell cultured on nanopatterns resulted more oriented with respect to these on flat surfaces (**Figure 2.3 d**). Such a peculiar difference is appreciable both when cells are cultured on "0.7" and "0.35" nanopatterned surfaces. Overall, these data showed that the growth of confined FAs occurs more on nanopatterns, as these limit the adhesion area of FAs and force their growth in a specific direction.

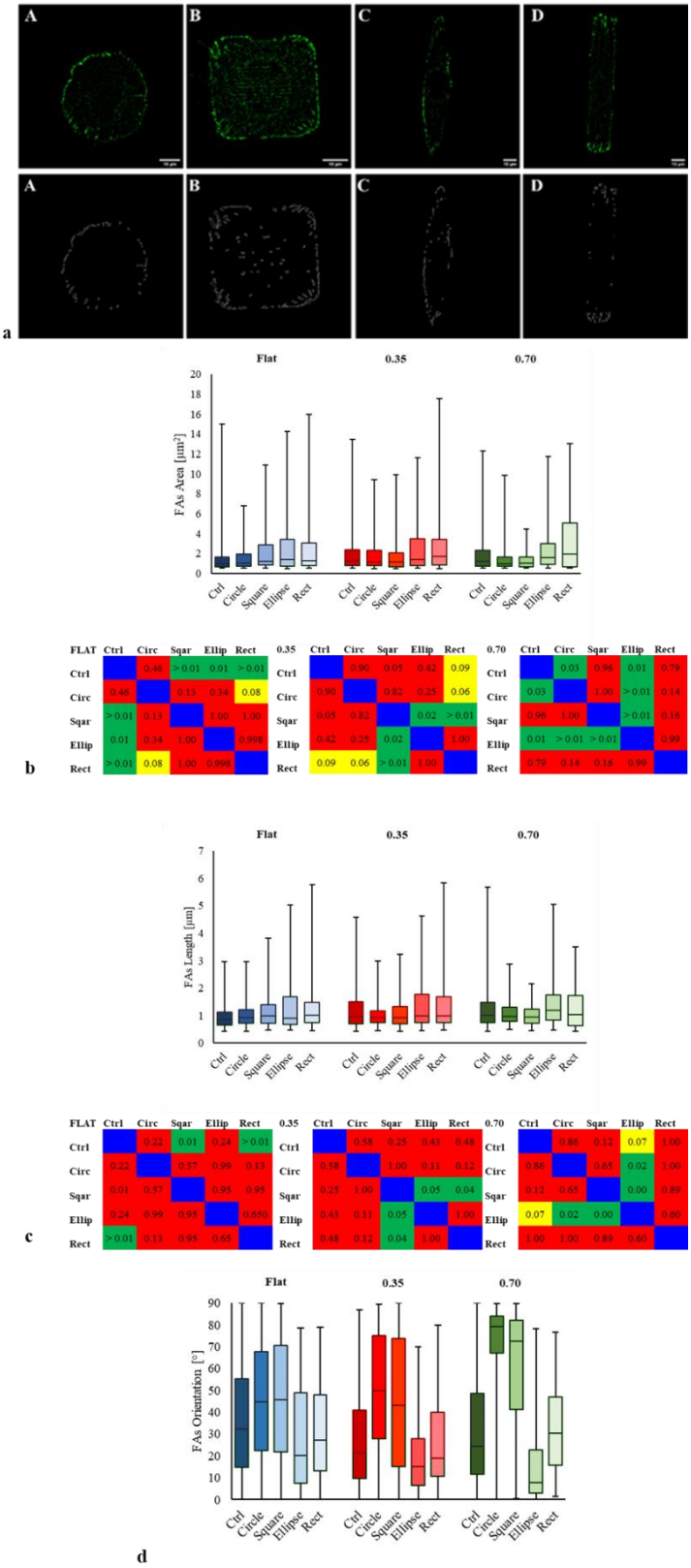

Figure 2.3: (a) *Positioning of vinculin-containing FAs in different shape cells. Focal adhesions are immunostained for vinculin (green). The black and white image highlights the FAs contours. This corresponds to the green image on which we applied the median filter and the background subtraction. Box and whisker of the* ***(b)*** *FA area,* ***(c)*** *FA length and* ***(d)*** *FA orientation in the cell shape evolution. Significance tables: statistically significant differences of the mean values of the moduli are in green ($p < 0.05$) or yellow ($0.10 < p < 0.05$).*

2.2.2 Relationship between cell stiffness, FAs and stress fibres assembly

In this phase of the study, we also define how selected arrangements of FAs on adhesive islands having predetermined shapes and sizes generate specific spatial assemblies of cytoskeletal structures and then we evaluate the impact of such cytoskeleton assembly on cellular mechanics. Actomyosin stress fibres, one of the main components of the cell's cytoskeleton, provide mechanical stability to adherent cells by applying and transmitting tensile forces onto the extracellular matrix (ECM) at the sites of cell-ECM adhesion. Our results provide fundamental and meaningful information for assessing the assembly of altered stress fibres by micro- and nano-patterning techniques. In this regard, we observed how cytoskeletal architecture in terms of thickness and global alignment of fibres modulates cell stiffness. Understanding of the relationship between cell mechanics and cytoskeletal composition requires simultaneous measurement of cell stiffness and quantitative imaging of the cell's cytoskeleton. For this reason, the assembly of cytoskeleton structures is investigated using immunofluorescent staining and confocal microscopy. In this respect, we observed that the organization of the actin cytoskeleton and the formation of stress fibres strongly depend on the shape of the adhesive island. A disorganized meshwork of thin actin filaments with several filopodial protrusions was detectable when cells were cultured on isotropic surfaces, with cortical actin retracing the contour of the coated adhesive island (**Figure 2.4 a, b**). On the contrary, we observed that the cytoskeleton of cells cultured on elongated substrates was prevalently constituted by packed actin stress fibres oriented along the major axis of the elongated cells (**Figure 2.4 c, d**). Moreover, we observed that cellular shape impacted the formation of cell actin cap, a supramolecular structure constituted by thick, parallel, and highly contractile actomyosin filaments, that are specifically anchored to the apical surface of the nucleus[3]. When cells were cultivated on isotropic surfaces, no actin cap was detected after 24 h of culturing (**Figure 2.4 a, b**) while it was observed when cells were cultured on anisotropic ones (**Figure 2.4 c, d**). Then, we investigated the role of nanopatterning on the stress fibres assembly. Surprisingly, we observed that SC cultured on 0.35 and 0.7 patterned surfaces possessed thick basal stress fibres oriented along nanogroove direction particularly evident in anisotropic shapes. The presence of the nanopattern implied a greater orientation of the basal fibres even in the case of cells with isotropic shapes compared to flat surfaces. An actin cap constituted by thin fibres was present on the top of the perinuclear region both for isotropic and anisotropic shapes (**Figure 2.4 e, f, g, h**).

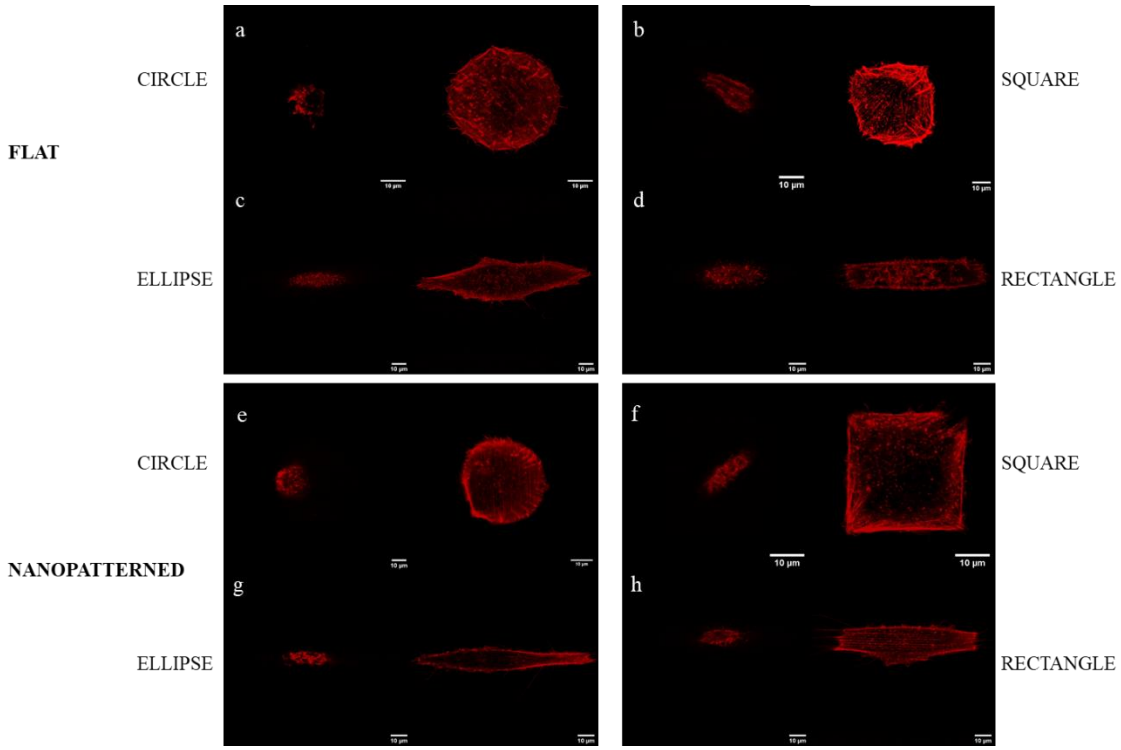

Figure 2.4: *Representative Confocal Z-scan images of actin cytoskeleton of* ***(a, e)*** *circular,* ***(b, f)*** *squared,* ***(c, g)*** *elliptical and* ***(d, h)*** *rectangular SCs cultured on flat and 0.7 nanopatterned surfaces, respectively. Images on the left correspond to the apical optical sections, whereas those on the right to the basal plane. Scale bar is 10 µm.*

Then, we studied how this specific modification of cytoskeleton assembly impact cell mechanical properties. Of the many techniques developed to measure mechanical properties in living cells, atomic force microscopy (AFM) is particularly advantageous, since it allows measurement of global or local mechanical properties in physiological conditions and with good spatial and temporal resolution. We focused on the mechanical properties of the thickest cytosolic area in the vicinity of the nucleus. The distribution of elastic moduli of cells cultivated in the different experimental conditions involving shape and/or FA confinement is reported in **Figure 2.5**. Generally, the distributions were right skewed with long tails towards high moduli values that in some cases surpassed 10 kPa. Thus, the local stiffness of cells in the nucleus region exhibited relatively soft spots with a few hard sites. This made the mechanical state of the cell cortex the nuclear region highly heterogeneous, which made difficult to draw out definitive conclusions on the statistically significant difference of the mean values. Generally, cells cultivated on flat substrates showed an increasing trend of moduli from isotropic (circle, square) to the anisotropic (ellipse, rectangle) shapes. Cells cultivated on the rectangular shapes possessed the highest modulus, whereas cells on control, unconfined, substrates exhibited intermediate values of moduli that were significantly higher than that of cells cultivated on circular micropatterns. This was mainly due to the presence of thick actin stress fibres oriented along the

major axis of the elongated cells, which wrap around the nucleus, exerting greater pressure on it than that measured for isotropic cells. Therefore, micro and nanopatterning approaches aimed at altering the aspect ratio and the stress fibres disposition of adherent cells are indeed a good method to modulate cell stiffness via changes in fibres alignment. The difference of Young's moduli was also evident between the two anisotropic shapes. It was mainly since the stress fibres of elliptical cells could anchor in a smaller space than rectangular ones because of the conformation of the ellipse edge. Indeed, on the curved and pointed lateral edges of the ellipse, cells can form only a few FAs, which limits the formation of a densely packed stress fibres array that strongly compresses the nucleus. This does not occur on rectangular-shaped micropatterns, since the presence of blunt lateral edges enables the formation of a larger number of FAs (**Figure 2.3 a**).

Focusing on the contribution of the nanotopography on the measurement of mechanical properties, we observed that when cells were cultivated on topographic nanopattern, we observed a general decrease of the mean elastic moduli values of cells cultivated on circle, square and ellipse micropattern. However, cells on rectangular micropattern still displayed the highest average moduli. Therefore, anisotropic shapes were effective in altering cell mechanics in order for cells to display a stiffer nuclear region. When shape confinement cooperated with FA confinement, the mechanical stability of cells was somehow disrupted by the presence of the topographic nanograting that presumably reduced the space available for FA formation and growth. This occurrence was not observed on rectangular micropatterns in which the presence of a coaligned nanopattern induced the formation of parallel FAs and actin bundles that stiffened the nuclear region.

The results presented in this study can be useful to design optimal strategies to modulate internal cell tension by substrate micro and nanopatterning favouring changes in the aspect ratio rather than the total spread area of the patterned surfaces.

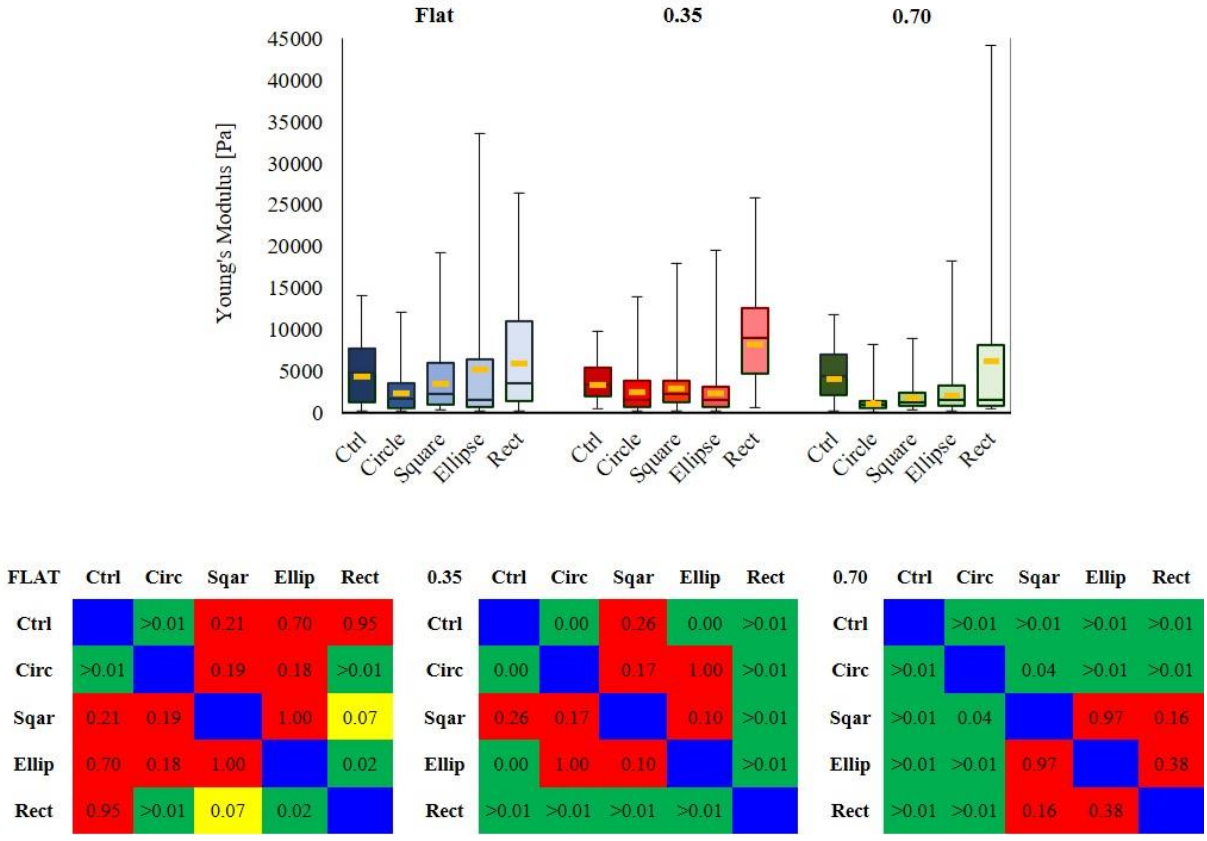

Figure 2.5*: Box and whisker plot of the Young's Modulus of cells cultivated in the different experimental conditions. Black horizontal lines within the boxes represent medians, whereas yellow dashes indicate mean values. The indentation depth for the evaluation of moduli is 200 nm. Significance tables: statistically significant differences of the mean values of the moduli are in green ($p < 0.05$) or yellow ($0.10 < p < 0.05$).*

2.2.3 Relationship between cell shape and nucleus deformation

Membrane stretching and stress fibre assembly are expected to exert mechanical stresses on the nuclear envelope thus altering nucleus shape. Cells on elongated substrates exert a greater cytoskeletal tension along the cell major axis that induces the stress fibres formation and the cytoskeleton stiffening in this direction[4]. This implies significant vertical and lateral compression forces on the nucleus and hence the variation from a round to an elongated nuclear morphology. As can be observed from the images and confirmed by experimental analysis, in elongated cells, the nuclear envelope elongated, and the nucleus exhibited a higher modulus. On the contrary, the nuclei of the circular and square cells showed a lower Young's modulus (**Figure 2.5**) with an almost round morphology. So, while the nucleus remained almost round in the circular and square geometry, the nucleus stretched in the rectangular and elliptical geometry (**Figure 2.6 a**). In a first attempt to assess

the effect of cell shape confinement and topographic pattern on nucleus morphology, we evaluated the aspect ratio (A/R) of the projected area of the nucleus (**Figure 2.6 b**). Nuclei usually displayed an oblong shape, with mean A/R values exceeding 1.25. The distribution of A/R values was rather symmetrical, although long tails could be observed. Cells on control or isotropic micropatterns displayed the lower average values of A/R, whereas nuclei of cells on anisotropic micropatterns were more oblate in shape. However, owing to the large variance in the distribution we were only able to detect a significant difference of the A/R of nuclei of cells on flat elliptical micropatterns with respect to control surfaces, and of nuclei of cells on rectangular micropatterns on a 0.35 µm topography with respect to the control 0.35 µm nanopatterned surface. The only exception to this trend was that of the mean A/R value of cells on elliptical micropatterns with an underlying 0.35 µm topography, which had a relatively low AR. This might be attributed to the presence of a fine nanotopography that impairs FA assembly and growth at the pointed end of the ellipse thus not allowing the formation of highly contractile stress fibres that compress the nucleus laterally.

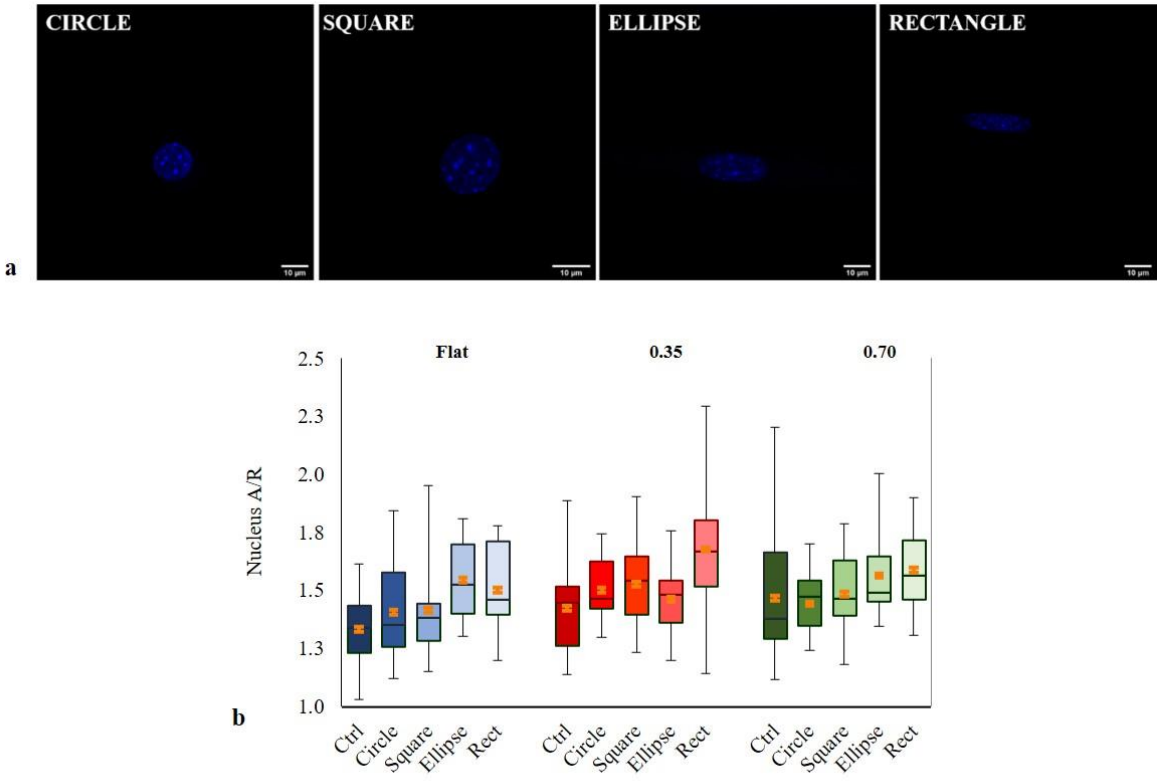

***Figure 2.6**: Box and whiskers of **(a)** Nuclear morphology in different shape cells. Nuclei are immunostained for DAPI (blue). **(b)** the nuclear A/R on flat and nanopatterned substrates, in the cell shape evolution. Asterisks indicate significant difference with respect to the control.*

Lateral compression is only on part of the possible mechanical stresses that the cell membrane and the cytoskeleton can exert on the nucleus envelope. Actin cap fibres are known to exert an axial compression on the nuclear envelope, which may affect the extent of the projected nuclear area. We calculated the projected nuclear areas of cells cultivated on the different substrates and the distributions are reported in **Figure 2.7 a**. We found that larger projected areas of nuclei of cells cultivated on flat rectangles or on rectangular micropatterns on 0.70 nanogratings suggesting that an elongate cell shape and a cytoskeleton arranged in parallel bundles are important factor to exert a compressive stress on the nucleus. However, cells cultivated on rectangular micropatterns on 0.35 nanogratings displayed nuclei with relatively low values of projected area. This observation corroborates the hypothesis that finer gratings (i.e. 0.35 μm pattern) impairs FA formation and the assembly of stress fibres that can effectively stress the nuclear envelope.

Subsequently, we wanted to evaluate the contribution of the different forces exerted by the stress fibres on the nuclei which cause their deformation. We, starting from the hypothesis that the nucleus, in initial conditions, was spherical we introduced three parameters: the axial stretching (the ratio between the height of the deformed nucleus and the initial one), the longitudinal stretching (the ratio between the major axis of the deformed nucleus and the initial one) and the transversal stretching (the ratio between the minor axis of the deformed nucleus and the initial one). Comparing these values, we observed a greater stretching in the longitudinal direction than the axial direction and additionally a greater longitudinal stretching for anisotropic shapes compared to isotropic ones (**Figure 2.7 b**).

Nucleus morphology of cell cultivated on micropatterned, and topographical patterned surfaces was investigated using immunofluorescence staining and z-scanning confocal microscopy. Therefore, 3D structure analysis software was employed to process confocal 3D microscopic images and to generate quantitative information about the morphological feature of SC nuclei.

Different adhesive conditions are known to affect nucleus volume and its mechanical properties. For instance, McKee et al. demonstrated that epithelial cells on 400 nm grating displayed smaller nuclei with respect to nuclei of cells cultivate on 2 μm gratings[5]. Interestingly, cells with bigger nuclei also displayed a higher stiffens. However, more recently Guo et al. reported that increased cell spreading induced a reduction in cell and nucleus volume[6]. The reduction of cell volume is a result of water efflux, which leads to a corresponding increase in intracellular molecular crowding and hence cortical stiffness. These seemingly contradictory results hide the fact that multiple overlapping phenomena dictate the mechanical properties of cells. Cell spreading, membrane tension, osmotic pressure and the cytoskeleton assembly are all likely to affect nucleus morphology and presumably cell stiffness. In this regard, we found that unconfined cells possessed small nuclei, whereas cells on the rectangular

micropatterns possessed relatively large nuclei (significantly larder with respect to control samples). In particular, cells on flat surfaces and 0.70 µm gratings exhibited nuclei with the highest average volume (**Figure 2.7 c**). At this stage, we are not able to exactly define what mechanical input, either osmotic pressure, cytoskeleton or membrane stretching, most effectively affects nucleus morphology, however, the fact that smaller nuclei are observed on control substrates is in agreement with the observation that nucleus volume tracks cell volume. On the micropatterned substrates, however, since the spreading area was the same, it was likely that cytoskeleton assembly and membrane stretching were the dominant factors in dictating nucleus deformation and hence its volume.

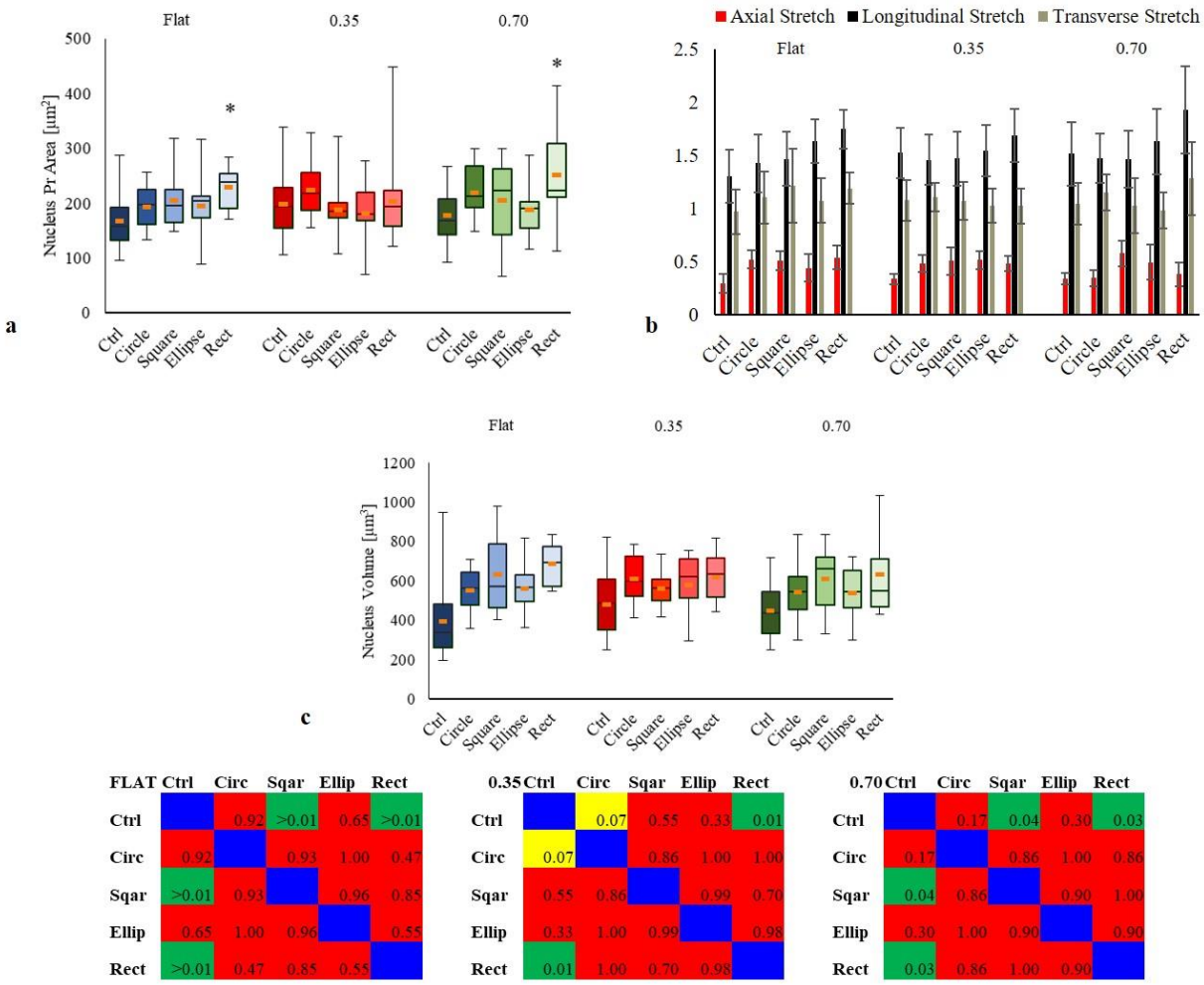

Figure 2.7: *Box and whiskers of* ***(a)*** *the nucleus projected area of shaped cells on flat and nanopattern substrates. Asterisks indicate significant difference with respect to the control.* ***(b)*** *Analysis on the Longitudinal stretch (black), axial stretch (red) and transversal stretch (grey).* ***(c)*** *Box and whiskers of the nucleus volume. Significance tables: statistically significant differences of the mean values of the moduli are in green ($p < 0.05$) or yellow ($0.10 < p < 0.05$).*

To have a clearer picture on the actual deformation experienced by cell nuclei, we calculated the deformation of the nucleus with the shape of the cell, we have assumed this three-dimensional object to be subject to a continuous and homogeneous deformation. When the deformation is homogeneous, it transforms an imaginary sphere into an ellipsoid (three perpendicular axes $\lambda_1 \geq \lambda_2 \geq \lambda_3$) called the Finite Strain Ellipsoid from which it is easy to characterize the style of deformation and its intensity. In this respect, we can consider only two parameters K and D able to completely describe the style of deformation (shape of the ellipsoid) and the amount of deformation (ellipsoidicity, i.e. how far it is from a perfect sphere) respectively. These two parameters do not require knowledge of the radius of the initial sphere, but only the knowledge of the principal axes of the finite strain ellipsoid. By denoting with λ_1/λ_2 the ratio of the longest to the intermediate axis and with λ_2/λ_3 the ratio of the intermediate to the shortest axis, we can distinguish the different shapes of finite deformation ellipsoids by using the values:

$$K = \frac{\ln[\lambda 1/\lambda 2]}{\ln[\lambda 2/\lambda 3]}$$

$$D = \sqrt{[\log[\lambda 1/\lambda 2\,]^2] + [\log[\lambda 2/\lambda 3\,]^2]}$$

Every ellipsoid can be reported as a point in the so-called Flinn diagram (**Figure 2.8 a**), where λ_1/λ_2 is plotted vertically against λ_2/λ_3 and K values describe slopes of lines passing through the origin. The diagonal defines plane strain deformation where the Y-axis of finite strain ellipsoids keeps constant during deformation. Using this graph, we were able to recognize:

- possible cigar-shaped nuclei, if located along the y-axis (K=infinite) where the constrictive deformation is said to occur;
- pancake-shaped nuclei if instead located along the x-axis (K=0) where the deformation is said to be flattened;
- plane deformation (K=1) characterizes nuclei for which the axis λ_2 remains constant despite deformation.

The parameter D indicates the distance between the origin of the diagram (representing the initial sphere) and the ellipsoid.

In the Flinn chart (**Figure 2.8 b**), the measurement performed on each cell were clustered in the lower part of the diagram, suggesting that the preferential nucleus deformation mode was plane/uniaxial contraction (flattening). In the **Figure 2.8 c**, the average values (± s.e.m) were reported. Here, all the

average values lied below the bisector, which represented the true plane strain. Therefore, the uniaxial constrictional strain was not the preferential deformation experienced by cells in any of the culturing conditions we tested. Also, control samples (triangles in the close-up) lied on the right part the diagram suggesting that for these culturing conditions, a more pronounced (i.e. higher intensity) nuclear flattening was observed. For the other culturing conditions, a clear trend of deformations was not present. In the K-D chart (**Figure 2.8 d**) we spot an inverse relationship between the strain intensity (D) and strain shape (K, median value). Median K values were below 1 for all the experimental conditions. For constrictional strains to be effective (and hence K>>1), extensive lateral and axial compressions should occur simultaneously. It seems that the adhesive stimuli provided by our patterns (micro- and nano-) did not produce that mechanical input able to compress nuclei both transversely and axially. Rather, flattening seems to occur with growing level of intensities, i.e. the flatter the shape the more intense (D > 1) was the strain.

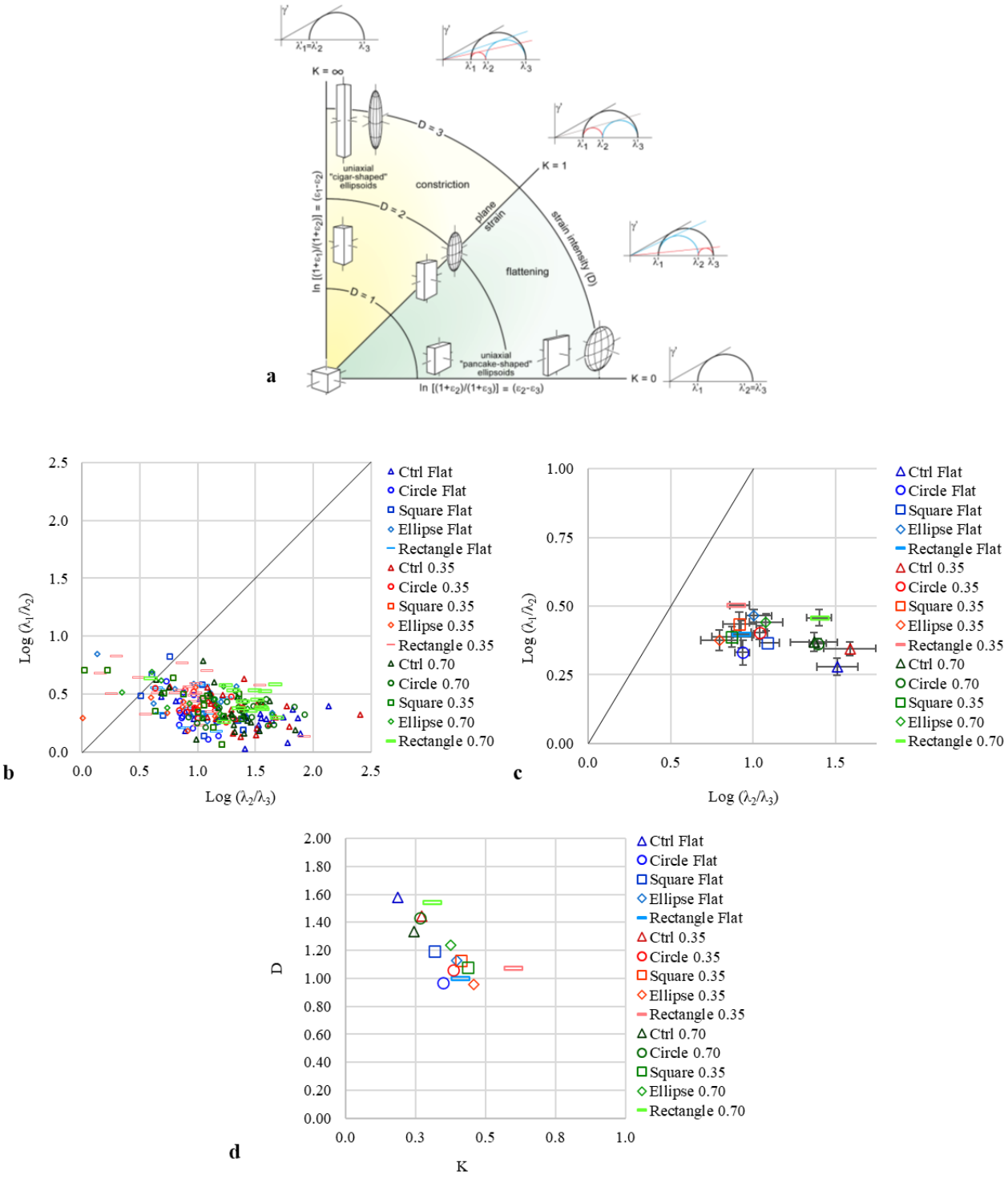

Figure 2.8: *log Flinn diagram of:* ***(a)*** *Strain ellipsoid* ***(b)*** *Strain nuclei of each cell of different shape and* ***(c)*** *the average values (± s.e.m) of strain nuclei of different shaped cells on Flat (blue), 0.35 (red) and 0.7 (green) substrates* ***(d)*** *Evolution of nuclear shape (K) as a function the amount of deformation (D) on Flat (blue), 0.35 (red) and 0.7 (green).*

2.2.4 Cell Mechanics to different indentation

In this section, we report the results of the evaluation of Young's moduli measured by modulating the AFM tip indentation depth. We assume that in this way we can test the mechanical properties of the different cellular compartments. More specifically, we calculated the elastic moduli of cells seeded on different substrates from an indentation depth of 200 nm (extracellular membrane) up to 1000 nm (inner part of the nucleus).

As we can see from the **Figure 2.9 a**, Young's moduli, calculated in the vicinity of the nuclear regions, showed a drop in the proximity of a 400 nm indentation and constant values for deeper indentations. This trend was particularly evident for the non-confined cells cultured on both flat and nanopatterned (0.35 and 0.7) substrates. Several studies in the literature claim that the nucleus of unconfined cells is located approximately 350 nm away from the extracellular membrane[7]. In this respect, the decrease in Young's modulus values measured at an indentation of 400 nm suggests a softer nucleus than the overhead stress fibres. The mechanical properties of cells confined in anisotropic shapes were found to have constant values irrespective of the indentation depth on both flat and non-patterned substrates (**Figures 2.9 b, c, d**). This event was probably due to the presence of a thick structure of actin fibres and a dense network of actin cap, measured by the AFM indenter. Differently, circular, and squared cells cultured on flat, and 0.35 substrates (**Figures 2.9 b, c**) showed an increase in the value of the modulus for deeper indentations (around 600 nm). This trend was presumably caused by the absence of an actin cap (on flat substrates) or to the presence of a thin network of actin caps (on 0.35 substrates) characteristic of isotropic cells. This scenario did not occur in the case of isotropic forms cultured on 0.7 substrates (**Figures 2.9 d**), since the presence of the less dense nanopatterns favoured the assembly of the cytoskeleton and the formation of a reinforcing actin cap located between the plasma and nuclear membranes even in circular and square cells, favouring mostly constant Young's moduli as the indentation varies.

For this purpose, we suppose that the modulus recorded at low indentations reflected the elasticity of the plasma membrane and the resistance of the underlying cellular matter. At higher indentations, the AFM cantilever perceived the contribution of other intracellular structures, like the actin fibres, the nuclear envelope and possibly LINC complexes, which produced higher moduli.

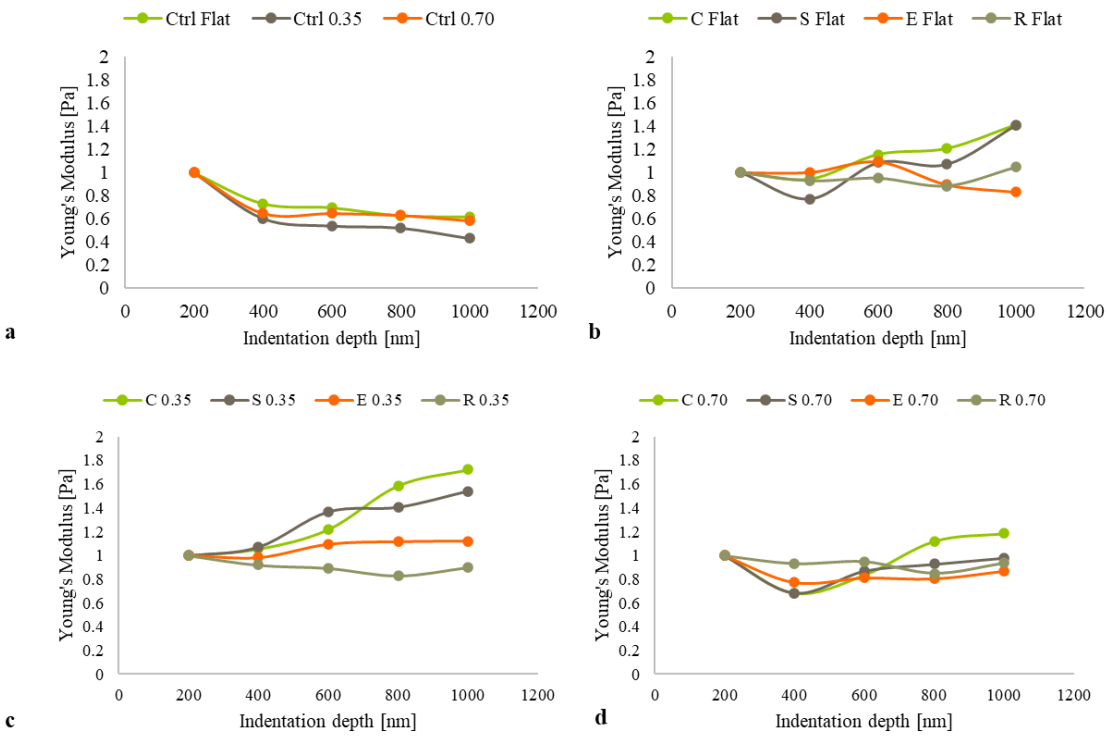

Figure 2.9: *Graph of the median Young's values of fifteen cells for each sample calculated to different indentation depths (200nm,400nm,600nm, 800nm, 1000nm).*

2.2.5 Correlation Plots

To identify possible correlation between morphological and mechanical parameters and owing to the large number of experimental combinations we tested, we plotted correlation matrices of pairs variables. Average value of one variable is correlated to the average value of a different variable and the correlation is expressed in terms of the Spearman's correlation coefficient. In the correlation plots, significant correlations are in red. For the sake of a clearer visualization variables are grouped in different categories. First, we analysed possible correlations of the average young's modulus, calculated at different indentations, with FA characteristics (**Figure 2.10**). From left to right (and from top to down) we indicate: the average of Young's modulus **var1)** at 200 nm; **var2)** at 400 nm; **var3)** at 600 nm; **var4)** at 800 nm; **var5)** at 1000 nm; **var6)** FAs Area; **var7)** FAs Length.

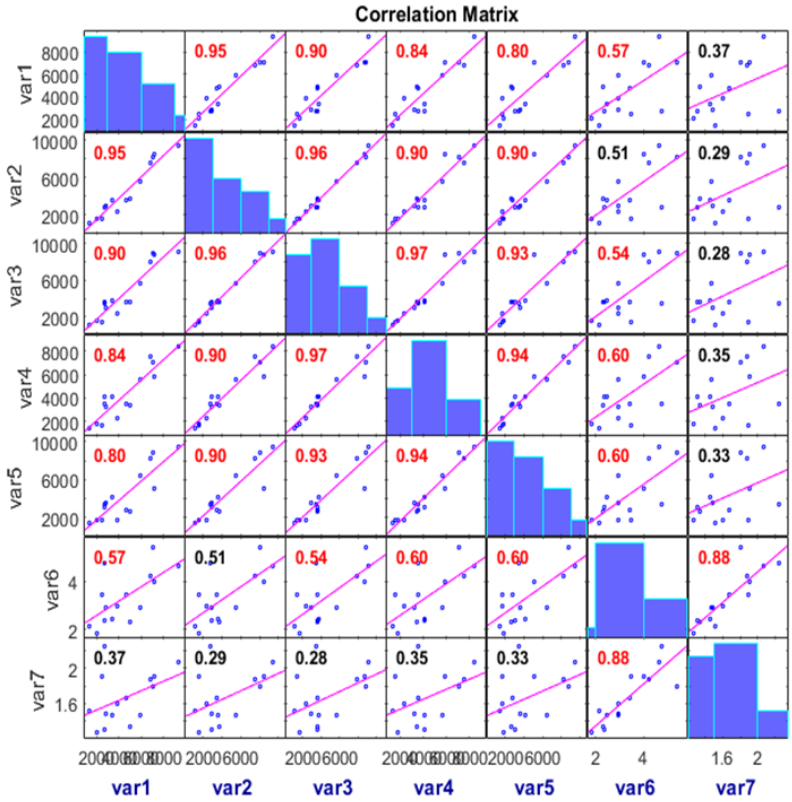

Figure 2.10: *Correlation plot between mechanical nuclear properties and FAs features. From left to right (and from top to down) The average of Young's modulus var1) at 200 nm; var2) at 400 nm; var3) at 600 nm; var4) at 800 nm; var5) at 1000 nm; var6) FAs Area; var7) FAs Length.*

A correlation between the moduli at different indentations was evident, meaning that i. we did not find extensive softening of stiffening at different indentation levels; ii. the trend of Young's moduli among the different experimental setups was conserved. We then found a positive correlation between the Young's modulus of the nuclear region and the FA area. Such a correlation was found irrespective of the indentation depth. Larger FAs characterize a more contractile phenotype of cells, which may induce a stiffening of the cortical acting thus resulting in a higher elastic modulus as recorded by the AFM. As we can see from the graph in **Figure 2.11** both isotropic and elliptic cells were characterized by mechanical properties in the range of 1000 to 7000 Pa, but FAs formed by elliptic cells, as well as rectangular cells, had a larger area than FAs of non-elongated cells. The anisotropic cells formed larger FAs because, by anchoring them at only two ends, although the adhesion area was the same, the cell could elongate in only one direction implying the stretching of the membrane which in turn was counterbalanced by larger adhesion plates. However, the stress fibres of the elliptical cells could anchor in a smaller space than rectangular ones because of the conformation of the ellipse edges. On the curved and pointed lateral edges of the ellipse, cells could form a few FAs, limiting the formation

of a densely packed stress fibres array that strongly compressed the nucleus. This was not the case of rectangular cells, as the presence of blunt lateral edges allowed the formation of a larger number of FAs. Moreover, the rectangular cells showed greater mechanical properties (8000-10000Pa). This was therefore due to the ability of the cells to form more FAs concentrated at the two ends of the cell, thus leading to the formation of stress fibres near the nucleus that compressed it more by exerting a greater force on it. Besides, unconfined cells, on both flat and nanopattern substrates (ctrl), were not affected by any specific effect on the possible cell adhesion area and the FAs could be formed in random positions and dimensions. For this reason, FAs of unconfined cells did not show a particular trend. We can conclude by confirming that a larger FAs area corresponds to a greater cell ability to anchor to the substrate and therefore the force that the stress fibres exert on the nucleus will be greater. Finally, we also found a more obvious corelation between FA length and area, stating that longer FAs were also characterized by a larger area.

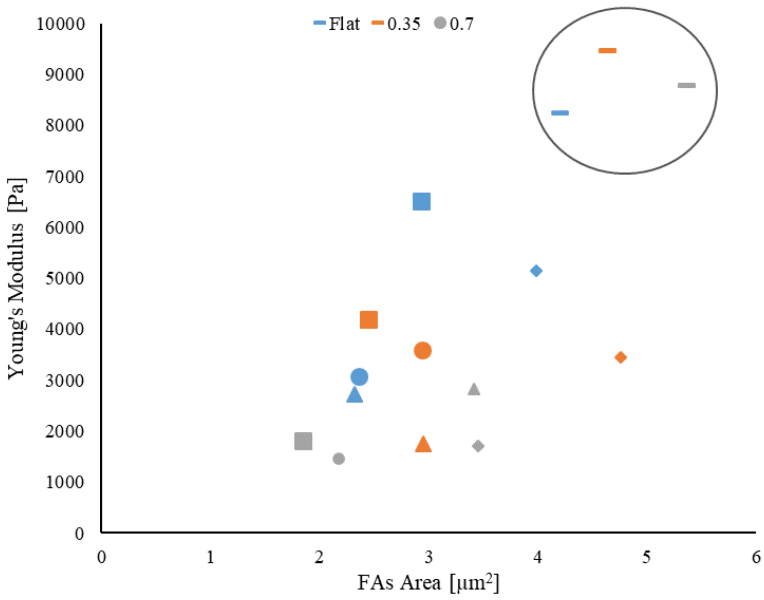

Figure 2.11: *Evolution of FAs area as a function of Young's modulus for (▲) ctrl, (●) circular, (■) square, (◆) elliptical and (▬) rectangular cells on Flat (blue), 0.35 (red) and 0.7 (grey) substrates.* The indentation depth is 10000 nm.

Subsequently, in **Figure 2.12** we compared average values of young's moduli of the nucleus region (evaluated at different indentations) with the morphometric parameters of nuclei. So, we show the correlation plot between mechanical and morphological nuclear properties. From left to right (and from top to down) the variables considered are: the average of Young's modulus **var1)** at 200 nm;

var2) at 400 nm; **var3)** at 600 nm; **var4)** at 800 nm; **var5)** at 1000 nm; the Nucleus **var6)** Aspect Ratio; **var7)** Volume; **var8)** Projected Area.

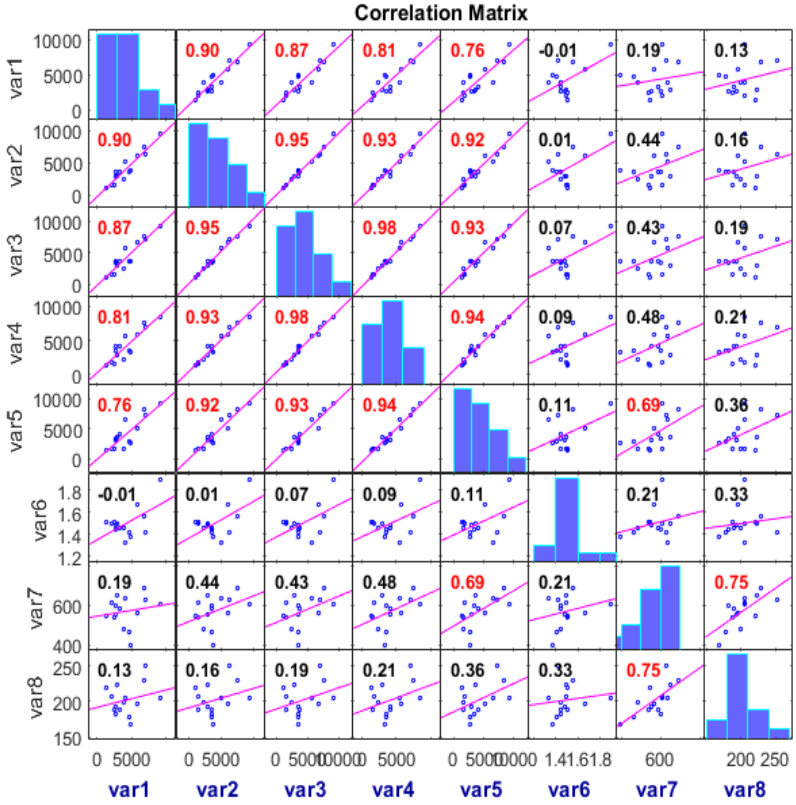

***Figure 2.12**: Correlation plot between mechanical and morphological nuclear properties. From left to right (and from top to down) Young's modulus var1) at 200 nm; var2) at 400 nm; var3) at 600 nm; var4) at 800 nm; var5) at 1000 nm; the Nucleus var6) Aspect Ratio; var7) Volume; var8) Projected Area.*

As we expected, there is a strong correlation between the moduli at various indentations, indicating a consistent trend in modulus variation with indentation. τ goes from a maximum of 0.98 to a minimum of 0.76 for the relation between Young's moduli calculated by 200 to 1000 nm of indentation. We did not find any correlations between moduli and the nucleus A/R and projected area. Instead, we found that the correlation coefficient of moduli with nucleus volume increased with the indentation depth (from 0.19 up to 0.69). A significant correlation (0.69) was found for moduli calculated at 1000 nm of indentation depth. The very low correlation coefficient found for 200 nm indentation suggested that at small values of indentations depth the AFM only sampled the elasticity of the top structures constituting the apical surface of the cell, i.e. cell membrane, cytoplasm matter, apical actin. Starting from 400 nm indentations the correlation coefficient increased dramatically (above 0.4) suggesting that from this indentation value the AFM tip started perceiving the presence

of the nucleus that contributed to defining the overall mechanical properties of the cell. Larger nuclei influenced more the cell's elasticity as perceived by the AFM, which resulted in increased moduli values. To sum up, in agreement with McKee et al., we found that when the nucleus volume of confined cells increased, the elastic modulus of nuclei increased (**Figure 2.13**)[5]. We assume that this result can depend on the effect of the proximity of the nucleus to the cellular membrane. It has been proven that when the volume of the rigid nucleus increases in the cell, the resistance to deformation measured over the nuclear region, increase due to the combined responses of the cell membrane, cytoskeleton, and nucleus, whose proximity to the outer dorsal membrane is decreased due to its increased volume. Conversely, when the nucleus is smaller, more cytoplasmic space exists between the nucleus and the outer cell membrane, thus offering decreased resistance to deformation by the indenting probe. Another hypothesis is that this behaviour may be caused by the "internal" mechanical forces such as resistance forces due to chromatin deformation and internal pressure (fluid content and chromatin decondensation).

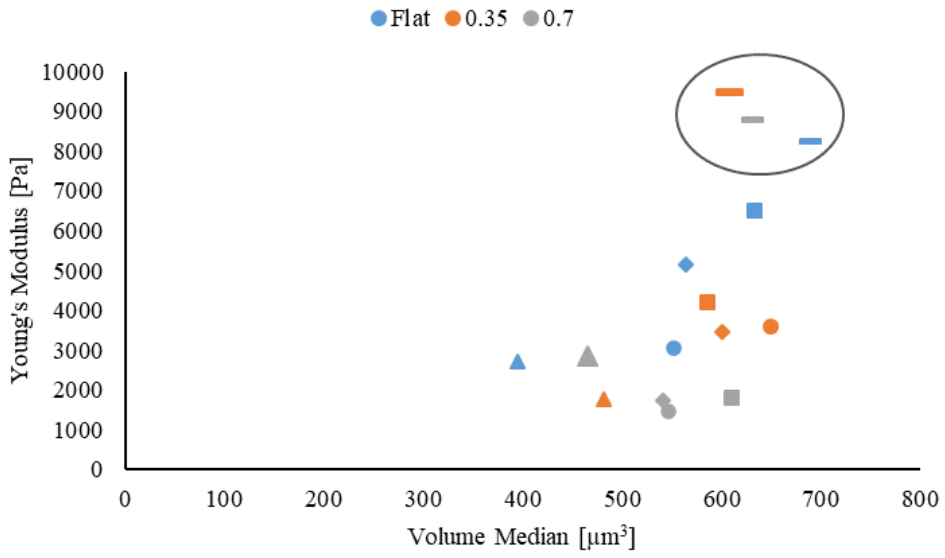

Figure 2.13: *Evolution of nuclear volume as a function of Young's modulus for (▲) ctrl, (●) circular, (■) square, (◆) elliptical and (▬) rectangular cells on Flat (blue), 0.35 (red) and 0.7 (grey) substrates.* The indentation depth is 10000 nm.

Finally, we investigated possible correlation between moduli and nucleus deformation (**Figure 2.14**). The latter was measured in terms of the median value of the strain shape parameter K, average value of the strain intensity D, and principal stretches, i.e. longitudinal, transverse and axial.

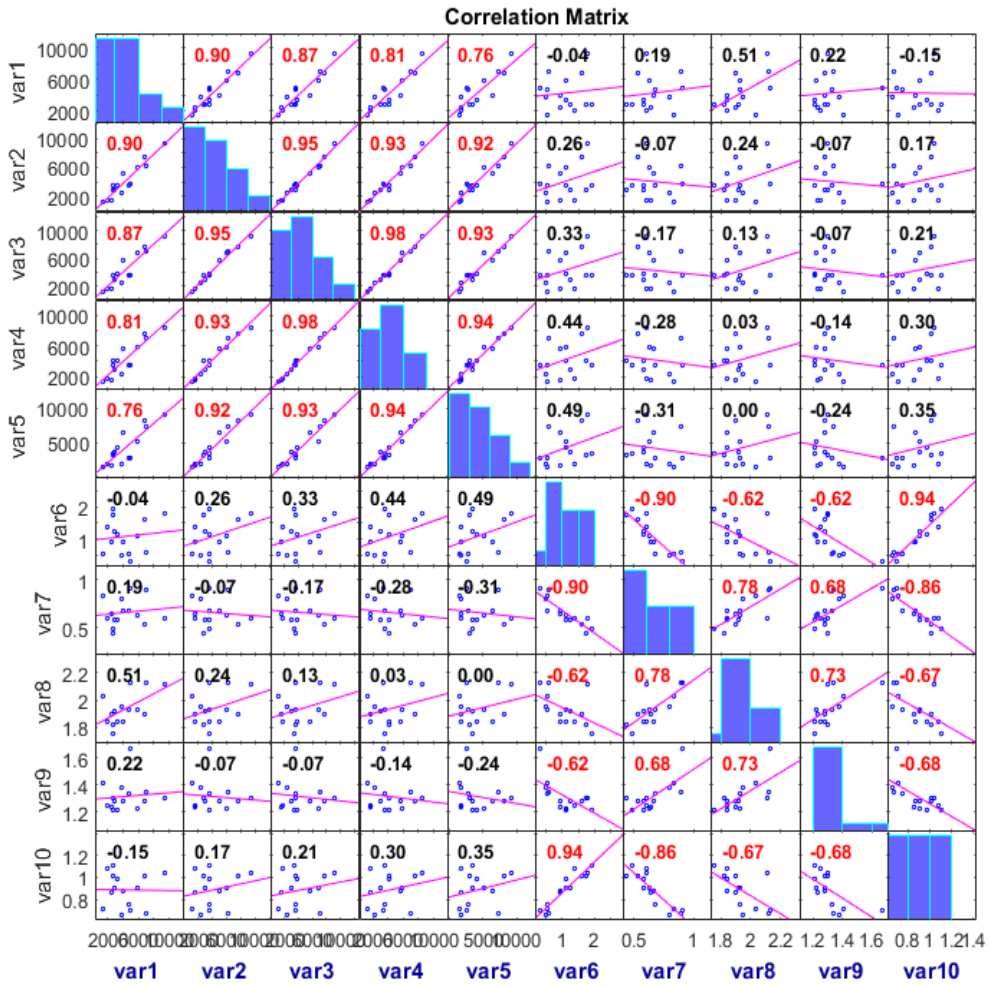

Figure 2.14: *Correlation plot between mechanical and deformation nuclear properties. From left to right (and from top to down) the variables considered are: the average of Young's modulus var1) at 200 nm; var2) at 400 nm; var3) at 600 nm; var4) at 800 nm; var5) at 1000 nm; var6) K; var7) D; var8) Nucleus Axial Stretch; var9) Nucleus Longitudinal Stretch; var10) Nucleus Transversal Stretch.*

We were not able to identify any significant correlation between the moduli and the strain-related parameters. However, we found that correlation coefficients of the average modulus and the strain shape K increased with increasing indentation depths, i.e. -0.04 for moduli calculated at 200 nm up to 0.49 for moduli calculated at 1000 nm. At high indentation depths, nuclei characterized by high K values were found in cells having high average moduli in the nuclear region. Although non-significant, we may speculate that such a positive trend, that is relevant for high indentation depts, arises from the stiffening effect provided by the actin cytoskeleton compressing the nucleus. In our experiments, K rarely surpasses 1, meaning that the strain shape is mostly in the form of a plane strain or flattening strain for low K values. In both cases, actin bundles in the form of an apical cap, are required to compress the nucleus axially. The presence of these dynamic structures exerting

mechanical forces on the nucleus are expected to provide an additional stiffening effect, which is probed by the AFM tip only at sufficiently deep indentations. The other significant correlations appearing in the correlation plot pertain the strain related variables. This is not surprising since K and D are calculated from the geometrical features of the deformed nuclei, an information that is also contained in the principal stretches.

2.3 Conclusion

In this chapter, we explored the possibility to integrate biochemical and biophysical signals into synthetic culturing platforms. We exerted a fine control on various aspects of hTERT behaviour by fabricating culturing devices that capture the complexity of the extracellular microenvironment and in principle synchronize the events that regulate cells function and fate. For this purpose, we fabricated engineered material surfaces with tailored adhesive characteristics to direct SC behaviour in a deterministic manner and for relevant in vitro applications. More specifically, we explored how material signals dictate and define the formation, spatial positioning, and orientation of focal adhesions, which in turn affect the formation and organization of actin fibres and cytoskeleton. Moreover, we demonstrate that the structure of the cytoskeleton defines the magnitude and orientation of tensile forces exerted on the nuclear envelope and together with the signalling proteins of Focal Adhesions affect the nuclear mechanical properties. Therefore, we studied how to tune cell mechanics using specific geometrical patterns and potentially modulating them with the presence of nanometric grooves. The presence of nanogrooves influences the stability, spatial positioning and growth of the FAs. The presence of grooves helps the cells in FAs growing especially in the case of anisotropic cell shapes. In this regard, our experimental data could be incorporated into a mathematical model so that we can predict the development of cell mechanical characteristics from the shape imposed on cells and the constraints imposed on FAs. Since the processes involved are very complex and depend on many factors, numerical simulations should be a valuable tool to test hypotheses and investigate the effects of single physical phenomena, and thereby increase our understanding of the underlying processes. In the last years, several mathematical models have been proposed to explain how topographical patterning can predict the positions, shapes and sizes of the FAs and the remodelling of fibres[8–10]. They mainly proved that SFs tend to establish a homeostatic equilibrium with their surroundings, and this leads to the final fibre organization. These models have been successively coupled with thermodynamic models for FA maturation and signal production and diffusion[11]. In our study we support the recent computational framework used by Vigliotti et al.[12]. In the proposed theory, the ability of the FAs to form and of the actin fibres to orient on flat and linearly patterned substrates was evaluated. The modelling scheme showed to capture some key experimental observations including the cell capacity to orient themselves randomly on flat substrates or with groove pitches less than about 150 nm and to align themselves with the direction of the grooves on substrates with larger pitches. Moreover, actin fibres bridge over the grooves on substrates with

groove pitches less than about 150 nm but form a network of fibres aligned with the ridges, with nearly no fibres across the grooves, for substrates with groove pitches greater than about 300 nm. In agreement with our experimental observations, this model rationalizes the responsiveness of cells to the topography of substrates based on the complex feedback involving focal adhesion formation on the ridges, the triggering of signalling pathways by these adhesions and the activation of stress fibre networks by these signals.

2.4 Experimental Section

2.4.1 General Materials

Trypsin and paraformaldehyde were provided from Gibco, Thermo Fisher Scientific. TRITC phalloidin, Triton X-100, bovine serum albumin (BSA) and fibronectin solution were provided by Sigma-Aldrich. Anti-vinculin monoclonal antibody was provided from Chemicon (EMD Millipore), Alexa Fluor 488 conjugated goat anti-mouse antibody and Deep Red Anthraquinone 5 (DRAQ-5) were purchased from Abcam. ASC52telo, hTERT immortalized adipose derived Mesenchymal stem cells were purchased from ATCC.

2.4.2 Sample Preparation

The Polycarbonate (PC) samples consisted of a 4 cm^2 area containing: flat substrates (**F**), parallel and straight channels with a groove and ridge width of 0,7 µm and a depth of 0,20 µm (**0.7**), and parallel and straight channels with a groove and ridge width of 0,35 µm and a depth of 0,14 µm (**0.35**). Before being activated, each sample is washed in 100% ethanol and thoroughly dried.

2.4.3 Micropatterning protocol

PC substrates are activated by exposure to O_2 plasma (Harrick Scientific Products, Pleasantville, NY, USA) for 1 min and to deep UV Printer (4D cell, Montreuil, France) for 10 min respectively. Then the samples are incubated for 1 h with 0.1 mg ml^{-1} poly-L-lysine-g-poly(ethyleneglycol) (PLL(20)-g[3.5]-PEG(2); SuSoS Surface Technology, Dubendorf, Switzerland) at room temperature (50 µL for each sample). After washing with distilled water, the treated surface was illuminated with deep UV light through a photomask.

The 4Dcell photomask is a quartz mask with a chromium designed coating for the aim of the micropatterning experiment. It is used for the printing of the micropatterns on slides, with deep UV. Our mask is characterized by four geometric figures having the same surface area: square, circle, rectangle and ellipse of the dimensions represented in **Figure 2.14**. The 4Dcell quartz mask is washed with absolute ethanol and it is illuminated for 10 min using the deep UV Printer, with its brown side facing the lamp. This makes the brown side of the mask hydrophilic. 3µL of millipore H_2O are added

onto the brown side of the 4Dcell quartz mask and the PEGylated side of the sample is gently dropped onto the mask. Using the deep UV Printer, the 4Dcell mask is illuminated for 8 min with the silver side facing the lamp. 5 mL of distilled water are added on the mask to help detach the slides from it. The activated side is than incubated 1h at room temperature with 50 µL of fibronectin (final concentration of 25 µg ml^{-1}) and after it is rinsed with water.

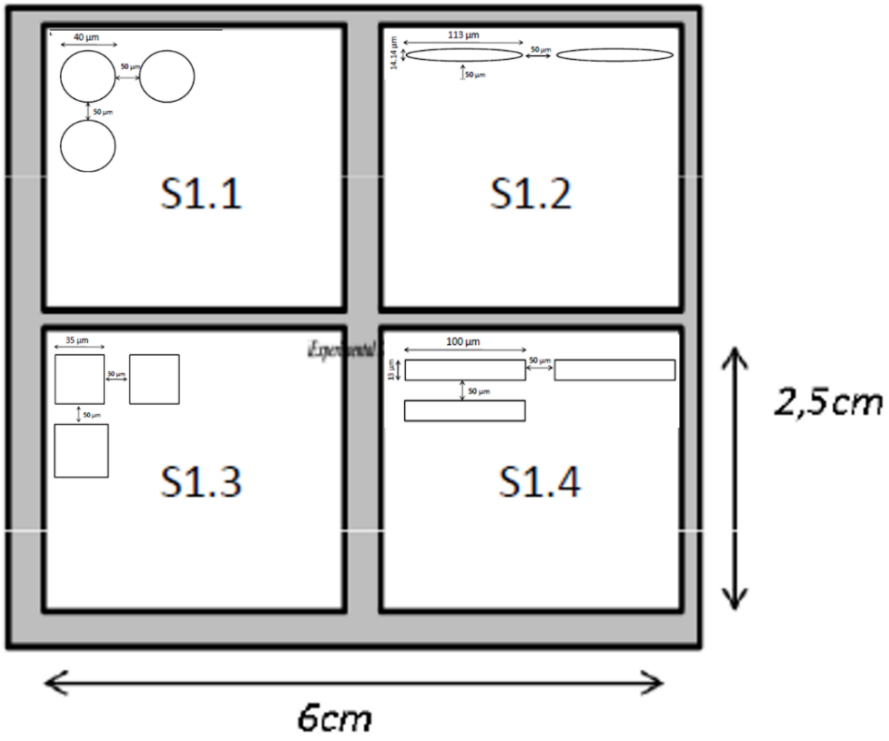

Figure 2.15: *The 4Dcell photomask design. It consists in four geometric figures having about 1500 µm² surface area: square, circular, rectangular, and elliptical shape.*

2.4.4 Plating of the cells

ASC52telo, hTERT immortalized adipose derived Mesenchymal stem cells are cultured in Mesenchymal Stem Cell Basal Medium (ATCC PCS-500-030). To make the complete growth medium, Mesenchymal Stem Cell Growth Kit (ATCC PCS-500-040) for Adipose and Umbilical-derived MSCs – Low Serum Components and G418 is added to the base medium. Cells are detached from the culture plate and centrifuged to remove traces of trypsin; the enzyme used to detach the cells. They are then resuspended in the culture medium and 25.000 cells are seeded per sample. Cells

were cultured at 37 °C in a humidified atmosphere of 95% air and 5% CO_2. Cells should be spread on the patterns 1h after plating.

2.4.5 AFM for Sample Surface Characterization

An atomic force microscope JPK NanoWizard II (JPK Instruments, Germany) was used to acquire images of PC samples. An Axio Observer Z1 microscope (Zeiss, Germany) was combined to the AFM to control tips and sample position. Silicon Nitride probes (MLCT, Bruker, USA), with a spring constant of 0.01 N/m, were used in contact mode, in air, at room temperature. Raw images were corrected by the JPK data processing software using a standard procedure (flatten, planefit and artifact lines caused by the tip attachement and removal). The scale indicating the sample height or deflection was adjusted to limit the gap between high and low regions. Using this software, we measured the cross sections through the images, and we obtained the samples 3D views.

2.4.6 Fixed-cell Staining

Cell fixation was performed by incubating cells in a 4% paraformaldehyde solution for 15 minutes. Then, cells were permeabilized with 0.1% Triton X-100 in PBS for 15 min. Samples were blocked in 3% bovine serum albumin in PBS (Sigma-Aldrich) for 1 h to avoid non-specific binding. FAs were labelled by incubating samples with an anti-vinculin monoclonal antibody (dilution 1: 400, Sigma-Aldrich) for 1 h at room temperature. After incubation, substrates were washed three times with Triton-PBS (3 min per wash) and incubated with Alexa Fluor 546 conjugated goat anti-mouse antibody (dilution 1: 1000) for 1 h at room temperature. Actin filaments were stained by incubating samples with Alexa Fluor 488 phalloidin (dilution 1: 200) for 1 h at room temperature. Finally, cells were incubated for 15 min at 37 °C in DRAQ-5 solution (dilution 1:200) or in DAPI solution (dilution 1:10000) to stain nuclei. Samples were thoroughly rinsed in PBS and mounted on glass slides by using mounting media (Sigma-Aldrich). Fluorescent images of FAs and actin bundles were collected with a Leica TCS SP5 confocal microscope (Leica Microsystems). Samples were excited at 488 nm (actin), 543 nm (vinculin) and 633 (nuclei), and the emissions were collected in the 500-530 nm, 560-610 nm and 650-720 nm ranges, respectively.

2.4.7 AFM for Cell Mechanics

A JPK NanoWizard II AFM was used to measure mechanical properties of living cells. Soft cantilevers (PNP-DB, NanoWorld, nominal spring constant 0.06 N/m) were used to investigate cell mechanical properties. The AFM was mounted on a Zeiss LM 510 confocal microscope to enable coaligning the AFM tip with cells. The mechanical properties of the cell cytoplasm were measured in different points but in proximity of the cell nucleus, by performing a force mapping. Force curves were typically recorded at a scan rate of 1 Hz, corresponding to a maximum loading rate of 1 nN/s and a maximum force of 1 nN. Typically, 64 force curves were measured over a cell area of 10 x 10 μm. Mechanical properties of cells, in terms of Young's modulus (E) values were estimated by fitting the force-indentation curve with Hertzian model for linearly elastic materials. In order to investigate the different cell compartments E was evaluated for five different indentations: 200 nm, 400 nm, 600 nm, 800 nm and 1000 nm, for each force curve. AFM measurements were carried out on fifteen cells per sample. Once the Young's modulus map was obtained, we calculated the mean, median and standard deviation of these values for each cell.

2.4.8 Analysis of nuclear morphology and FAs Shape

Digital images of the different cell compartments stained using immunofluorescence techniques, were analysed with the command "analyze particles" in Fiji. This allows us to extract information about, area, A/R, orientation and shape of the nuclei and FAs by analysing a set of 20 single isolated cells for each sample. The analysed set of cells came from different samples carried out in analogous conditions. Nuclei/FAs orientation on linear pattern, was defined as the angle that the principal axis of inertia formed with a reference axis, i.e the pattern direction in the case of linear or the horizontal axis for flat surfaces.

Nuclear volume was calculated by acquiring 30 z-stacks per sample and using a custom written script in ImageJ. Briefly, Z-stack sections of nuclei were binarized. The area of each section was multiplied by the voxel height (Vh) and the volume was expressed as the sum of the areas*Vh comprising the stack. The average, median and standard deviation values of all the parameters listed above were calculated. Statistical significance was assessed through Kruskal-Wallis test (run in Matlab) with level of significance $p < 0.05$.

2.4.9 Plotting cell/nucleus mechanical properties and Correlation Plot

Once obtained the data, we used Microsoft Excel to compute the average, the median and the standard deviation of each cell's Young's modulus, corresponding to 64 force curves. We took the points in which the nucleus was visible in order to compute its mechanical properties. Once again, we plotted the Young's modulus average value for each cell of the sample. The "corrplot" command in MatLAB was implemented to evaluate the Spearman's correlation coefficient between morphological and mechanical properties of the nucleus.

2.5 References

1. Bhadriraju, K. & Chen, C. S. Engineering cellular microenvironments to improve cell-based drug testing. *Drug Discov. Today* **7**, 612–620 (2002).

2. Balaban, N. Q. *et al.* Force and focal adhesion assembly: a close relationship studied using elastic micropatterned substrates. *Nat. Cell Biol.* **3**, 466–472 (2001).

3. Kim, D.-H., Chambliss, A. B. & Wirtz, D. The multi-faceted role of the actin cap in cellular mechanosensation and mechanotransduction. *Soft Matter* **9**, 5516 (2013).

4. Kumar, A., Makhija, E., Radhakrishnan, A. V., Jokhun, D. S. & Shivashankar, G. V. Chapter 2 - Cell geometric control of nuclear dynamics and its implications. in *Mechanobiology in Health and Disease* (ed. Verbruggen, S. W.) 55–76 (Academic Press, 2018). doi:10.1016/B978-0-12-812952-4.00002-7.

5. McKee, C. T., Raghunathan, V. K., Nealey, P. F., Russell, P. & Murphy, C. J. Topographic Modulation of the Orientation and Shape of Cell Nuclei and Their Influence on the Measured Elastic Modulus of Epithelial Cells. *Biophys. J.* **101**, 2139–2146 (2011).

6. Guo, M. *et al.* Cell volume change through water efflux impacts cell stiffness and stem cell fate. *Proc. Natl. Acad. Sci.* **114**, E8618–E8627 (2017).

7. Wang, N., Tytell, J. D. & Ingber, D. E. Mechanotransduction at a distance: mechanically coupling the extracellular matrix with the nucleus. *Nat. Rev. Mol. Cell Biol.* **10**, 75–82 (2009).

8. Deshpande, V. S., McMeeking, R. M. & Evans, A. G. A bio-chemo-mechanical model for cell contractility. *Proc. Natl. Acad. Sci.* **103**, 14015–14020 (2006).

9. Kaunas, R., Hsu & Deguchi. Sarcomeric model of stretch-induced stress fiber reorganization. *Cell Health Cytoskelet.* 13 (2010) doi:10.2147/CHC.S14984.

10. Ristori, T., Vigliotti, A., Baaijens, F. P. T., Loerakker, S. & Deshpande, V. S. Prediction of Cell Alignment on Cyclically Strained Grooved Substrates. *Biophys. J.* **111**, 2274–2285 (2016).

11. Pathak, A., McMeeking, R. M., Evans, A. G. & Deshpande, V. S. An Analysis of the Cooperative Mechano-Sensitive Feedback Between Intracellular Signaling, Focal Adhesion Development, and Stress Fiber Contractility. *J. Appl. Mech.* **78**, 041001 (2011).

12. Vigliotti, A., McMeeking, R. M. & Deshpande, V. S. Simulation of the cytoskeletal response of cells on grooved or patterned substrates. *J. R. Soc. Interface* **12**, 20141320 (2015).

Chapter 3

3 Cellular response on dynamic surfaces

3.1 Introduction

In an in vivo context, the extracellular matrix (a network of pores, fibres, ridges of micro or nano-metric size) continuously changes its biochemical/biophysical features displaying different signals to cells in a spatio-temporal dependent manner[1]. For this purpose, temporal variations of the ECM, including changes in the microarchitecture, play a crucial role in regulating different biological processes in vivo as gene transcription and morphogenesis, and therefore also the progression of pathologies[2,3]. Mesenchymal stem cells immortalized with hTERT are a promising cell source for regenerative therapies given their multipotent nature[4,5]. These cells are finely sensitive not just to soluble differentiation factors, but also to biophysical cues arising from or induced by the cellular microenvironment, including substrate stiffness[6], cell morphology[7], and dynamic mechanical perturbation[8]. These exogenous mechanical cues can influence the cytoskeletal organization, cell proliferation, chromatin remodelling and nuclear stiffness. Several well-known methods have allowed a deep understanding of the mechanisms underlying the cell's recognition and reaction to signals, but specific aspects such as multi-signal stimulation or dynamic changes are still unclear. This calls for new culture systems designed to visualize biophysical material signals according to predefined spatio-temporal programs. Recently, stimulus-responsive materials have been used as 'dynamic' substrates because they are powerful tools to prepare dynamic cell culture platforms[9,10]. More specifically, special attention has been focused on light-sensitive materials, exploiting the peculiarity of light to be precisely localized over a substrate, programmed in time and space, and remotely addressable at an appropriate wavelength without compromising cell viability. Among the various light-sensitive materials, those containing azobenzene molecules have shown the ability to inscribe topographical features dynamically by providing remarkable surface mass transport under appropriate illumination conditions[11]. The mass transport is induced by a reversible process of trans-

cis-trans isomerization of a special class of azobenzene molecules (the push-pull type such as Poly Disperse Red 1, pDR1[12]).

3.2 Results and Discussion

In this section, pDR1 azofilms were used as cell culture supports to inscribe linear topographic patterns and to study the dynamic cell response to time-varying topographic signals. The confocal microscope set-up allowed the inscription of micron and submicron-scale structures on azopolymers enabling them to directly induce dynamic topographic cues to live cells at different times or locations and study cell response in a real-time manner[13]. Given the centrality of the nucleus in directly perceiving mechanical stresses and adapting transcriptional activities with mechanical inputs, this study aimed to investigate how cellular and nuclear properties changed when cells were exposed to topographical signals variable over time, and how these changes might affect the cell mechanobiology. More specifically, we examined the nuclear mechanics and morphology of hTERT cells when they move from isotropic and anisotropic flat substrates to substrates with aligned nano-ridges, and we evaluated how these behaviours vary over time (from 0 to 48 h following nanopattern inscription). More in details, among the different culture conditions analysed in the previous chapter, except for the controls, we observed that the micropatterned samples of circular and rectangular cells cultured on both flat and 0.7 surfaces were the most susceptible to nuclear deformation. For this reason, in this section we choose to analyse the response of circular and rectangular cells cultured on flat surfaces to dynamic topographic stimuli composed of parallel and straight channels with a groove and ridge width of approximately 0.7 µm.

Moreover, the information obtained from the static cell cultures constitutes the basic principles from which we could compare cell behaviour in dynamic conditions. Our objective was to investigate cellular response in terms of correlation between cell mechanics - nucleus deformation - FAs distribution on surfaces on which nanotopography varies dynamically. Subsequently, we considered how the mechanical characteristics of the nuclear region were related to the density of chromatin and lamins A/C, an important nucleoskeletal protein believed to modulate transcription and to mechano-regulate the genome. This was possible by using high-resolution confocal images to correlate nucleus mechanics with nuclear envelope integrity. In particular, 3D reconstructed images were a useful tool able to show the indentation effect of actin stress fibres on specific regions of the nuclear envelope. Observing how nuclear mechanics influences nuclear activity, i.e. analysing the configuration of chromatin we had information about the stem cells transcriptional status. Chromosomes are compartmentalized into discrete territories and nuclear morphological changes and nucleoskeletal

integrity can have a direct effect on chromatin topology, condensation, and accessibility to transcription sites.

3.2.1 Pattern Inscription on Azopolymer Substrates

hTERT cells were seeded on pDR1m flat substrates, which had previously been micropatterned using a photomask (the same technique used in the static case) to produce circular (C) and rectangular (R) adhesive islands with the same area (1500 μm^2). 24 hours after seeding, we embossed a linear pattern on the initial flat surface using the light polymer activation technique. Single-photon confocal microscopy was used to emboss precise and complex submicrometric patterns of the desired size on pDR1m thin films. Since the maximum absorption band of this azo-polymer is 467 nm, the laser sources with wavelength values of both 405, 488 and 514 nm could be used to induce the continuous trans-cis-trans isomerization of pDR1m molecules, favouring the resulting surface mass migration[14]. The laser beam path could be controlled via software by drawing a specific region of interests (ROIs) in which the laser was activated only in the selected areas with a high spatial resolution (nm order). The peculiarity of the confocal microscope set-up enabled us to produce complex topographies by simply changing the shape, the dimension, and the direction of the ROIs without compromising cell viability. Since topographic patterns were generated by laser-induced mass displacement, it was reasonable to expect that the features would be affected by the processing parameters. Before determining the final settings, we carried out a careful parameter optimization analysis, assessing in detail the influence of laser intensity, laser dwell time and writing conditions on the resulting nanopattern features (*SI* data not shown).

The final nanopattern consisted of 7 rectangular ROIs in the case of the rectangular cell and 17 rectangular ROIs in the case of the circular cell in both cases arranged horizontally to the scan direction, resulting in linear ridges. These ROIs were produced in proximity of the constrained cell and were irradiated for 60 s with Argon laser at 488 nm, generating easily parallel gratings (**Figure 3.1**). Using topography analysis performed with AFM we verified the width of each ridge (0.70 ± 0.09 μm) the pitch between two ridges (1.40 ± 0.04 μm) and the height of the ridges (0.20 ± 0.02 μm).

In conclusion, using these techniques, we can vary nanotopographic pattern features and surface adhesive island shape, to evaluate the topographical contribution on the FAs maturation, cellular spreading, and hence nuclear mechanical and morphological properties.

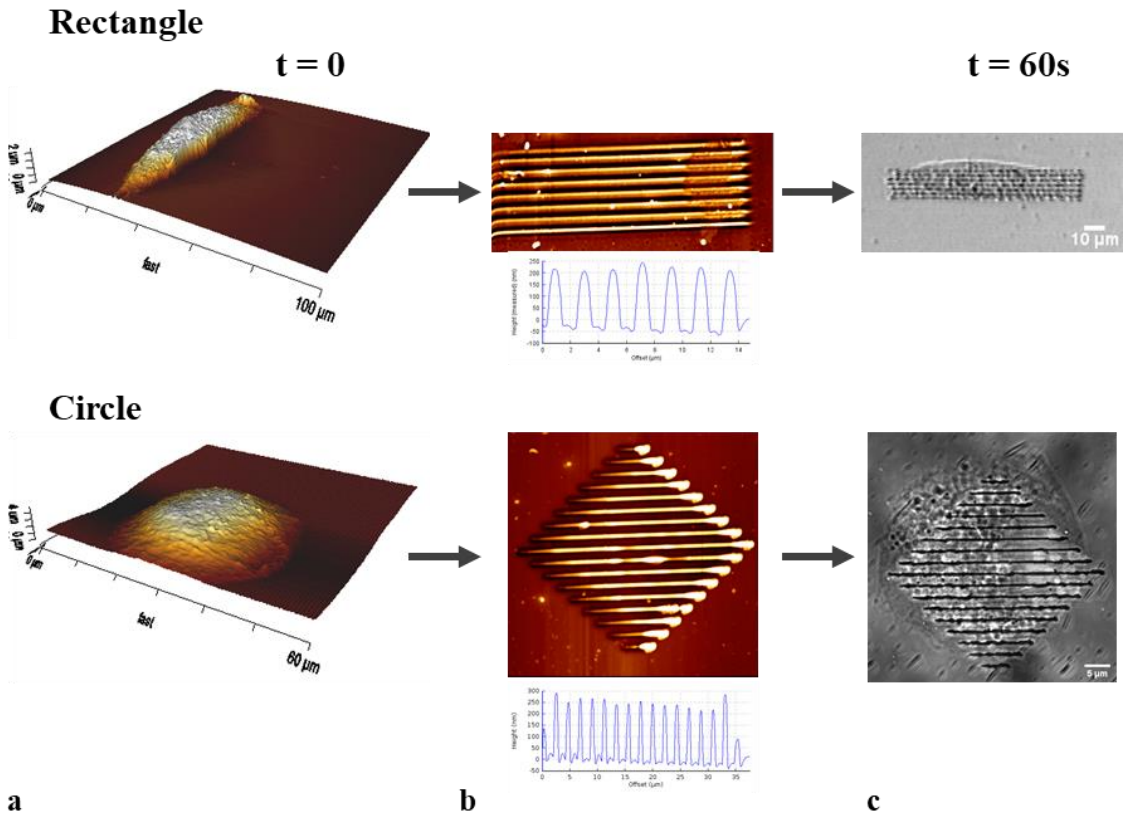

Figure 3.1: (a) *the 3D reconstruction of the rectangular and circular cells on flat substrates.* ***(b)*** *AFM images of patterned surfaces of the azofilms. The figure above represents the bidimensional projection of the topographic reliefs and the figure below shows the cross-section profiles* ***(c)*** *Confocal-inscribed linear pattern on pDR1m. Confocal images of linear pattern with periodicity of 0.7 µm. The sample was irradiated with Argon laser at 488 nm for 60 s.*

3.2.2 Cell mechanic on Dynamic Topographic Patterns

Changes in the FA assembly in response to the extracellular topography led to changes in cytoskeletal structure, and ultimately to changes in cellular properties and their ability to transduce mechanical signals from the ECM. Changes in cell-ECM interactions are often associated with changes in the expression of integrins and molecules in the FA plaque, which in turn can influence F-actin organization and thus the mechanical properties of the cell properties[15].

Using AFM, we have carefully evaluated the mechanical properties of living cells. However, due to the heterogeneous and dynamic nature of living cells, it is difficult to isolate the influence of individual internal cellular components on the response of the whole cell to the biophysical signal. Nevertheless, we found that changes in the elastic modulus of cells aligned to the underlying nanopattern could thus be correlated with changes in the shape-dependent structure of the cytoskeleton. Understanding the relationship between cell mechanics and cytoskeletal composition

required simultaneous measurement of cell stiffness and quantitative imaging of the cell's cytoskeleton. For this purpose, the assembly of cytoskeleton structures was investigated using immunofluorescent staining and confocal microscopy (**Figure 3.2 a**).

First, we measured Young's moduli of rectangular cells in proximity to the nuclear region. Despite the change of surface topography, the values of the cell modulus did not change in time, i.e., the average modulus was not different from the value measured immediately before the pattern inscription (**Figure 3.2 b** blue indicators). As expected, also the elastic moduli of cells cultivated on control surfaces (i.e., on which the topographic pattern was not embossed) fluctuated around a constant value (**Figure 3.2 b** red indicators). In particular, the variance of the measured moduli of the nuclear region of cells on control samples was higher with respect to the variance to the modulus measured on cells on patterned substrates. Therefore, although the superposition of a pattern does not alter the stiffness of the nuclear region, the confinement of FAs on the topographic relieves exerts a stabilizing effect on the cytoskeletal structures. Cell's elasticity, at least of the nuclear region, is mostly affected by the macroscopic, rectangular shape, rather than by the presence of an underlying nanotopography.

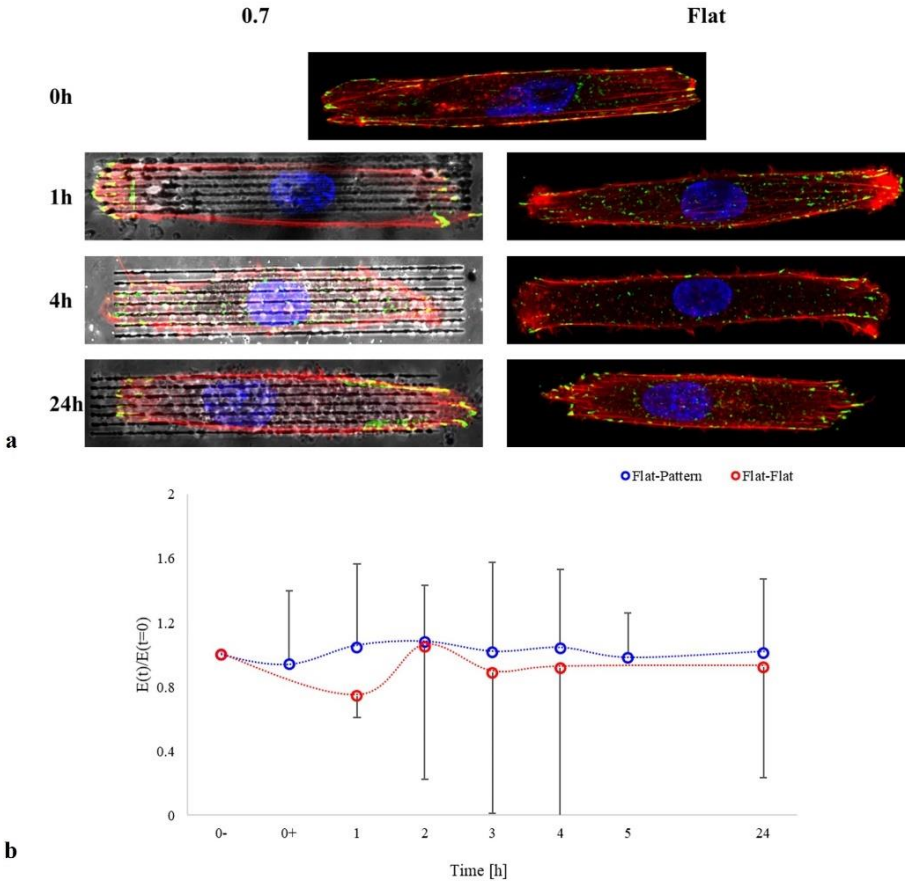

Figure 3.2: (a) *Confocal images of fixed rectangular hTERT on flat surface and 1, 4 and 24 hours after the linear pattern inscription. Cell cytoskeleton is stained with Phalloidin (red), FAs are immunostained for vinculin (green), and nuclei are stained with DAPI (blue).* ***(b)*** *Plots of the Young's moduli variation over time of rectangular cells cultured on flat surfaces and subsequently in contact with nanotopographic pattern (blue indicators) and cells cultured on flat surfaces without undergoing further topographical changes over time. Using "t= 0-" we indicate cells on flat pDR1m substrate, whereas with "t=0+" we indicate the immediate moment of cell-topography contact.*

In contrast, cells confined in circular shapes, in the absence of topography, were characterised by randomly oriented actin fibres (**Figure 3.3 a**). Their Young's moduli evaluated in the nuclear region was constant values over time (**Figure 3.3 b** red indicators). As soon as the linear nanopattern was applied, there was a rapid drop in mechanical properties (**Figure 3.3 b** blue indicators). We associate this behaviour with the redistribution of FAs and the reassembly of the cytoskeleton. In fact, in agreement with the results presented in the previous chapter, the presence of the nanopattern implied a greater orientation of the basal fibres even in the case of cells with isotropic shapes compared to flat surfaces. For this reason, stress fibres re-orientation along the underlying pattern direction, the values of the elastic moduli increased, remaining mostly constant in the following hours but still lower than those measured over time in the absence of the topography. This is probably because when shape confinement affects the FA confinement, the mechanical stability of cells is disrupted by the presence of the topographic nanograting that reduces the space available for FA formation and growth.

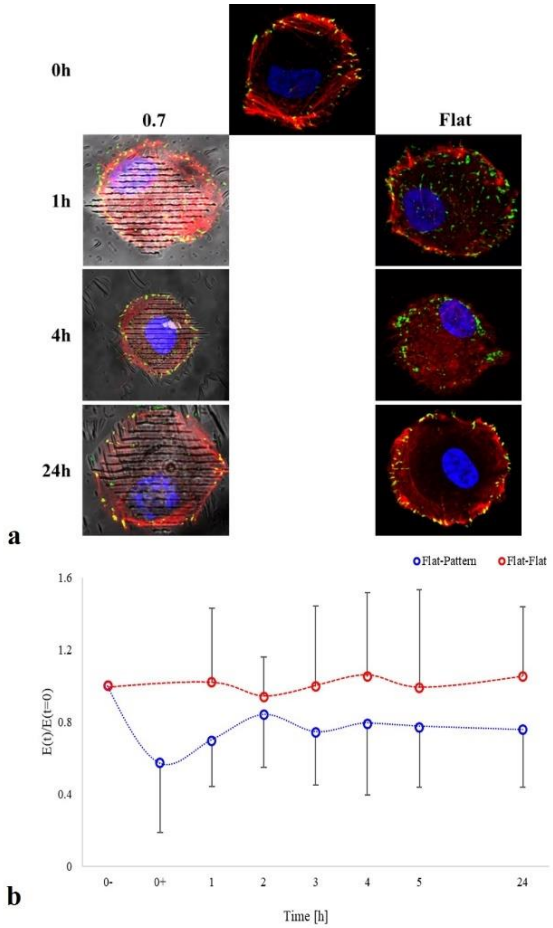

***Figure 3.3**: **(a)** Confocal images of fixed circular hTERT on flat surface and 1, 4 and 24 hours after the linear pattern inscription. Cell cytoskeleton is stained with Phalloidin (red), FAs are immunostained for vinculin (green), and nuclei are stained with DAPI (blue). **(b)** Plots of the Young's moduli variation over time of circular cells cultured on flat surfaces and subsequently in contact with nanotopographic pattern (blue indicators) and cells cultured on flat surfaces without undergoing further topographical changes over time. Using "t= 0-" we indicate cells on flat pDR1m substrate, whereas with "t=0+" we indicate the immediate moment of cell-topography contact.*

Finally, comparing the response to nanotopography of both cell shapes considered (**Figure 3.4**), our experimental observations show a lower cytoskeletal stiffness over time for circular cells than for rectangular ones. This was mainly due to the circumstance that the actin filaments in the geometry of the circular substrate were initially organised as networks of short filaments and random structures and subsequently subjected to a drastic reassembly (lower cytoskeletal stiffness). In contrast, the cells on the elongated substrate experienced increased cytoskeletal tension due to the reinforcement of elongated stress fibres, already oriented before the application of nanotopography, which imposed significant vertical and lateral compressive forces on the nucleus.

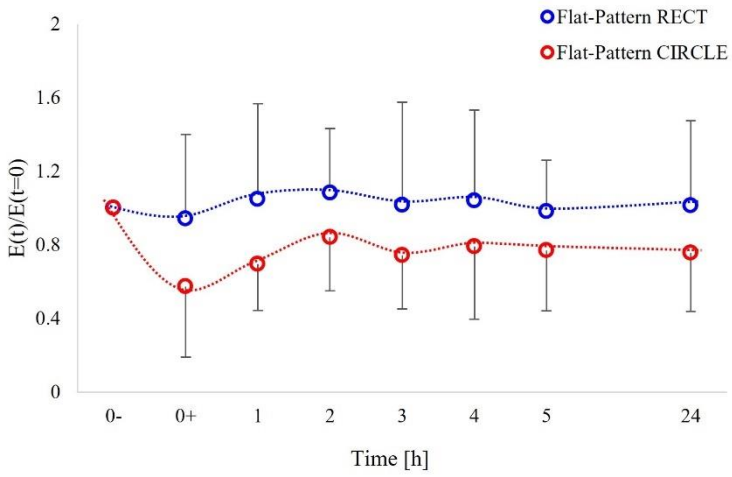

Figure 3.4: *Plots of the Young's moduli variation over time of circular cells cultured on flat surfaces and subsequently in contact with nanotopographic pattern (blue indicators) and cells cultured on flat surfaces without undergoing further topographical changes over time. Using "t= 0-" we indicate cells on flat pDR1m substrate, whereas with "t=0+" we indicate the immediate moment of cell-topography contact.*

Interestingly, this result agrees with what has been observed in the static case in which we observed that SCs cultured on both flat and nanopatterned rectangular surfaces possessed higher mechanical properties than those cultured on isotropic ones.

3.2.3 Focal Adhesion Remodelling

Focal Adhesion (FA) distribution and assembly over time play a fundamental role in the regulation of cell fate[16]. FAs could tune the cytoskeleton-generated forces employed by the cell at the interface and alter the cell contractility that in turn could deform the nucleus and impact the regulation of cell fate through the cytoskeleton-nuclear axis[17]. Topographic patterns of nanometric size display conducive zones for FAs formation and growth juxtaposed to non-conducive ones. The nanopatterning techniques allow achieving a tighter control on FAs shape and positioning. In this respect, combining micro-and nanopatterning techniques we achieved adequate confinement of the cell in rectangular and circular shapes to control FAs dynamics, thus the cytoskeleton arrangement and mechanical identity of the cells. Interestingly, after quantification of vinculin areas, we found that a considerable number of FAs (**Figure 3.5 a**) were located at the periphery cell in rectangular cells seeded on flat substrates and co-localized with the pattern ridges on the linearly patterned substrate (mean value 28°) (**Figure 3.5 b**). This alignment was constant for up to 4 hours after nanopattern inscription (**Figure 3.5 c**). Furthermore, a smaller number of mature vinculin patches that

were more aligned in the direction of the pattern were observed 24 hours after pattern inscription (mean value 21°). This behaviour is particularly evident in **Figure 3.5 d** in which a higher percentage of FAs with an angle between 0° and 15° are observed 24 hours after the pattern inscription compared to the previous hours and those of cells cultured on flat surfaces and more than 75% of the FAs were oriented within 30° from the pattern direction.

Additionally, the mature FAs of the rectangular cells maintained a constant area and length over time regardless of the underlying nanopattern inscription (**Figure 3.5 e, g**). Indeed, FAs on linear patterns showed length (2.3 ± 0.2 μm) and area (1.7 ± 0.1 μm^2) comparable to those measured on the flat substrate (length = 2.5 μm ± 0.3, area = 1.9 ± 0.1 μm^2), which displayed broadly distributed FAs. However, after the patter inscription we observed a general increase of the fraction of the longer FAs, passing from a 3% of FAs longer than 5 μm at 1 hour to 10.4% after 24 hours. Similar reasonings could be made on the evolution of the fraction of FAs with larger areas (**Figure 3.5 f, h**).

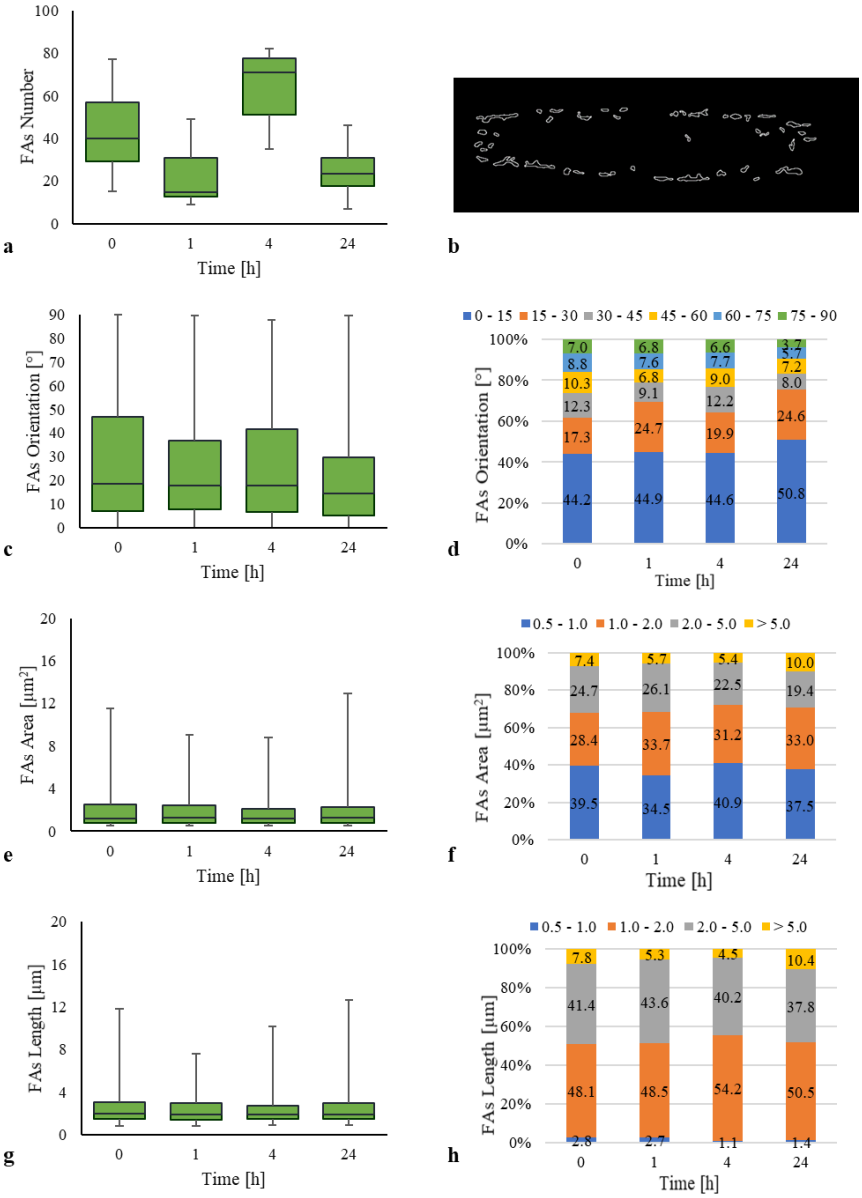

Figure 3.5: (a) *Box and whisker of the FAs number.* ***(b)*** *Positioning of vinculin-containing FAs in rectangular shape cells. Focal adhesions are immunostained for vinculin, the black and white image highlights the FAs contours. On the left box and whisker of the* ***(c)*** *FAs orientation,* ***(e)*** *FAs area, and* ***(g)*** *FAs length in time evolution. On the right, the time evolution of* ***(d)*** *FAs orientation,* ***(f)*** *FAs area, and* ***(h)*** *FAs length expressed as a percentage. t= 0 indicates rectangular cells on flat pDR1m substrate, t= 1, 4 and 24 h indicate rectangular cells on nanopatterned pDR1m substrate respectively 1, 4 and 24 hours after pattern inscription.*

About the circular cells on flat substrates, it was interesting to note that a considerable number of FAs (**Figure 3.6 a**) were positioned along the circumference of the cells, without following a predefined orientation (angle of approximately 45°) (**Figure 3.6 b**). This random orientation of the FAs was kept constant until 4 hours after the sub-inscription of a nanopattern consisting of linear parallel ridges that entirely covered the area of the circular adhesive island (**Figure 3.6 c**). After 24 hours from the pattern inscription, the FAs showed a greater alignment (25° ± 1) along the direction of the underlying pattern that corresponds to a greater number of FAs with an orientation between 0° and 15°, and more

than 50% were oriented within 30° from the pattern direction (**Figure 3.6 d**). Furthermore, FAs of rectangular cells showed a slight increase in size (area and length) over time. In more details, the percentage of FAs having an area greater than 5 μm^2 and a length greater than 5 µm increases with increasing hours on the pattern (**Figure 3.6 e, f, g, h**).

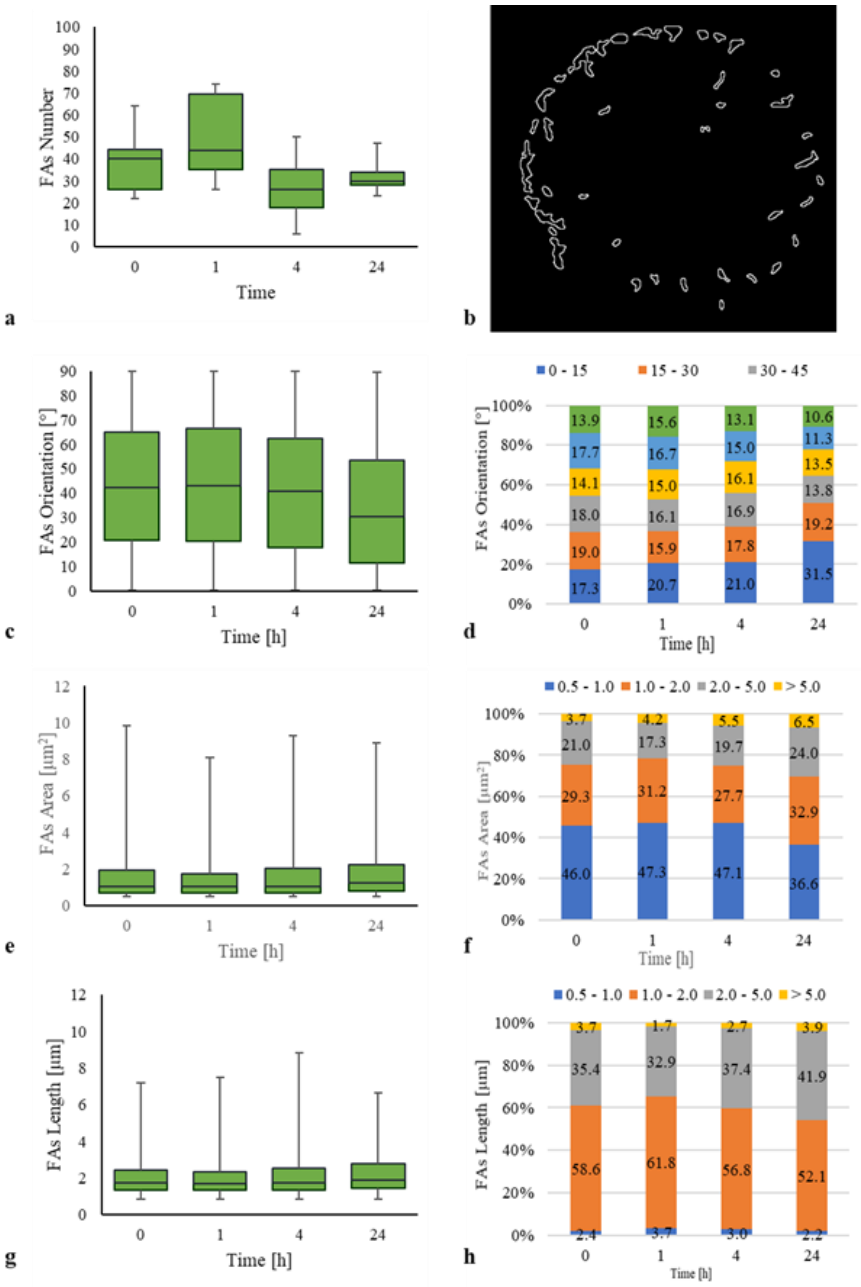

Figure 3.6: ***(a)*** *Box and whisker of the FAs number.* ***(b)*** *Positioning of vinculin-containing FAs in circular shape cells. Focal adhesions are immunostained for vinculin, the black and white image highlights the FAs contours. On the left box and whisker of the* ***(c)*** *FAs orientation,* ***(e)*** *FAs area, and* ***(g)*** *FAs length in time evolution. On the right, the time evolution of* ***(d)*** *FAs orientation,* ***(f)*** *FAs area, and* ***(h)*** *FAs length expressed as a percentage. t= 0 indicates circular cells on flat pDR1m substrate, t= 1, 4 and 24 h indicate circular cells on nanopatterned pDR1m substrate respectively 1, 4 and 24 hours after pattern inscription.*

Our results proved that dynamic surface pattern can control the assembly of FAs consistently with other reports that emphasize the role of FA assembly and orientation on guiding hTERTs through the process of self-organization. The mechanical forces acting on the cell surface are transmitted via FAs to the actin cytoskeleton and in turn to the intracellular regions of the mechanosensor. Focal adhesions, both those of anisotropic cells partially oriented in the direction of the pattern as soon as they are formed and those of isotropic cells randomly arranged, take about 24 hours to fully reorient with respect to the underlying pattern so that perceived mechanical signals are transduced into biochemical signals, generating intracellular structural changes and a functional response (**Figure 3.7**).

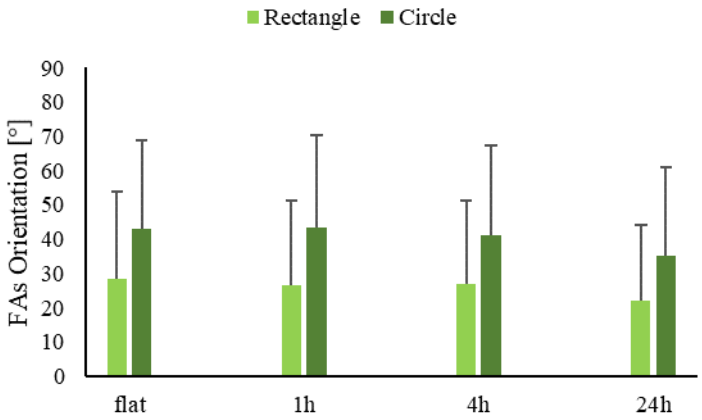

Figure 3.7: *FAs orientation in time evolution. t= 0 indicates cells on flat pDR1m substrate, t= 1, 4 and 24 h indicate cells on nanopatterned pDR1m substrate respectively 1, 4 and 24 hours after pattern inscription.*

3.2.4 Nuclear Deformation

The geometrical constraints cause a different distribution of stress fibres and therefore of the internal cell forces such as to regulate the deformation and morphology of the nuclei. In this regard, we again observed that nuclei of rectangular cells appeared more elongated than nuclei of circular cells both seeded on a flat substrate (t=0). Nucleus morphology of cell cultivated on flat or topographical patterned surfaces was examined using immunofluorescence staining and z-scanning confocal microscopy. Thus, 3D structure analysis was employed to process confocal microscopic images and to generate quantitative information about the morphological feature of hTERT nuclei.

By using this technique, we observed that the nuclei elongation on rectangular patterns increased after the embossing of the nanopattern. In fact, the average value of the nuclear aspect ratio (A/R) was systematically greater than 1 (a value corresponding to perfectly circular shapes) After a temporary increase in the A/R value at 1 hour post inscription, the A/R steadily increased from 2 hours up to 48 hours (**Figure 3.8 a**). The rectangular shape attributed to the cell implied the stretching of the membrane and the assembly of stress fibres which in turn exerted mechanical stresses on the nuclear envelope, thus resulting in the elongated shape of the nucleus. Indeed, the cytoskeleton of the cells on rectangular micropatterns exerted tension along the major axis of the cell, which induced the formation of stress fibres and significant vertical and lateral compression forces on the nucleus that influenced their shape. Therefore, the fabrication of a linear nanopattern extended in the same direction as the major axis of the rectangle further affect the A/R of the nuclei of an already stretched cell. Regarding the nuclear area, **Figure 3.8 b** shows that it was not considerably affected by topographic signals in the case of rectangular cells. This parameter decreased slightly as soon as the cell perceived the topographic signal and then increased non-significantly over the following hours. The effect of the underlying nanopattern was evident in influencing the volume and height of the nucleus over time (**Figure 3.8 c, d**). The nuclei of rectangular cells reacted to the presence of the underlying nanopattern by flattening (decreasing in height) up to two hours after embossing. Probably, this was due to the immediate reassembly of the actin fibres, which in the first two hours, sensing the underlying signals, change conformation by exerting vertical forces on the nucleus. Two hours after the pattern fabrication, the height of the elongated nuclei of rectangular cells began to increase, and this growth was visible up to 48 hours on the linear nanopattern. This trend was similar for the nuclei volume of rectangular cells. In fact, as was also observed in the previous chapter, the increase in cell diffusion, induced by the underlying nanopattern, induced a reduction in the volume of the cells and nucleus. This decrease in nuclei volume could probably be due to the outflow of

water, which leads to a corresponding increase in intracellular molecular crowding[18]. The situation evolved in the opposite direction once the cell diffusion remained unchanged (approximately two hours after the pattern perception).

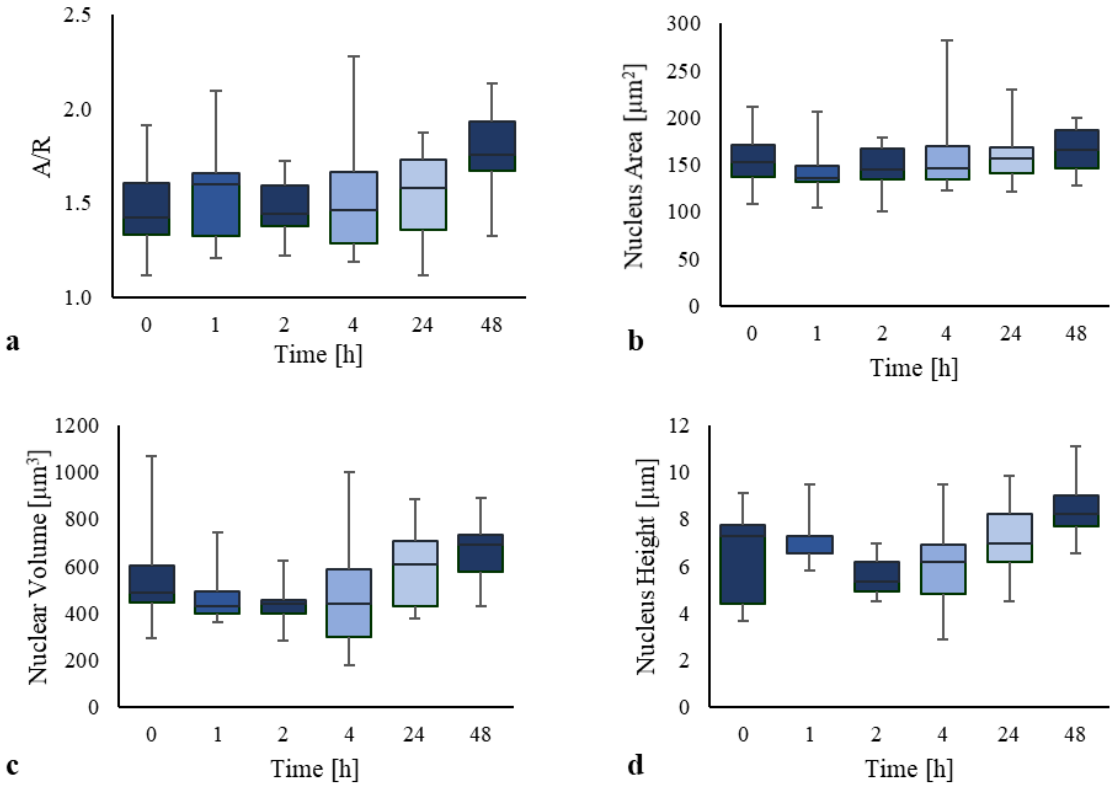

Figure 3.8: *Box and whiskers of* ***(a)*** *the nuclear A/R,* ***(b)*** *nucleus projected area,* ***(c)*** *the nuclear volume and* ***(d)*** *the nuclear height of rectangular shaped cells in time evolution. t= 0 indicates rectangular cells on flat pDR1m substrate, t= 1, 2, 4, 24 and 48 h indicate rectangular cells on nanopatterned pDR1m substrate respectively 1, 2, 4, 24 and 48 hours after the pattern inscription.*

Next, we carried out the same evaluations as for the rectangular cells on circular cells to study their behaviour over time following the nanopattern inscription. We observe different cellular responses from the previous case. Directly 24 hours after the linear nanopattern was produced, the median value of the nuclear A/R was higher than that of the nuclei of the circular cells on flat pdr1m (**Figure 3.9 a**). This mainly indicated that the circular cells were characterised by nuclei that maintained a mostly circular shape even in the short time after the embossing of the topographic pattern. Consistent with the observation made for the FAs, these began to align with the underlying linear nanopattern 24 hours after pattern fabrication, causing a change in the arrangement of the actin fibres, which in turn pressed on the nucleus, giving it a slightly more elongated shape. As far as the nuclear area is concerned, we observed that it was significantly influenced by linear topographic signals in the case

of circular cells (**Figure 3.9 b**). In fact, the median value of nuclear projected area increased one hour after pattern inscription (from 151.494 μm^2 to 223.994 μm^2) and then drastically reduced (110.54 μm^2) after another hour in contact with the nanopattern. From this moment, the area increased until 24 hours after the perception of the pattern, i.e. until the moment when the FAs oriented in the direction of the pattern. A similar trend was observed by analysing the evolution of nuclear volume over time (**Figure 3.9 c**). Taking together this information, we can conclude that the nuclei of circular cells seeded on flat surfaces reduce their size within the first hours of contact with the underlying nanopattern and then gradually increase their size up to 24 hours after the patter inscription. As previously confirmed, the FAs of the circular cells after 24 hours were mature and oriented. This resulted in the formation of aligned stress fibres that exerted a force on the nucleus again resulting in size reduction (t= 48h area= 125.699 μm^2).

Therefore, we can deduce that cytoskeleton assembly and membrane stretching were dominant factors in influencing the volume of the nucleus.

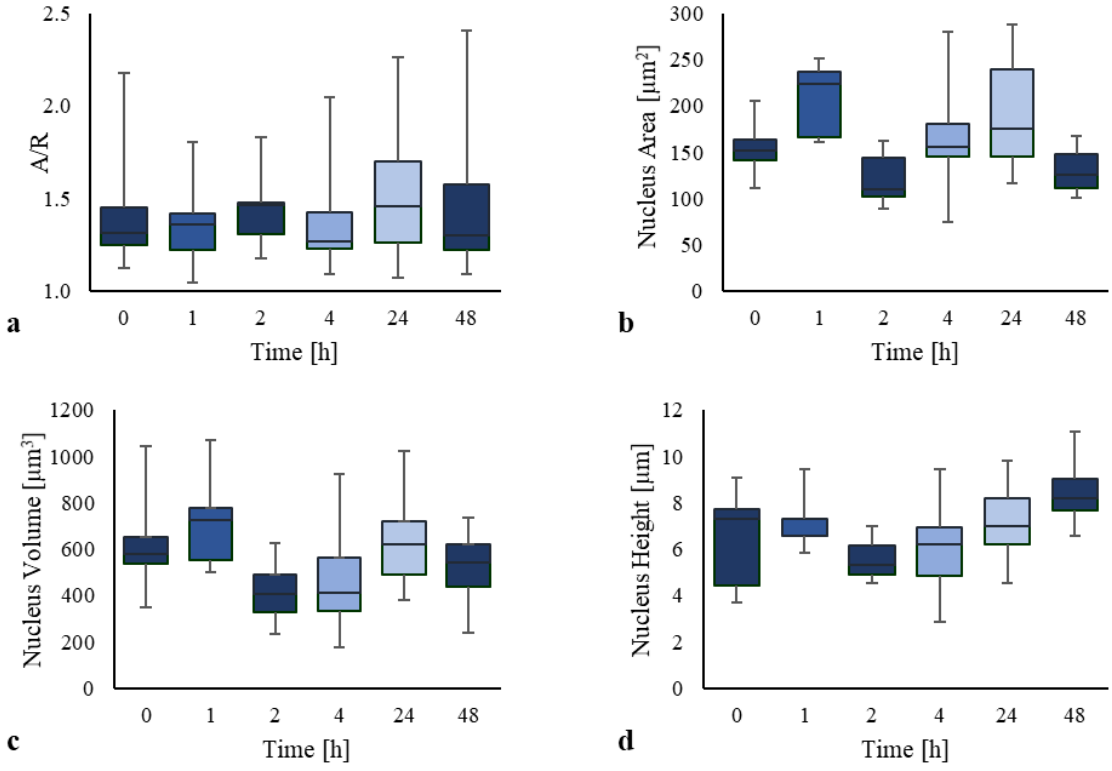

Figure 3.9: *Box and whiskers of* ***(a)*** *the nuclear A/R,* ***(b)*** *nucleus projected area,* ***(c)*** *the nuclear volume and* ***(d)*** *the nuclear height of circular shaped cells in time evolution. t= 0 indicates circular cells on flat pDR1m substrate, t= 1, 2, 4, 24 and 48 h indicate circular cells on nanopatterned pDR1m substrate respectively 1, 2, 4, 24 and 48 hours after the pattern inscription*

3.2.5 Chromatin assembly

In the previous paragraphs, we have shown that the micro- and nano-topographies underlying cells affect cellular behaviour in terms of morphological and mechanical properties. At this stage, we wondered whether and how topographical signals, and eventually the resulting changes in cell structure and contractility, could influence the chromatin condensation states. The dynamics changes of nucleus morphology following pattern inscription are suggestive of a spatial reorganization or possibly of epigenetic modification of the DNA. To assess this, we monitored the changes in the fluorescence intensity of DAPI and of the acetylate groups on K9 of histone 3 and their spatial distribution. DAPI binds strongly to adenine–thymine-rich regions in DNA and therefore marks the region of the nucleus with the higher chromatin density. Therefore, it can be used to measure global or local changes in chromatin condensation. Conversely, acetylation of histones has been correlated with chromatin decondensation[19]. In particular, the acetylation of H3 at lysine 9 has been correlated with active promoters. Therefore, cells with a higher fraction of H3K9Ac are more transcriptionally active[20,21]. For this purpose, combinations of fluorochromes were used to distinguish differently coloured targets (DAPI in blue and H3K9Ac in green) simultaneously in a single cell and high-resolution confocal imaging was used to observe the variation in chromatin configuration (**Figure 3.10 a**).

The nuclei of cells cultivated on rectangular flat pattern exhibited in the 24h - 48h interval slightly but steadily decreased in the observed timeframe ultimately achieving a fluorescent intensity value at 48 h nearly halved with respect to the value measured at 24 h (**Figure 3.10 b** red indicators). In the experiment in which the topography was added to the adhesive micropattern, we observed a more dynamic densification of chromatin (**Figure 3.10 b** blue indicators). After a small decrease of the overall intensity at 2 h after pattern inscription, intensity significantly increased at 4 h post pattern inscription (**Figure 3.10 d**). Then the DAPI intensity decreased, although achieving values higher with respect to what measured in the control sample. Then, owing to the discrete nature of chromatin in which dense domains of heterochromatin are interspersed into an amorphous/open euchromatin, we refined the analysis by evaluating the distribution of fluorescence intensities and size of the brightest domains, corresponding to heterochromatin loci. The distributions of local intensities (**Figure 3.10 f**) show fluctuations of the median values similar to those observed in the case of the global measurements, i.e., a decrease at 2 h post pattern inscription and a rapid increase at 4 h. Besides this, also the shape of the distributions changed dramatically. Right skewed distributions with long tails towards high intensity values are observed prior to pattern inscription (0 h) and 48 h after pattern

inscription. Much narrower and more symmetric distributions are observed at 2 and 24 hours post pattern inscription, with significantly lower intensities with respect to the other time points. Interestingly, at 4 h post pattern inscription, we observed a quasi-uniform distribution extending over broad ranges of fluorescence intensities. The changes in local intensity might arise from either an intrinsic densification of chromatin or to changes in spot size, i.e., the larger the volume the higher the intensity. To verify which one is the underlying nature of the intensity change, we calculated the distributions of the volumes of the fluorescent spots (**Figure 3.10 g**). All the distributions were right-skewed, and the mean value of the volume steadily increased with time. This information, combined with the former on the local intensities, suggests that the change in intensities arise from dynamic densification (change in intensity) and reconfiguration (change in volume) of chromatin domains, rather than a simple increase in domine spot size.

Afterwards, we focused on evaluating the time changes of the fluorescence intensity of the H3K9Ac, as a measure of the quantity and spatial distribution of the decondensed and transcriptionally accessible chromatin. First, we evaluated the global intensity in each nucleus. Cells on control rectangular flat island displayed nuclei with a constant intensity of H3K9Ac in the 48 hours of the experiment (48 - 72 h post seeding) (**Figure 3.10 c** red indicators). A different dynamic of acetylation of H3 was observed when a topographic pattern was overlapped to the adhesive micropattern (**Figure 3.10 c** blue indicators). A marked decrease in acetylation was observed after 2 h post pattern inscription (**Figure 3.10 e**). Then acetylation levels increase back again at 48 hours, achieving a significantly (p<0.07) higher levels with respect to time 0 h, which is also significantly higher (p<0.05) levels with respect to time the control case (point 48 h corresponding to 72 h post seeding). Second, we evaluated the distribution of the fluorescence intensities of the spots positive for H3K9Ac (**Figure 3.10 h**). The trend of the median values of the distributions was qualitatively similar to the trend observed for the average values of the fluorescence intensities evaluated globally. The distributions were generally right skewed, with the only exception of the distributions obtained at 4 and 48 hours post inscription. In the first case, a rather homogeneous distribution was observed that was reminiscent of the distribution of the DAPI stained loci at the same time point. At 48 hours the distribution displayed three distinct peaks, suggesting the existence of a much more heterogeneous assembly of H3K9Ac domains. Altogether these data suggest that the superposition of a topographic pattern onto an adhesive one profoundly affects chromatin configuration and its epigenetic state. We identified 4 h as a characteristic time in which extensive changes in local chromatin density and acetylation occurs.

Finally, the redistribution of gene material and its epigenetic modifications was a phenomenon actually and qualitatively evident. Indeed, clusters of DAPI increased in volume over time, separated from those of H3K9Ac and, at longer times (48 hours post patterning) were mostly located along the circumference of the nuclei (**Figure 3.10 a**).

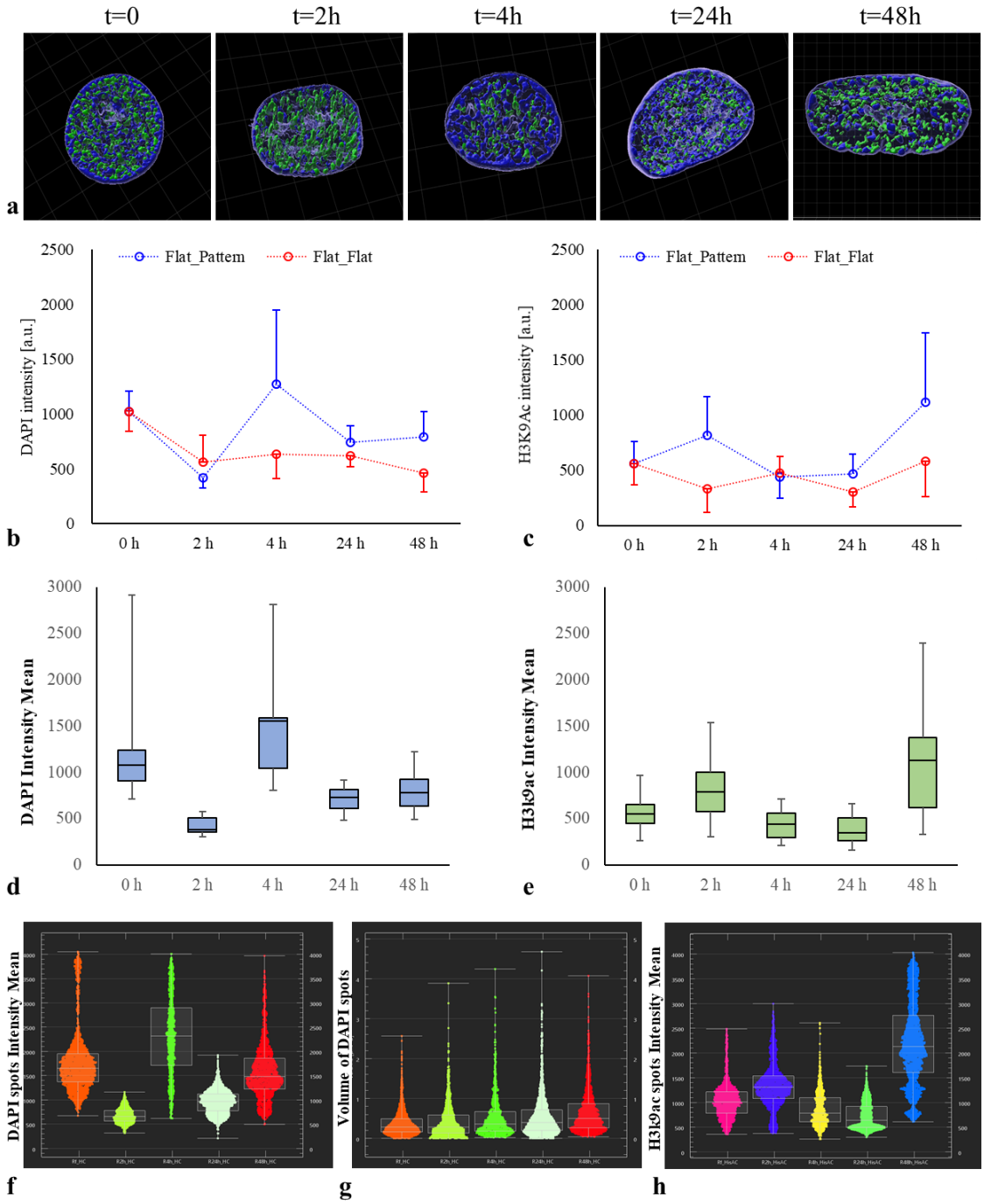

Figure 3.10: ***(a)*** *3D reconstruction of rectangular cell nuclei on flat surface (t=0) and 2, 4, 24 and 48 hours after pattern inscription. Nuclei are immunostained for DAPI (blue) and H3k9Ac (green). Plots of the* ***(b)*** *DAPI global intensity and* ***(c)*** *H3k9Ac global intensity variation over time in nuclei of rectangular cells cultured on flat surfaces (red indicators) and in contact with nanotopographic pattern (blue indicators). Box and whiskers of* ***(d)*** *the DAPI intensity mean,* ***(e)*** *H3k9Ac intensity mean,* ***(f)*** *the intensity mean of DAPI spots,* ***(g)*** *the volume of DAPI spots [μm^3] and* ***(h)*** *intensity mean of H3k9Ac spots in time evolution.*

To find a possible correlation between changes in chromatin condensation or acetylation with nuclear morphology, we performed Spearman correlation tests on the morphometric parameters and fluorescence intensity values of DAPI and H3K9Ac (**Figure 3.11**). We did not find any significant correlation among the various parameters suggesting that the changes in chromatin configuration and acetylation are not related to any morphologic parameter.

Figure 3.11: *Correlation plot between nuclear mechanical, morphological properties and epigenetic modifications in rectangular cells. From left to right (and from top to down)* ***var1)*** *Av Int Mean DAPI overall;* ***var2)*** *Av Int Mean DAPI local intensity;* ***var3)*** *Av Int Mean H3K9Ac overall;* ***var4)*** *Av Int Mean H3K9Ac local intensity;* ***var5)*** *Av Vol Spot DAPI [Aμm^3]* ***var6)*** *Av Nuc Area;* ***var7)*** *Av Nuc Height;* ***var8)*** *Av Nuc A/R;* ***var9)*** *Av Nuc Volume;* ***var10)*** *Av Mod 400.*

Then, we studied how the gene matter of cells cultivated on circular micro islets behaved after the superposing of a topographic pattern over the adhesive one. Also, in the case of circular micropattern, the DAPI stain intensity slightly but steadily decreased in time for the cells cultivated on the control substrates, i.e., no topography inscribed (**Figure 3.12 b** red indicators). Differently from the rectangular micropatterns, the inscription of the topography over the circular pattern did not affect the average DAPI intensities (**Figure 3.12 b** blue indicators, **d**), whose values were very similar to those measured for the control case. The quantification of the distribution of the fluorescence

intensities of the DAPI spots revealed qualitatively similar right skewed distributions, with the only exception of the distribution evaluated at 48h that was bimodal in nature (**Figure 3.12 f**). Furthermore, a clear trend of the volumes of the DAPI spot was not present (**Figure 3.12 g**).

Concerning the H3K9Ac immunofluorescence, we observed marked fluctuation in time (qualitatively visible in **Figure 3.12 a**). However, the average values of intensity never surpassed those measured at the beginning of the observation (24 h of culture) (**Figure 3.12 c**). In the case of the superposition of the topographic pattern, we observed a decrease in fluorescence intensity after 4 h post inscription that then steadily increased up to 48 h (**Figure 3.12 e**). The intensity value attained at this time point was significantly higher with respect to the value of the corresponding time-point in the control case ($p>0.05$). Local analyses on the H3K9Ac intensity distribution highlighted more heterogeneous distributions with respect to those observed in the case of rectangular patterns. In fact, the distribution of intensities was usually characterized by several (local) peaks (**Figure 3.12 h**). It is likely that the superposition of a topographic pattern on a surface inducing a low contractility phenotype, as the circular micropattern, do not significantly alter chromatin condensation or the epigenetic state. We observed an increase of the H3K9Ac levels at longer times (48h time-point) on the topographically patterned circular substrates.

With the data at our disposal, we cannot confirm nor deny that the observed increase of acetylation levels from 4 up to 48 is a genuine event or is part of a sequence of fluctuations. Altogether, we believe that cells on the small and isotropic circular adhesive islets are less prone to respond, in terms of local chromatin densification and epigenetic marks, to overlapping topographic signals.

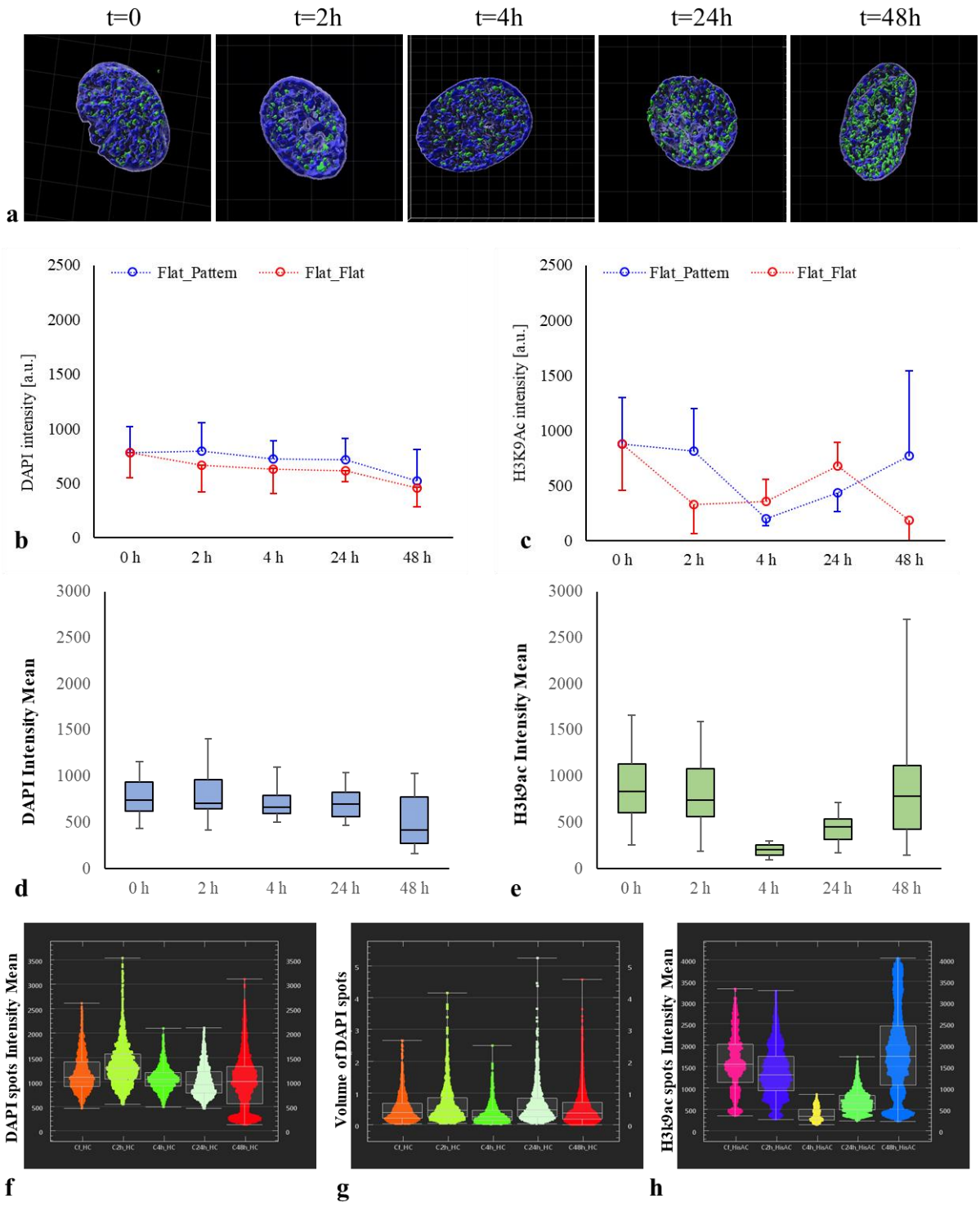

Figure 3.12: ***(a)*** *3D reconstruction of circular cell nuclei on flat surface (t=0) and 2, 4, 24 and 48 hours after pattern inscription. Nuclei are immunostained for DAPI (blue) and H3k9Ac (green). Plots of the* ***(b)*** *DAPI global intensity and* ***(c)*** *H3k9Ac global intensity variation over time in nuclei of circular cells cultured on flat surfaces (red indicators) and in contact with nanotopographic pattern (blue indicators). Box and whiskers of* ***(d)*** *the DAPI intensity mean,* ***(e)*** *H3k9Ac intensity mean,* ***(f)*** *the intensity mean of DAPI spots,* ***(g)*** *the volume of DAPI spots [μm^3] and* ***(h)*** *intensity mean of H3k9Ac spots in time evolution.*

Similarly, to what we observed in the case of the rectangular patterns, we did not find any correlation with nucleus morphometric or mechanical parameters (**Figure 3.13**).

The absence of a specific correlation between chromatin redistribution and the cell's mechanical and morphological properties probably occurs because acetylation is a very complex phenomenon and we have analysed only one type of this, i.e., the acetylation of the 9th lysine residue of the histone H3. However, in order to conduct a more exhaustive study, acetylation at other locations of other histones or other types of genetic modifications would have to be considered, including methylation, phosphorylation, ubiquitination, and glycosylation[21]. In addition, we believe that the complexity of the acetylation process could be also attributed to the request of enzymes capable of translocating from the cytoplasm to the nucleus and triggering biochemical reactions, as well as to the size of the nuclear pores[22], which in turn could influence the rate of nucleocytoplasmic transport[23].

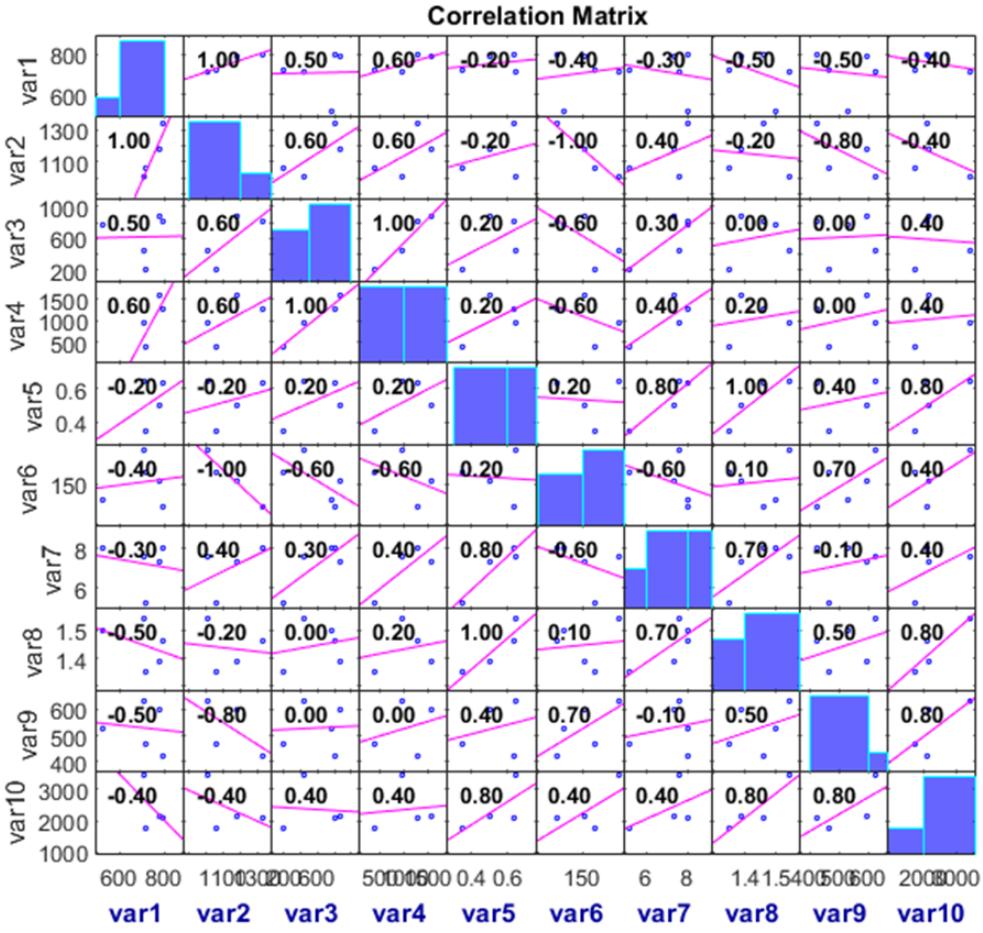

Figure 3.13: *Correlation plot between nuclear mechanical, morphological properties and epigenetic modifications in circular cells. From left to right (and from top to down) var1) Av Int Mean DAPI overall; var2) Av Int Mean DAPI local intensity; var3) Av Int Mean H3K9Ac overall; var4) Av Int Mean H3K9Ac local intensity; var5) Av Vol Spot DAPI [Aμm^3] var6) Av Nuc Area; var7) Av Nuc Height; var8) Av Nuc A/R; var9) Av Nuc Volume; var10) Av Mod 400.*

Ultimately, when comparing hTERTs cultured on micropatterned islands with well-defined cell shapes (round or elongated) without the presence of nanopatterns, we noted that cells in an elongated shape showed significantly lower levels of nuclear H3K9Ac, compared to cells in a round shape (**Figure 3.14 a**) with an equal diffusion area. Conversely, elongated cells had higher values of DAPI spots intensity mean than circular cells (**Figure 3.14 b**). This behaviour confirms the multiple studies known in the literature showing a greater amount of transcriptionally inactive chromatin of elongated cells compared to a greater amount of transcriptionally inactive chromatin characteristic of circular-shaped cells[24].

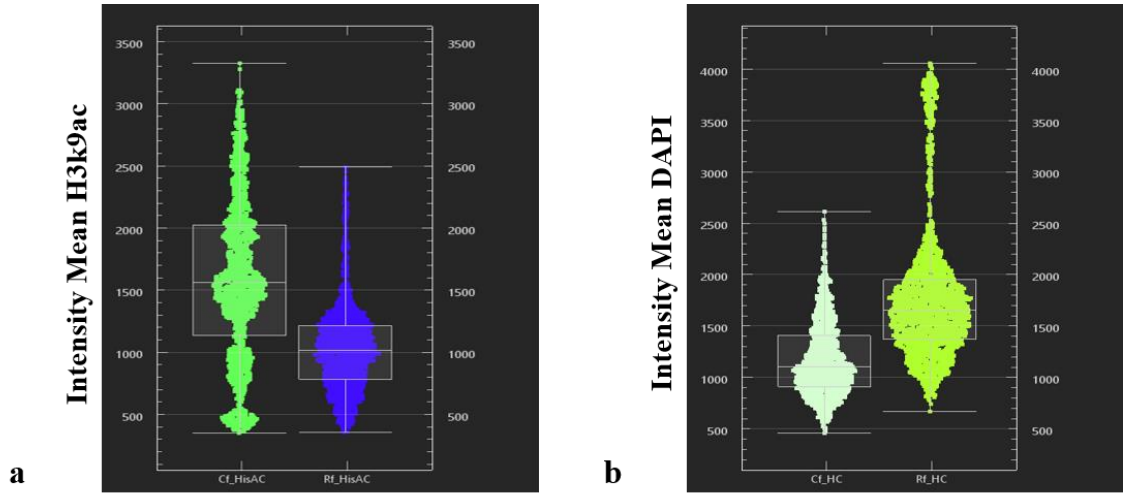

Figure 3.14: *Box and whiskers of* ***(a)*** *the H3k9Ac spots intensity mean* ***(b)*** *DAPI spots intensity mean expressed by the nuclei of circular and rectangular cells both grown on flat substrates.*

In agreement with Li et al., we therefore demonstrated that regardless of the level of original contractility, the level of histone 3 acetylation increased in nuclei in response to nanopattern inscription, but only after 24 - 48h post-patterning (long timescale) after a phase of chromatin redistribution evident at short timescales[25].

In conclusion, the conducted experiments based on the use of dynamic substrates show that cells with originally different mechanical properties (rectangular and circular) exhibit alterations in their adhesive properties due to the superposition of the nanopattern, which can alter not only the mechanical state but also the chromatin redistribution and the epigenetic state.

3.2.6 YAP and lamin A/C expression

Nucleus is far from being a passive structure. Gene matter and the nuclear envelope extensively adapt to external mechanical stimuli. Changes in local chromatin density and acetylation are two rather downstream results of the process of nuclear shape changes and external mechanical actions. Several other markers have been identified in the recent past that provide information on the active mechanosensing mechanisms that ultimately affect nuclear mechanics and gene expression[26,27]. Among these Lamin and YAP (Yes-associated protein) attracted interest as their mechanosensitive nuclear expression and localization correlated with cell differentiation and other cellular functions[28]. In particular, A-type lamins are the family most involved in mechanotransduction events. The nuclear lamina performs different essential functions in the mechanotransduction pathway modulating the nuclear stiffness, governing the chromatin remodelling, and transmitting cytoskeletal forces to the nucleus[29]. Indeed, A-type lamins mutation and distribution have been found to affect the nuclear response, altering several cellular processes such as mitosis, chromatin organisation, DNA replication-transcription, and nuclear structural integrity. In addition, YAP is a transcription factor widely studied because it can respond to mechanical (i.e., the ECM rigidity) and topographical signals (i.e., the micro- or nano-pattern)[30,31]. In particular, YAP is a cofactor that shuttles between the cytoplasm and nucleus where it associates with several promoter-specific transcription factors. Being the expression and localization of Lamins and YAP two important readout of the actual mechanical state of the cells (in general) and the nucleus (in particular) we stained cell cultures (on flat and nanopatterned substrates), at different time points for Lamin A and YAP. We wanted to verify whether Lamins and YAP are sensitive to dynamic changes of the adhesion properties of the substrate and hence changes in the FA and cytoskeleton assemblies.

Regarding the nuclei of rectangular cells, we observed that after pattern inscription a slight decrease in Lamins intensity was observed up to 4 hours (**Figure 3.15 a**). Afterwards, Lamins intensity significantly increased and attained a high level of fluorescence intensity up to 48 hours. Conversely, cells on the control substrates, expressed constant levels of lamins, with some fluctuations at late time-points (**Figure 3.15 b**). However, Lamins intensity on flat substrates was significantly lower, with respect to the nanopatterned samples at 24 h and 48 h time points.

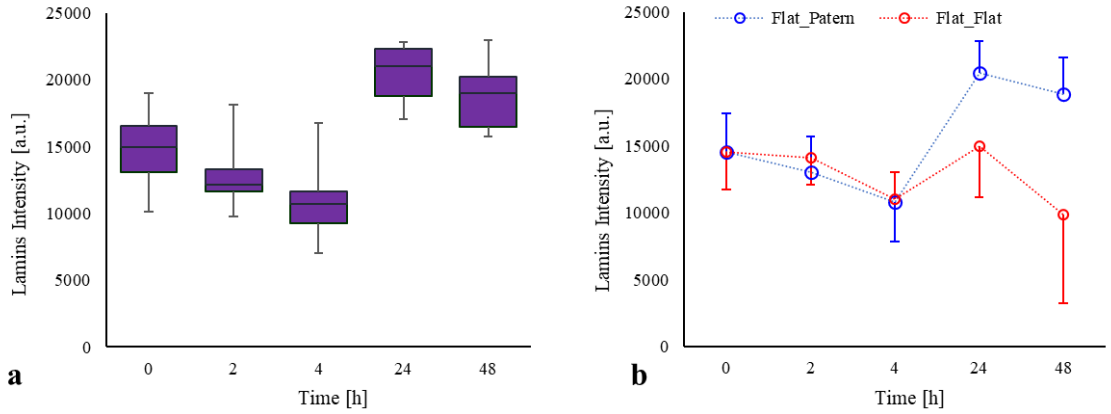

Figure 3.15: (a) *Box and whiskers of the time evolution of lamins A/C protein expression.* ***(b)*** *Plots of the lamins A/C intensity variation over time in nuclei of rectangular cells cultured on flat surfaces (red indicators) and in contact with nanotopographic pattern (blue indicators).*

As far as the nuclear import of YAP, it has been correlated with increased cell contractility or increased mechanical properties of the extracellular environment[32]. In our experimental setup, we wanted to observe whether the nuclear transport of YAP was sensitive to dynamic changes of the adhesive conditions. We found a higher fluorescence density of YAP in the nuclear region with respect to the cytoplasmic fluorescence density on flat substrates (t=0) (**Figure 3.16 a**). After pattern inscription, we observed a gradual decrease in YAP fluorescence density in both cellular compartments (2h post patterning). However, at longer time intervals (above 24 h), YAP was intensely localized in the nucleus, whereas it remained at low values of fluorescence density in the cytoplasm. Cells on the control substrates behaved in a similar manner at short times, with a gradual reduction of YAP fluorescence in either the cytoplasm or the nucleus (**Figure 3.16 b** on the bottom). However, fluorescence tended to remain at low levels at later time points (24 h control in the graph corresponding to 48 h post seeding and 48 h corresponding to 72 h post seeding). We then refined the analysis by evaluating relative differences of fluorescence density with respect to time zero. As evident from **Figure 3.16 c** the relative behaviour of YAP fluorescence in the nanopatterned sample and control are similar up to 4 hours. Then cells on nanopatterned samples expressed higher levels of nuclear YAP with respect to the control case.

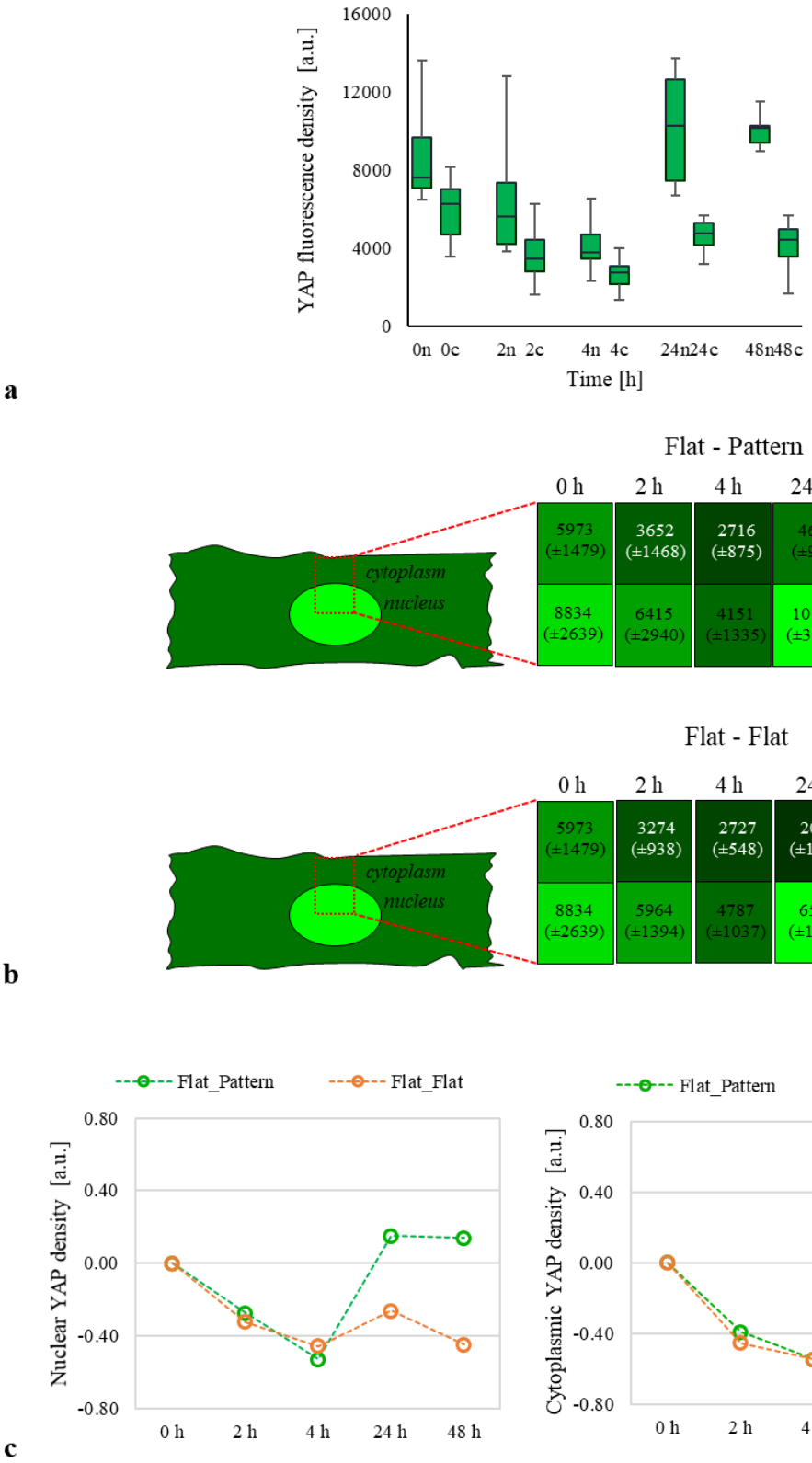

Figure 3.16: ***(a)*** *Box and whiskers of the time evolution of fluorescence density of YAP.* ***(b)*** *Graphical representation of the time evolution of nuclear and cytoplasmic YAP density values in the nuclei of rectangular cells cultured on nanopatterned substrate (top) and on flat surfaces (bottom) expressed in terms of green intensity.* ***(c)*** *Plots of Nuclear YAP density (on the left) and cytoplasmic YAP density (on the right) variation over time in nuclei of rectangular cells cultured on flat surfaces (orange indicators) and in contact with nanotopographic pattern (green indicators).*

In order to find a possible correlation between changes in nuclear structure with nuclear morphology and mechanic, we also in this case, performed Spearman correlation tests (**Figure 3.17**). We found a significant correlation between the intensity level of lamins and the nuclear fluorescence density of YAP. This observation is consistent with literature reports indicating an increase of nuclear Lamin expression and increased YAP nuclear transport in more contractile cells, i.e. cells on stiff substrates. Coherently with these observations, we found a very high correlation coefficient (0.80 although non-significant) between the Lamin fluorescence intensity and the elastic modulus of the nuclear region.

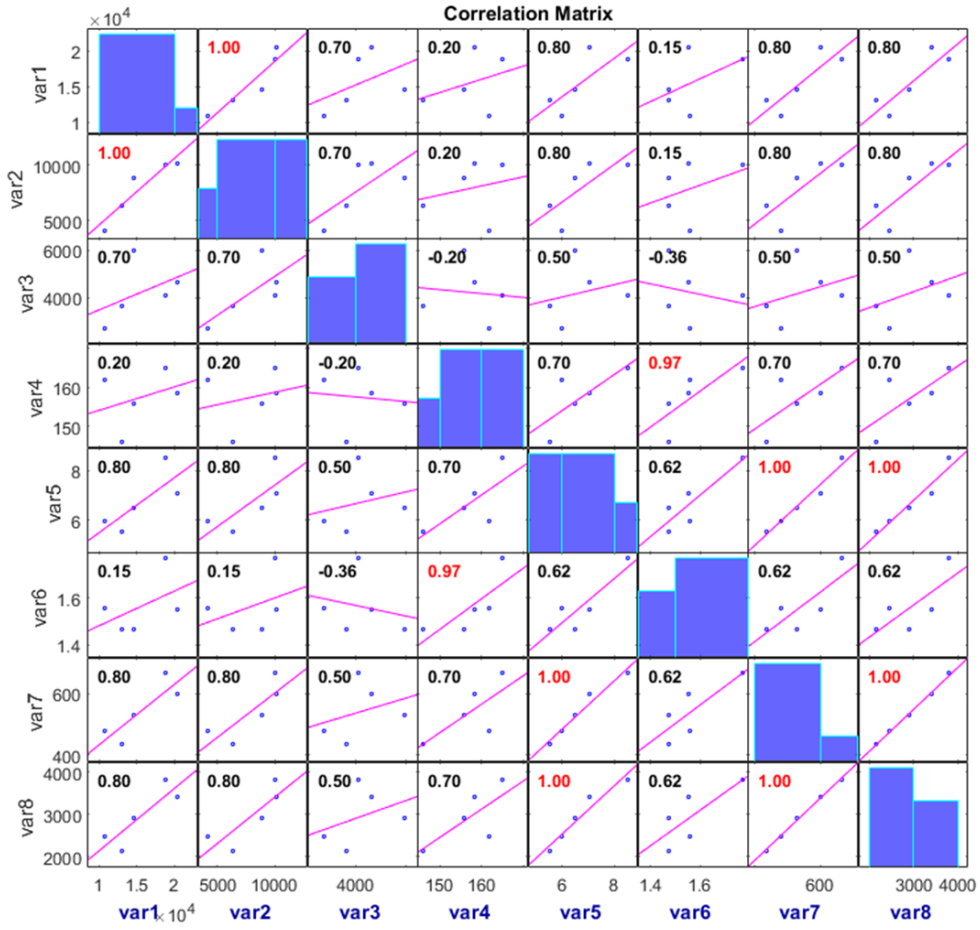

Figure 3.17: *Correlation plot between nuclear mechanical, morphological properties and epigenetic modifications in rectangular cells. From left to right (and from top to down)* ***var1)*** *Av Lamin;* ***var2)*** *Av YAP Nuclear;* ***var3)*** *Av YAP Cytoplasmatic;* ***var4)*** *Av Nuc Area;* ***var5)*** *Av Nuc Height;* ***var6)*** *Av Nuc A/R;* ***var7)*** *Av Nuc Volume;* ***var8)*** *Av Mod 400.*

Subsequently, we passed to analyse lamins intensity on the isotropic circular micropattern, which produces a less contractile phenotype as opposed to the rectangular micropattern. Also in this case, we observed an increase in Lamin intensity after the nanopattern superposition, but later point (48 h)

(**Figure 3.18 a**). Cells on control surfaces (no nanopattern inscription) express constant values of lamins, at least in the time frame we observed (24 – 72 h post seeding) (**Figure 3.18 b**).

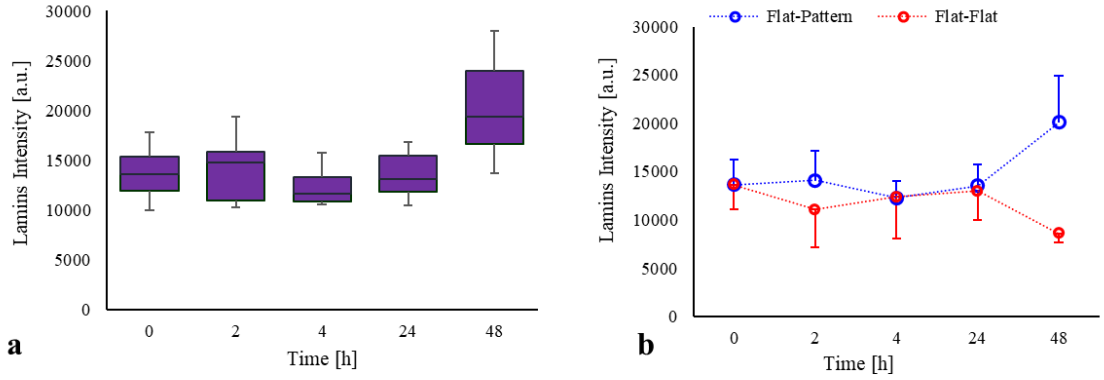

Figure 3.18: (a) *Box and whiskers of the time evolution of lamins A/C protein expression.* ***(b)*** *Plots of the lamins A/C intensity variation over time in nuclei of circular cells cultured on flat surfaces (red indicators) and in contact with nanotopographic pattern (blue indicators).*

Finally, we analysed YAP fluorescence density and its localization in the cells on circular micropatterns. Similarly, to what observed in the case of rectangular micropatterns, we found higher levels of nuclear YAP with respect to cytoplasmic YAP (**Figure 3.19 a**). The superposition of a topographic pattern did not affect the distribution significantly, for short time intervals (up to 4 hours). However, at longer time intervals we observed a marked increase in nuclear YAP. In comparison, cells on control substrates (no pattern inscription) exhibited relatively constant values of fluorescence density all over the time frame of the analysis (**Figure 3.19 b**). Also in this case, we refined the analysis by evaluating relative differences of fluorescence density with respect to time zero. **Figure 3.19 c** shows that the contribution of the nanotopography was evident 24 hours after pattern inscription when the amount of YAP increased significantly and particularly its cytoplasmic localization compared to the control substrates. Hence, despite the lower contractile phenotype of cells on a circular adhesive area, the superposition of a topography over the adhesive signal does affect Lamin expression and YAP transport at longer times.

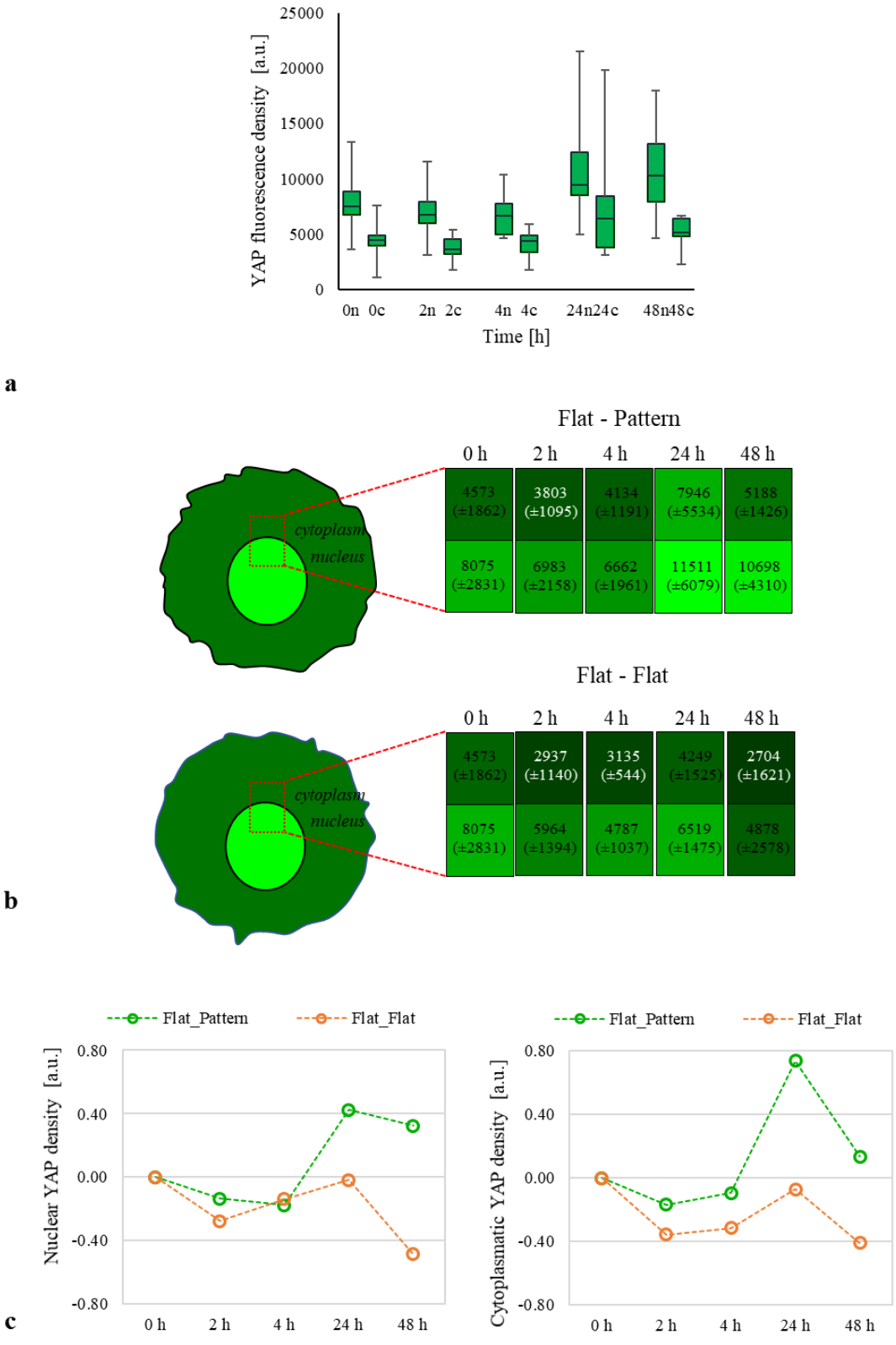

Figure 3.19: ***(a)*** *Box and whiskers of the time evolution of fluorescence density of YAP.* ***(b)*** *Graphical representation of the time evolution of nuclear and cytoplasmic YAP density values in the nuclei of circular cells cultured on nanopatterned substrate (top) and on flat surfaces (bottom) expressed in terms of green intensity.* ***(c)*** *Plots of Nuclear YAP density (on the left) and cytoplasmic YAP density (on the right) variation over time in nuclei of circular cells cultured on flat surfaces (orange indicators) and in contact with nanotopographic pattern (green indicators).*

For circular cells we did not find a correlation between the intensity level of lamins and the nuclear fluorescence density of YAP (**Figure 3.20**). The latter, however, has a high correlation with the cell stiffness at the nuclear region. It is likely that the expression of lamins in cells on isotropic shapes, which generally induce a less contractile phenotype, is less sensitive to changes in adhesion due to the surfacing of the topographic patterns.

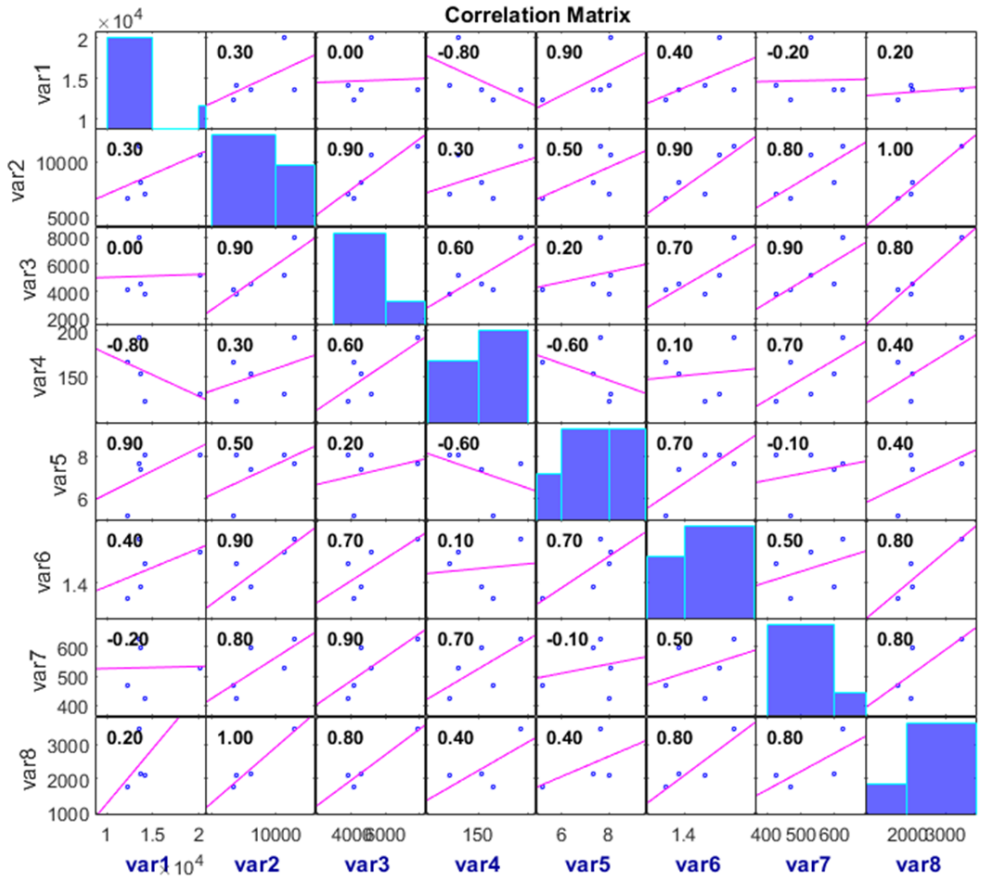

Figure 3.20: *Correlation plot between nuclear mechanical, morphological properties and epigenetic modifications in circular cells. From left to right (and from top to down)* ***var1)*** *Av Lamin;* ***var****2)* *Av YAP Nuclear;* ***var****3)* *Av YAP Cytoplasmatic;* ***var4)*** *Av Nuc Area;* ***var****5)* *Av Nuc Height;* ***var****6)* *Av Nuc A/R;* ***var****7)* *Av Nuc Volume;* ***var****8)* *Av Mod 400.*

In agreement with several works in the literature, including those carried out by Swift et al.[33] and Gonzalez-Cruz et al.[34], we also found a positive correlation between the expression of laminin protein and average cell moduli (in the case of rectangular cells) and between the density of nuclear YAP and cellular mechanical properties (in the case of both cellular shapes). However, these events did not appear immediately as the cells required time (24 - 48h) to perceive the changes in the microenvironment. Although there is no statistical significance (coefficient values 0.80 in **Figure 3.17**) since we have considered few time points, we cannot disregard such a high correlation value

and agree with the literature in which it has been repeatedly demonstrated that increased expression of lamins and nuclear YAP transport occurs when the cell assumes a more contractile phenotype[35].
In conclusion, putting together our results, we have observed that exerting relatively fine-tuned modifications of the adhesive conditions results in significant effects not only in terms of cell morphology and mechanics but also in terms of gene matter (DAPI and H3K9Ac), structural features of the nucleus (lamins) and transport mechanisms (YAP).

3.3 Conclusion

In this chapter, we have shown how cells sense mechanical signals from their microenvironment and transduce them to the nucleus to regulate the mechanical and morphological properties as well as the gene expression programs. In particular, we observed how cell geometric constraints and topographical patterns of nanometric scale affect over time the cell mechanical properties and subsequently induce cytoskeleton-mediated alterations in the nuclear properties. Moreover, the changes in the physical properties of the nucleus have been observed to be correlated with alterations in nuclear architecture and transcriptional factors expression[36].

We showed that cell geometry controls these nuclear properties by regulating the local tensile stresses generated from mature focal adhesions. In more detail, we observed how the physical properties of the microenvironment, in particular nanotopography, impact the properties of the cytoskeleton and nucleus by regulating the dynamic reciprocities between the tension-dependent formation of focal adhesions, the polymerisation of actin filaments, the stiffening of the nuclear envelope lamina network and the nucleocytoplasmic displacement of epigenetic factors. By summarising the analyses carried out in this chapter, we can conclude that biophysical cues in the form of parallel nano-grooves on the surface of cell-adhesive substrates (circular or rectangular adhesion area) affect the nuclear mechanical and structural properties, the chromatin condensation, and the transcriptional factors translocation in nuclei. In the next future, these could therefore be likely to improve reprogramming efficiency and eventually replace the effects of small-molecule epigenetic modifiers. Moreover, this information may be crucial in the biomedical field, offering new ways to maximise the potential of stem cell technologies, mitigate the pathophysiological response in injured and diseased states, and greatly improve the design of next-generation biomaterials. For this purpose, in addition to histone acetylation, other histone modifications such as phosphorylation, methylation and ribosylation, could also be regulated by biophysical factors and could be determined in future studies. Clarifying anisotropic mechanosensing and chromatin remodelling of cells will not only advance our understanding of the roles of mechanical deformation in tissue remodelling, but also provide a rational basis for designing tissue engineering bioreactors that can utilise appropriate mechanical stimulation.

3.4 Experimental Section

3.4.1 General Materials

Trypsin and paraformaldehyde and rabbit YAP1 polyclonal antibody were provided from Thermo Fisher Scientific. Poly-Disperse Red 1-methacrylate (pDR1m), Chloroform, TRITC phalloidin, Triton X-100, bovine serum albumin (BSA), fibronectin solution and anti-paxillin monoclonal antibody were provided by Sigma-Aldrich.

Alexa Fluor 488 Phalloidin, Alexa Fluor 546 conjugated goat anti-mouse antibody, Rabbit pAb to Histone H3 (acetyl K9) - ChIP Grade (Cat. No. ab4441) and DAPI were purchased from Abcam. ASC52telo, hTERT immortalized adipose derived Mesenchymal stem cells were purchased from ATCC. Anti-Lamin A/C mouse Antibody was purchased from Santa Cruz (Cat. No. 376248).

3.4.2 Dynamic Sample Preparation

10 μm diameter cover glasses are washed three times in acetone and sonicated for 15 minutes, then dried on a heated plate. Spin coating technique was used to produce thin films of pDR1m on cover glasses. pDR1m was initially dried overnight and then dissolved in chloroform at a 3% w/v concentration, sonicated and heated to 37°. 15 μl of this solution was used for each cover glass. The solution was spun over the cover glass using a Laurell spin coater (Laurell Technologies Co.) at 5000 rpm. The film thickness was assessed with a Dektak 150 Veeco profilometer. Only those samples display a uniform coating thickness of (approximately) 300 nm were used for the experimentations and analyses.

3.4.3 Micropatterning protocol

pDR1m substrates are activated by exposure to deep UV Printer (4D cell, Montreuil, France) for 15 min. Then the samples are incubated for 1 h with 0.1 mg ml^{-1} poly-L-lysine-g-poly(ethyleneglycol) (PLL(20)-g[3.5]-PEG(2); SuSoS Surface Technology, Dubendorf, Switzerland) at room temperature (40 μL for each sample). After washing with distilled water, the treated surface was illuminated with deep UV light through a photomask.

The 4Dcell photomask is a quartz mask with a chromium designed coating for the aim of the micropatterning experiment. It is used for the printing of the micropatterns on slides, with deep UV. Our mask is characterized by two geometric figures having the same surface area (1300μm^2): circle and rectangle. The 4Dcell quartz mask is washed with absolute ethanol and it is illuminated for 10 min using the deep UV Printer, with its brown side facing the lamp. This makes the brown side of the mask hydrophilic. 2.5μL of millipore H_2O are added onto the brown side of the 4Dcell quartz mask and the PEGylated side of the sample is gently dropped onto the mask. Using the deep UV Printer, the 4Dcell mask is illuminated for 8 min with the silver side facing the lamp. 5 mL of distilled water are added on the mask to help detach the slides from it. The activated side is than incubated 1h at room temperature with 50 μL of fibronectin (final concentration of 50 μg ml^{-1}) and after it is rinsed with PBS.

3.4.4 Plating of the cells

hTERT are cultured in Mesenchymal Stem Cell Basal Medium (ATCC PCS-500-030). To make the complete growth medium, Mesenchymal Stem Cell Growth Kit (ATCC PCS-500-040) for Adipose and Umbilical-derived MSCs – Low Serum Components and G418 is added to the base medium. Cells are detached from the culture plate and centrifuged to remove traces of trypsin; the enzyme used to detach the cells. They are then resuspended in the culture medium and 25.000 cells are seeded per sample. Cells were cultured at 37 °C in a humidified atmosphere of 95% air and 5% CO_2. Cells should be spread on the patterns 2h after plating.

3.4.5 Dynamic Topographic Pattern Inscription

hTERT were cultured on pDR1m coated glass slides previously micropatterned (method described above) for 24 hours. Afterwards, real-time pattern inscription on cell-populated samples was performed by using a Axio Observer Z1 microscope (Zeiss, Germany). The isomerization of the azopolymer and its consequent mass transport were activated using an Argon laser at 488 nm and 1.3 mW of intensity with a 10x (N.A. 1.4) objective lens. Patterns were embossed on the pDR1m substrates by illuminating with the laser light in specifically drawn regions-of-interest (ROIs). In more details, around 0.7 μm wide parallel ROI with spacing of 0.7 μm were used. The exposure time was 60 seconds.

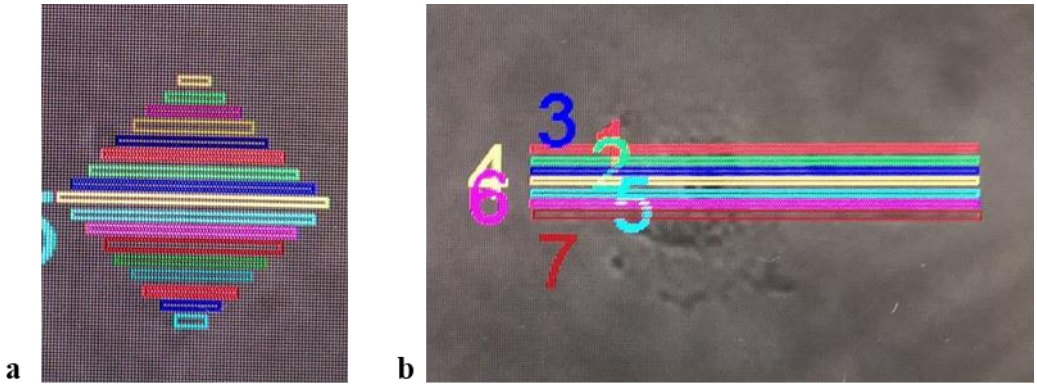

Figure 3.21: *Parallel ROI used to fabricate linear nanopattern on* ***(a****) circular and* ***(b)*** *rectangular cells.*

3.4.6 AFM for Sample Surface Characterization

An atomic force microscope JPK NanoWizard II (JPK Instruments, Germany) was used to acquire images of pDR1m samples. An Axio Observer Z1 microscope (Zeiss, Germany) was combined to the AFM to control tips and sample position. Silicon Nitride probes (MLCT, Bruker, USA), with a spring constant of 0.01 N/m, were used in contact mode, in air, at room temperature. Raw images were corrected by the JPK data processing software using a standard procedure (flatten, planefit and artifact lines caused by the tip attachment and removal). The scale indicating the sample height or deflection was adjusted to limit the gap between high and low regions. Using this software, we measured the cross sections through the images, and we obtained the samples 3D views.

3.4.7 Fixed-cell Staining

Cells were fixed at different time-points: flat and 1 h, 4 h, 24 h, 48 h after pattern inscription. Cell fixation was performed by incubating cells in a 4% paraformaldehyde solution for 15 minutes. Then, cells were permeabilized with 0.1% Triton X-100 in PBS for 15 min. Samples were blocked in 3% bovine serum albumin in PBS (Sigma-Aldrich) for 1 h to avoid non-specific binding. FAs were labelled by incubating samples with an anti-paxillin monoclonal antibody (dilution 1: 400) for 1 h at room temperature or histones were marked by incubating samples with an anti-histone H3(ACK9) in monoclonal antibody (dilution 1: 400) for 1.30 h at room temperature. After incubation, substrates were washed three times with Triton-PBS (3 min per wash) and incubated with Alexa Fluor 546

conjugated goat anti-mouse antibody (dilution 1: 1000) for 1 h at room temperature. Actin filaments were stained by incubating samples with Alexa Fluor 488 phalloidin (dilution 1: 200) for 1 h at room temperature. Finally, cells were incubated for 15 min at room temperature in DAPI solution (dilution 1:1000) to stain nuclei. Samples were thoroughly rinsed in PBS and placed upside down on the glass. Fluorescent images of FAs and actin bundles were collected with an Axio Observer Z1 confocal microscope (Zeiss, Germany). Samples were excited at 488 nm (phalloidin), 543 nm (paxillin) and 405 (DAPI), and the emissions were collected in the 500-530 nm, 560-610 nm and 420-480 nm ranges, respectively.

3.4.8 YAP and Lamins immunostaining

Cells were fixed at different time-points: flat and 1 h, 4 h, 24 h, 48 h after pattern inscription. Cell fixation was performed by incubating cells in a 4% paraformaldehyde solution for 15 minutes. Then, cells were permeabilized with 0.1% Triton X-100 in PBS (PBS-T) for 15 min. Samples were blocked in 3% bovine serum albumin in PBS for 1 h to avoid non-specific binding. Anti-YAP (1:250, rabbit) primary antibodies in BSA were added to the samples and incubated overnight at 4 °C. Subsequently, lamins were labelled by incubating samples with an anti-LMNA (1: 500, mouse) for 1 h at room temperature. Primary antibodies were removed by rinsing in PBS-T three times for 3 min. Samples were then incubated at room temperature with secondary antibodies (1:1000, goat anti-rabbit AlexaFluor 546, 1:300 goat antimouse Alexa-Fluor 647), and Alexa Fluor 488 Phalloidin (1:300) for 1 h at room temperature. Finally, cells were incubated for 15 min at room temperature in DAPI solution (dilution 1:1000) to stain nuclei. All immunostained samples were stored in PBS at 4 °C until imaging. Fluorescent images were collected with an Axio Observer Z1 confocal microscope (Zeiss, Germany). Samples were excited at 488 nm (phalloidin), 555 nm (YAP), 639 (lamins) and 405 (DAPI), and the emissions were collected in the 500-530 nm, 560-610 nm, 640-650 nm and 420-480 nm ranges, respectively.

3.4.9 AFM for Cell Mechanics

The contact mechanics of the live cells constrained on flat or patterned substrates were determined by probing the cells with an AFM (JPK NanoWizard II). The probes used in this study were soft silicon nitride cantilevers with a square pyramid tip incorporated at the free end (PNP-DB,

NanoWorld, nominal spring constant 0.06 N/m). Spring constants of the cantilevers were measured independently for each experiment. The AFM was mounted on a Zeiss LM 510 confocal microscope to enable coaligning the AFM tip with cells. All probe indentations were performed over the central region of the cell in an area where the nucleus was present by performing a force mapping. Contact between the AFM tip and cell was defined by visually noting when the cantilever deflection deviated from a linear extrapolation of zero force. Force curves were typically recorded at a scan rate of 1 Hz, corresponding to a maximum loading rate of 1 nN/s and a maximum force of 1 nN. Typically, 64 force curves were measured over a cell area of 10 x 10 μm. Three separate experiments were performed on each topography for each timepoint, with 64 force-versus-indentation curves measured from each of ten aligned cells per pitch (indentation speed, 1 μm /s). Mechanical properties of cells, in terms of Young's modulus (E) values were estimated by fitting the force-indentation curve with Hertzian model for linearly elastic materials. The Young's modulus of the hTERT cells on each sample was quantified by calculating the median of the eight values with the greatest distance from the substrate (approximately corresponding to the nucleus).

Approximately thirty cells were indented for each time point. The individual elasticity values for a sample were collected via the JPK data processing software providing the distribution of elasticity values. Once collected the data, we used Microsoft Excel to compute the average, the median and the standard deviation of each cell's Young's modulus, corresponding to 64 force curves. We consider the points in which the nucleus was visible to compute its mechanical properties (the 8 points with the greatest distance from the substrate). Young's moduli at the subsequent times were normalized respect to the elasticity values of the flat specimen (t=0-).

3.4.10 Analysis of FAs and nuclear morphology and H3K9, YAP and Lamins fluorescence intensity

Different cell compartments were stained using immunofluorescence techniques and successively high-resolution confocal imaging was used to observe the single cell.

- FAs and nucleus morphology were analysed using the command "analyse particles" in Fiji. This allows to extract information about area, length, A/R, shape and orientation of the nuclei and FAs.
- Nucleus volume was calculated via a custom written script in ImageJ. Briefly, Z-stack sections of nuclei were binarized. The area of each section was multiplied by the voxel height (Vh)

and the volume was expressed as the sum of the areas*Vh comprising the stack Lamins intensity values were calculated using the command “analyse particles” in Fiji and considering the average gray values. This measures the sum of the gray values of all the pixels in the selection divided by the number of pixels.

- The YAP fluorescence density was measured was measured separately for the nuclear and cytoplasmic regions by calculating the ratio between the fluorescence intensity and the area of the individual cell compartments considered. The area of the cytoplasm was calculated by subtracting the area of the nucleus from the area of the whole cell.
- The DAPI intensity mean, the H3K9AC intensity mean (local and global) and the DAPI spots volume were quantified using Imaris software.

The average, median and standard deviation values of all the parameters listed above were calculated. To effectuate these measures, we collect a minimum of 15 z-stacks per each sample (sections 0.4). These sections were subsequently projected to a single plane to create an overall image of the specimen. All images in each group were collected with the same hardware and software settings.
Statistical significance was assessed through Kruskal-Wallis test (run in Matlab) with level of significance $p < 0.05$.

3.4.11 Correlation Plot

Corrplot in MatLAB was implemented to look for a correlation between morphological and mechanical properties of the nucleus. Average value of one variable was correlated to the average value of a different variable and the correlation was expressed in terms of the Spearman’s correlation coefficient. In the correlation plots, significant correlations are in red. For the sake of a clearer visualization variables are grouped in different categories.

3.5 Reference

1. Wu, M., Fannin, J., Rice, K. M., Wang, B. & Blough, E. R. Effect of aging on cellular mechanotransduction. *Ageing Res. Rev.* **10**, 1–15 (2011).

2. Handorf, A. M., Zhou, Y., Halanski, M. A. & Li, W.-J. Tissue Stiffness Dictates Development, Homeostasis, and Disease Progression. *Organogenesis* **11**, 1–15 (2015).

3. Lu, P., Weaver, V. M. & Werb, Z. The extracellular matrix: A dynamic niche in cancer progression. *J. Cell Biol.* **196**, 395–406 (2012).

4. Bianco, P. *et al.* The meaning, the sense and the significance: translating the science of mesenchymal stem cells into medicine. *Nat. Med.* **19**, 35–42 (2013).

5. Pittenger, M. F. *et al.* Multilineage potential of adult human mesenchymal stem cells. *Science* **284**, 143–147 (1999).

6. Engler, A. J., Sen, S., Sweeney, H. L. & Discher, D. E. Matrix elasticity directs stem cell lineage specification. *Cell* **126**, 677–689 (2006).

7. Downing, T. L. *et al.* Biophysical regulation of epigenetic state and cell reprogramming. *Nat. Mater.* **12**, 1154–1162 (2013).

8. Huang, A. H., Baker, B. M., Ateshian, G. A. & Mauck, R. L. Sliding contact loading enhances the tensile properties of mesenchymal stem cell-seeded hydrogels. *Eur. Cell. Mater.* **24**, 29–45 (2012).

9. Le, D. M., Kulangara, K., Adler, A. F., Leong, K. W. & Ashby, V. S. Dynamic topographical control of mesenchymal stem cells by culture on responsive poly(ε-caprolactone) surfaces. *Adv. Mater. Deerfield Beach Fla* **23**, 3278–3283 (2011).

10. Ng, C. C. A. *et al.* Using an electrical potential to reversibly switch surfaces between two states for dynamically controlling cell adhesion. *Angew. Chem. Int. Ed Engl.* **51**, 7706–7710 (2012).

11. *Polymeric nanostructures and their applications*. (American Scientific Publ, 2007).

12. Barrett, C., Natansohn, A. & Rochon, P. Cis-Trans Thermal Isomerization Rates of Bound and Doped Azobenzenes in a Series of Polymers. *Chem. Mater.* **7**, 899–903 (1995).

13. Rianna, C. *et al.* Spatio-Temporal Control of Dynamic Topographic Patterns on Azopolymers for Cell Culture Applications. *Adv. Funct. Mater.* **26**, 7572–7580 (2016).

14. Ambrosio, A. *et al.* Realization of submicrometer structures by a confocal system on azopolymer films containing photoluminescent chromophores. *J. Appl. Phys.* **107**, 083110 (2010).

15. Docheva, D. *et al.* Researching into the cellular shape, volume and elasticity of mesenchymal stem cells, osteoblasts and osteosarcoma cells by atomic force microscopy. *J. Cell. Mol. Med.* **12**, 537–552 (2008).

16. Ventre, M., Causa, F. & Netti, P. A. Determinants of cell–material crosstalk at the interface: towards engineering of cell instructive materials. *J. R. Soc. Interface* **9**, 2017–2032 (2012).

17. Natale, C. F., Ventre, M. & Netti, P. A. Tuning the material-cytoskeleton crosstalk via nanoconfinement of focal adhesions. *Biomaterials* **35**, 2743–2751 (2014).

18. Guo, M. *et al.* Cell volume change through water efflux impacts cell stiffness and stem cell fate. *Proc. Natl. Acad. Sci.* **114**, E8618–E8627 (2017).

19. Kouzarides, T. Chromatin Modifications and Their Function. *Cell* **128**, 693–705 (2007).

20. Haberland, M., Montgomery, R. L. & Olson, E. N. The many roles of histone deacetylases in development and physiology: implications for disease and therapy. *Nat. Rev. Genet.* **10**, 32–42 (2009).

21. Zhou, J. *et al.* Genome-wide profiling of histone H3 lysine 9 acetylation and dimethylation in Arabidopsis reveals correlation between multiple histone marks and gene expression. *Plant Mol. Biol.* **72**, 585–595 (2010).

22. Wang, N., Tytell, J. D. & Ingber, D. E. Mechanotransduction at a distance: mechanically coupling the extracellular matrix with the nucleus. *Nat. Rev. Mol. Cell Biol.* **10**, 75–82 (2009).

23. Feldherr, C. M. & Akin, D. The permeability of the nuclear envelope in dividing and nondividing cell cultures. *J. Cell Biol.* **111**, 1–8 (1990).

24. Tijore, A., Wen, F., Lam, C. R. I., Tay, C. Y. & Tan, L. P. Modulating Human Mesenchymal Stem Cell Plasticity Using Micropatterning Technique. *PLoS ONE* **9**, e113043 (2014).

25. Li, Y. *et al.* Biophysical Regulation of Histone Acetylation in Mesenchymal Stem Cells. *Biophys. J.* **100**, 1902–1909 (2011).

26. Cho, S., Irianto, J. & Discher, D. E. Mechanosensing by the nucleus: From pathways to scaling relationships. *J. Cell Biol.* **216**, 305–315 (2017).

27. Nardone, G. *et al.* YAP regulates cell mechanics by controlling focal adhesion assembly. *Nat. Commun.* **8**, 15321 (2017).

28. Halder, G., Dupont, S. & Piccolo, S. Transduction of mechanical and cytoskeletal cues by YAP and TAZ. *Nat. Rev. Mol. Cell Biol.* **13**, 591–600 (2012).

29. Donnaloja, F., Carnevali, F., Jacchetti, E. & Raimondi, M. T. Lamin A/C Mechanotransduction in Laminopathies. *Cells* **9**, (2020).

30. Zhao, B. *et al.* Cell detachment activates the Hippo pathway via cytoskeleton reorganization to induce anoikis. *Genes Dev.* **26**, 54–68 (2012).

31. Dupont, S. *et al.* Role of YAP/TAZ in mechanotransduction. *Nature* **474**, 179–183 (2011).

32. Zou, R. *et al.* YAP nuclear-cytoplasmic translocation is regulated by mechanical signaling, protein modification, and metabolism. *Cell Biol. Int.* **44**, 1416–1425 (2020).

33. Swift, J. *et al.* Nuclear Lamin-A Scales with Tissue Stiffness and Enhances Matrix-Directed Differentiation. *Science* **341**, 1240104–1240104 (2013).

34. González-Cruz, R. D., Sadick, J. S., Fonseca, V. C. & Darling, E. M. Nuclear Lamin Protein C Is Linked to Lineage-Specific, Whole-Cell Mechanical Properties. *Cell. Mol. Bioeng.* **11**, 131–142 (2018).

35. Dasgupta, I. & McCollum, D. Control of cellular responses to mechanical cues through YAP/TAZ regulation. *J. Biol. Chem.* **294**, 17693–17706 (2019).

36. Dahl, K. N., Ribeiro, A. J. S. & Lammerding, J. Nuclear shape, mechanics, and mechanotransduction. *Circ. Res.* **102**, 1307–1318 (2008).

Chapter 4

4 Modulation of cell shape

4.1 Introduction

The control of cell shape in vitro using different designs of micropatterned substrates is considered a useful instrument to investigate the fundamental mechanisms of morphogenesis. The patterning of cell adhesion motifs or topographic relieves has been shown to regulate cell architecture[1,2], polarity[3–5], migration[6,7] and differentiation[8,9]. The dynamics of cellular responses to changes in the microenvironment is a fundamental property of living systems that ensures the functional and mechanical coherence of tissues during development or renewal[10]. In the previous chapters, we used the micropatterning technique to demonstrate that cell behaviour is strongly sensitive to the spatial distribution of focal adhesions as well as to shape. In more details, in the second chapter we characterised the mechanical and morphological properties of cells confined in both isotropic and anisotropic shapes on flat and nanopatterned surfaces under static conditions. In the third chapter, we observed the behaviour of cells confined in circular and rectangular shapes subjected to dynamic topographic stimuli, i.e. linear nano-topographies whose inscription was limited to the cell adhesion area. In this chapter, we analyse the variation over time of the tensional and morphological state of the cells by changing shape and topography simultaneously, i.e. cells having initially a circular shape and subsequently became elongated by the application of a linear nanopattern whose inscription covered a greater surface area than the adhesion area. By combining different light-sensitive switches reacting to different wavelengths we fabricated arrays of signals whose display could be controlled in an orthogonal manner, thus increasing the complexity of the system. By applying different materials and innovative imaging techniques we explored the cell-substrate interface and the mechanisms through which cell geometry regulates cell signalling. Once again, we observed that the

field of dynamic platforms, realized through confocal microscopy, should potentially contribute to unveil complex biological events such as the modulation of cell shape.

Cell shape in vitro can be directed by geometrically defined micropatterned adhesion substrates. However conventional methods are limited by the fixed micropattern design, which cannot recapitulate the dynamic changes of the cell microenvironment[11]. Here, we manipulate the shape of living cells in real time by using a laser light trigger in a non-invasive spatio-temporal controlled way to introduce additional geometrically defined adhesion sites. The nanometric resolution of the laser patterning allowed us to identify the critical distances between cell adhesion sites required for cell shape extension. This method allows the precise control of specific actin-based structures that regulate cell architecture. Actin filament bundles, initially randomly organised in circular-shaped cells, were induced to align and distribute to form a rectangular-shaped cell in response to specific dynamic changes in the cell adhesion pattern. We have developed a simple method to modify the cell repellent properties of the polyethylene glycol (PEG) coating in the proximity of a living single cell already attached with a specific shape to a flat substrate. The manipulation of the adherent properties in the microenvironment of a single cell with sub-micrometre resolution enables the precise control of intracellular architecture remodelling in real time.

4.2 Results and Discussion

4.2.1 Laser patterning

Modification of a PEG layer on Poly Disperse Red 1 (pDR1)-coated glass can be an efficient and versatile micropatterning method to accurately define geometries that can stereotypically direct cell adhesion and shape. Initial oxidation of PEG was achieved by deep UV exposure (wavelength below 200 nm) through a chromium mask. Indeed, deep UV creates ozone which oxidises the surface and allows protein adsorption[12]. Using this technique and covering the oxidised areas with fibronectin (**Figure 4.1 a**), we forced the hTERT cells to acquire a circular shape (surface area=1300 μm^2). 24 hours after seeding, we embossed a linear pattern on the initial flat surface using the light polymer activation technique (**Figure 4.1 c**). Single-photon confocal microscopy was used to emboss precise and complex submicrometric patterns of the desired size on pDR1m thin films. Since the maximum absorption band of this azo-polymer is 467 nm, the laser source with wavelength value of 488 nm was used to induce the continuous trans-cis-trans isomerization of pDR1m molecules, favouring the resulting surface mass migration. The laser beam path could be controlled via software by drawing a specific region of interests (ROIs) in which the laser was activated only in the selected areas with a high spatial resolution (nm order). This photo-patterning technique, in a highly confined volume, induced local modification of the irradiated materials by modifying the repellent properties of the polyethylene glycol (PEG) coating in the vicinity of a single living cell. In particular, the mass transport induced by trans-cis isomerization of azobenzene molecules caused the nanopattern formation covering an area larger than that of the cell and the PEG removal along the ridges. To test this behaviour, in the absence of cells, we marked the substrate with fluorescent fibronectin 24 hours after the nanopattern embossing. As can be seen in the **Figure 4.1 b**, the fibronectin covered the areas without PEG, giving cells a larger area to adhere to and thus favouring elongation and the subsequent change in cell shape. The surface modifications were subsequently characterised using atomic force microscopy (AFM) (**Figure 4.1 d-f**). Parallel arrays of linear ROIs 100 µm long, separated by 700 nm and approximately 120 nm high were inscribed by placing the circular cell in the centre.

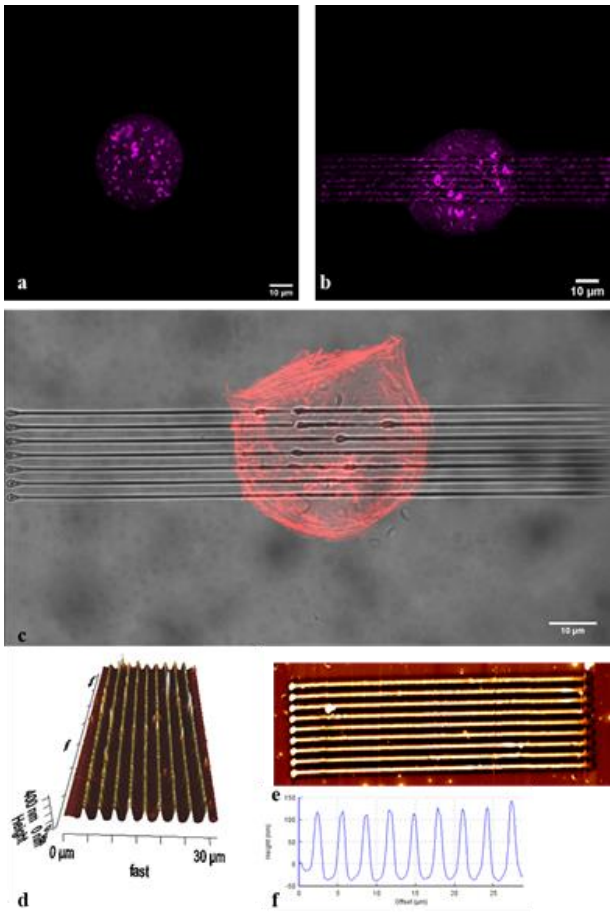

Figure 4.1:. *In-situ topographical changes induced by using the confocal technique.* ***(a)*** *Circular adhesive island coated with fluorescent fibronectin on flat substrate.* ***(b)*** *Area coated with fluorescent fibronectin 24 hours after the nanopattern embossing.* ***(c)*** *Confocal images of a single cell after linear pattern inscription (t=0+). Laser exposure was 60 seconds. AFM image of linear pattern obtained on pDR1m with Argon laser at 488 nm in 60 seconds:* ***(d)*** *three-dimensional image* ***(e)*** *bi-dimensional topographical image and* ***(f)*** *cross-section profile.*

The cell shape could then be modified by combining the photomask and confocal photopatterning techniques. The process is schematised in **Figure 4.2** where we show the first step of PEG removal by illuminating a region defined by a series of parallel horizontal bars positioned in the centre of a circular shaped cell. After this illumination, the cell needed time to form new mature FAs as well as to adhere to the available regions and adopted an almost rectangular shape.

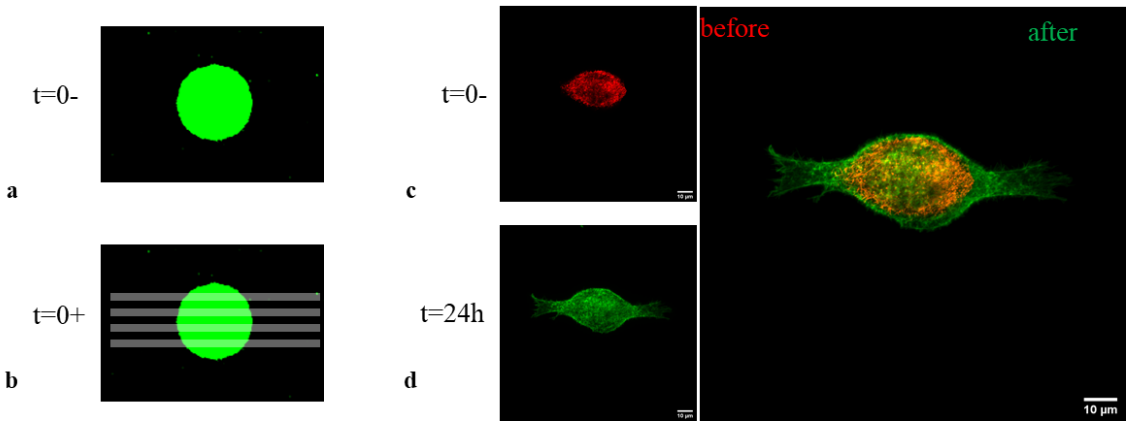

***Figure 4.2**: Graphical representation of the process. **(a)** Cell confined in circular shape on flat surface at t=0. **(b)** Inscription of the nanotopography consisting of a series of parallel horizontal lines positioned in the centre of the circular cell using confocal microscopy. Fluorescence image **(c)** of the circular cell on flat substrate t=0 and **(d)** of the elongated cell 24 hours after the nanopattern inscription. Cell cytoskeleton is stained with Phalloidin. Scale bar 10 µm.*

4.2.2 Control of actin network remodelling

The cell shape is supported by various structural elements including the actin filaments. These are highly dynamic and remodelled during cell shape changes[13]. Since the assembly of each structural element depends on the local adhesion geometry[1] we investigated whether laser-induced patterning could be used to guide cell shape changes and we then characterized the precise intracellular remodelling of the structural elements. The trans-cis isomerisation of azobenzene molecules located in the illuminated regions (ROIs) determines molecular motions at the nanoscale and mass transfer at the micrometre-scale[14]. In fact, when randomly oriented azobenzene molecules are irradiated by a polarized light having an appropriate wavelength, the molecules reorient in the direction orthogonal to the polarization plane. We hypothesize that the mass transport generated in the areas previously covered by PEG caused surface changes in a way that the surface is no longer anti-adhesive thus allowing cells to adhere. Any type of actin-based structure could be induced, displaced, or removed during the variation of the circular cell shape into an elongated one by adding new adhesive regions of defined geometries. In more details, extending the length of the nano-ridges (beyond the area of the circle) promoted the FAs reassembly which in turn implied a rearrangement of the actin bundles so that they remained confined between the grooves.

We studied the variation in cell shape and thus the dynamics of the assembly of cytoskeleton structures using immunofluorescence staining and confocal microscopy. We observed that the organisation of the actin cytoskeleton and the formation of stress fibres are strongly dependent on the shape of the adhesive island. At the initial time (t=0-) cells were confined in a circular shape on flat

surfaces. In fact, the mean value of cell A/R measured 1 and the mean value of cell roundness was approximately 1. In the hours following the nanopattern inscription, from t=0+ up to a maximum of 24 hours, it was evident that the cell was assuming a more elongated shape although they maintained a constant area (**Figure 4.3 a**). In this respect, the cell A/R values increased over time while those of cell roundness decreased (**Figure 4.3 b, c**).

Live patterning was so used to precisely control and orient the actin network polarization step. Circular cells on flat substrate consisted of a disorganised network of thin actin filaments with several filopodial protrusions and cortical actin running along the contour of the coated adhesive island. Furthermore, when the cells were cultured on isotropic surfaces, no actin cap was detected after 24 hours of culture on flat surfaces. So, initially, actin networks did not display any significant polarized architecture when cultured on a flat substrate (**Figure 4.3 d**). Within the first few hours of pattern inscription, the cells began to elongate and outward-curved actin fibres formed along the major axis of the cell and were located on either side of the nucleus (**Figure 4.3 e**). Four hours after the pattern inscription, the cells started to extend on the linear ridges and the central actin fibres became less curved and tended to adopt a straight morphology (**Figure 4.3 f**). 24 hours after pattern inscription, the cells assumed an elongated shape and showed a cytoskeleton predominantly composed of thick actin fibres oriented along the major axis of the cells (**Figure 4.3 g**).

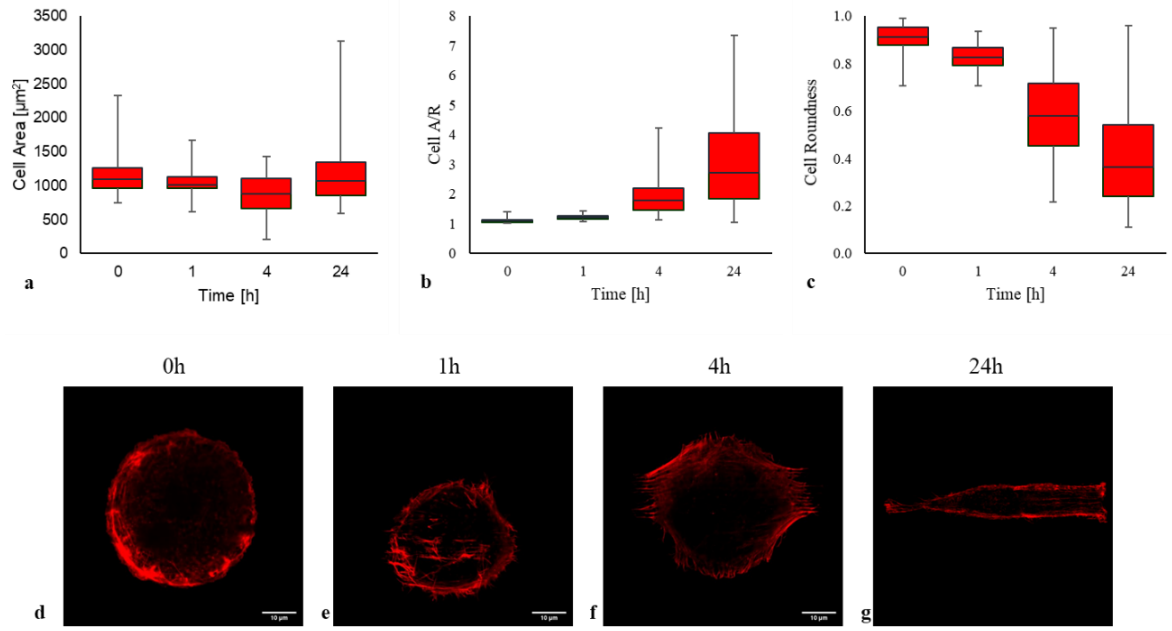

Figure 4.3: *Box and whiskers of **(a)** the cell projected area, **(b)** the cellular A/R and **(c)** the cell roundness of hTERT cells in time evolution. t= 0 indicates circular cells on flat pDR1m substrate, t= 1, 4 and 24 h indicate cells on nanopatterned pDR1m substrate respectively 1, 4, and 24 hours after the pattern inscription. Confocal images of fixed circular hTERT on **(d)** flat surface and **(e)** 1, **(f)** 4 and **(g)** 24 hours after the linear pattern inscription. Cell cytoskeleton is stained with Phalloidin (red).*

Therefore, the presence of the topographic nanopattern implied, in addition to an increased orientation of the basal fibres, an actin cap made up of thin fibres present in the upper part of the perinuclear region. Upon completion of this extension and contraction phase, cells ended up with a highly asymmetrical shape and polarized actin network.

Here, we have demonstrated that this new and simple method for surface nano-patterning in live cell culture offers a precise control in real time of cell shape modifications and intracellular architecture. This method should pave the way for further investigations of dynamic cellular responses to nano- and micro-scale changes in the microenvironment.

4.2.3 Focal Adhesion Remodelling

To study how cells change their shape and adapt their morphology following topographic signals, we observed the dynamics of FAs. The nano-sized topographical patterns created by illuminating the parallel ROIs positioned centrally to the circular cell resulted in the formation of zones favourable to the formation and growth of FAs juxtaposed to unfavourable ones. The nanopatterning techniques thus allowed a finer control over the FAs shape and positioning. The latter in turn influenced the arrangement of the actin bundles, which in turn exerted pressure on the nuclei, encouraging a change in their morphology. In this context, by combining micro- and nanopatterning techniques, we achieved adequate confinement of the cell in a circular shape that subsequently was elongated stimulated by the nanotopographic signals.

In this respect, the FAs that initially (t=0) anchored the circular cells to the flat substrates appeared localised along the circumference of the cell (**Figure 4.4 a**) and therefore characterised by a random orientation (mean value 43°) (**Figure 4.4 g**). Following the linear topographical stimulus imposed, the cells were able to elongate and spread into the initially non-adhesive areas by reassembling the FAs. In the case analysed in the previous chapter, circular cells were subjected to linear topographical signals but limited in the area of cell adhesion. In this context, the cells needed approximately 24 hours to align the FAs in the direction of the underlying pattern. In contrast, in the case now investigated, the circular cells were subjected to linear topographical signals that covered an area greater than that of cell adhesion. The FAs appeared oriented in the direction of the underlying topography already one hour after pattern inscription (mean value 30°) (**Figure 4.4 b, c**) and after 24 hours they were found to be restricted to the extremities of elongated cells (**Figure 4.4 d, g**).

Furthermore, during the first hours after the pattern embossing, the mature FAs of the cells maintained a mostly constant area and length over time irrespective of the inscription of the underlying nanopattern and the resulting change in cell shape (**Figure 4.4 e and f**). Twenty-four hours after pattern inscription, the FAs area increased with the extent of cell elongation, suggesting that the overall tension per cell increased with cell elongation. Indeed, FAs of elongated cells (t=24h) on linear patterns showed length (average value 2.03 ± 0.3 µm) and area (average value 1.0 ± 0.5 μm^2) comparable to those measured on the flat substrate (length = 1.71 ± 0.4 µm, area = 0.8 ± 0.1 μm^2), which displayed widely distributed FAs.

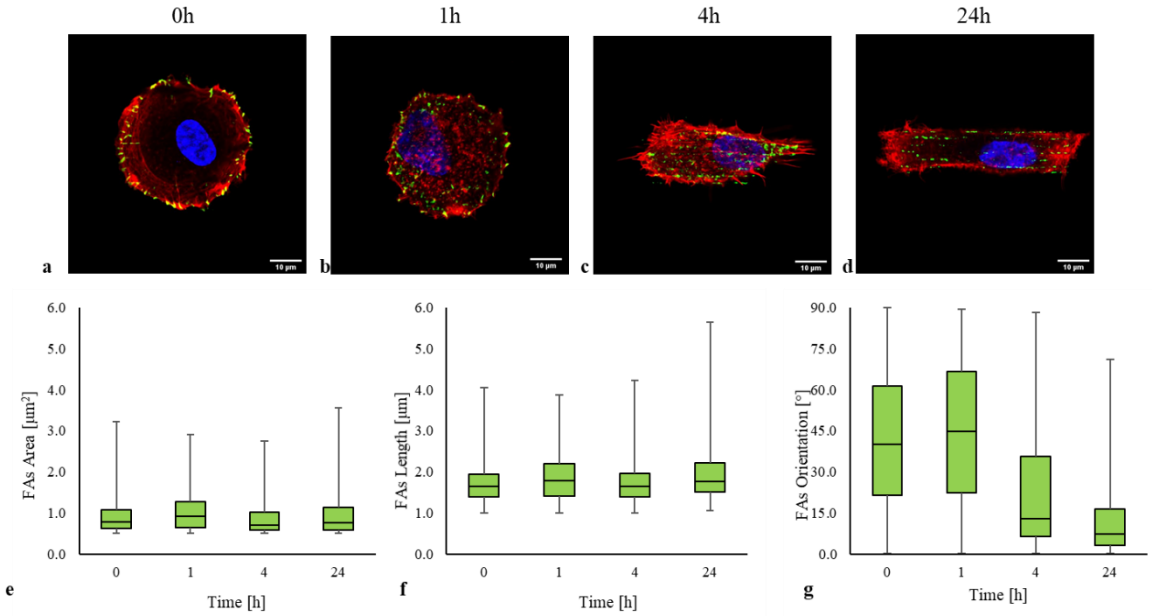

Figure 4.4: *Confocal images of fixed circular hTERT on* ***(a)*** *flat surface and* ***(b)*** *1,* ***(c)*** *4 and* ***(d)*** *24 hours after the linear pattern inscription. Cell cytoskeleton was stained with Phalloidin (red), FAs were immunostained for vinculin (green), and nuclei were stained with DAPI (blue). Box and whisker of* ***(e)*** *the FAs area,* ***(f)*** *the FAs length and* ***(g)*** *the FAs orientation in time evolution.*

In conclusion, hTERT cells of circular shape cultured on the flat surface formed FAs only on the perimeter of the adhesive island, while they were not able to elongate and spread in the non-adhesive areas. After the cells adapted their morphology following the shape changes induced by nanotopography, i.e. when the initial circular cell was transformed into a rectangular one, the cells spread over the whole new bio-adhesive area, showing actin bundles with FAs oriented at various angles at their termini.

4.2.4 Change in the cell mechanics

We have demonstrated how extracellular topographic signals can alter the FAs assembly, which in turn implies changes in cytoskeletal structure. The technique we have implemented is expected to induce changes of the stress state of cells due to a drastic change in cell shape and structure. In fact, changes in the FAs size and arrangement, as well as those of the actin fibres, inevitably induced alterations in cellular properties and more specifically in their ability to transduce mechanical signals from the ECM. To characterize the dynamic interplay between cell mechanics and cytoskeleton assembly, we combined quantitative imaging techniques of the cell cytoskeleton (using immunofluorescence-staining) with methods to measure cell stiffness using atomic force microscopy. Then, we carefully evaluated the evolution over time of the mechanical properties of living cells initially confined in circular shapes on flat substrates and subsequently in contact with the nanopatterned substrate. Measurements were performed in the vicinity of the nuclear regions but due to the heterogeneous and dynamic nature of living cells, it was again not possible to isolate the contribution of individual internal cellular components on the response of the whole cell to the topographic signal. Circular cells, in the absence of topography, were characterised by randomly oriented actin fibres (**Figure 4.3 d**). Their Young's moduli measured 2.27 ± 0.17 kPa (average value at t=0-). As soon as the linear nanopattern was applied (t=0+), there was a rapid decrease of the mechanical properties lasting 1 – 2 hours after the pattern was perceived (**Figure 4.5**). During this phase, the cells redistributed the FAs, which anchored differently to the substrate, leading to reassembly of the cytoskeleton and more precisely to an orientation of the basal fibres in the direction of the underlying pattern. In this respect, once the previously disoriented stress fibres became elongated and aligned in the direction of the underlying pattern, the values of the elastic moduli increased over the following hours until they reached their maximum values 24 hours after pattern inscription (the average value was 2.86 ± 0.27 kPa at t=24h), i.e. when the cell had assumed its rectangular shape.

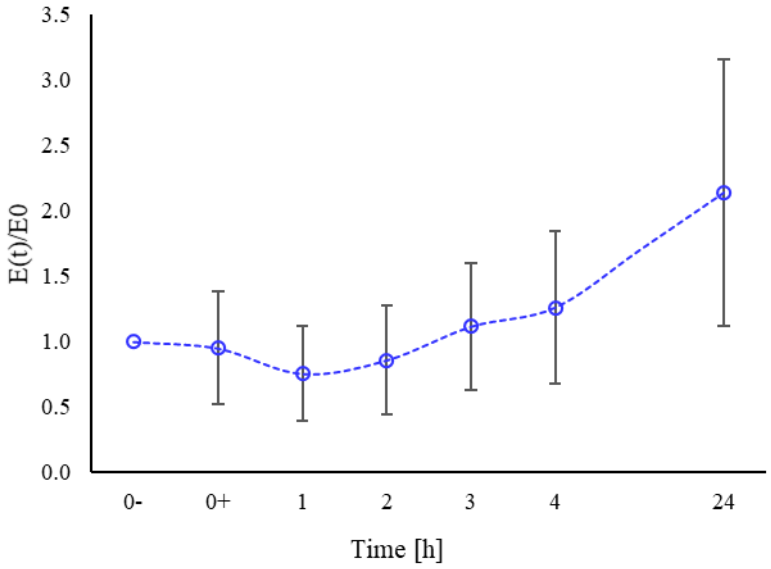

Figure 4.5: *Plot of the Young's moduli variation over time of circular cells cultured on flat surfaces and subsequently in contact with nanotopographic pattern. Using 't= 0-' we indicate cells on flat pDR1m substrate, whereas with 't=0+' we indicate the immediate moment of cell-topography contact.*

Our results confirmed a clear contribution of the nanotopography imposed on the confined circular cells in determining an increase in cell stiffness. The timing of the increase in Young's modulus was consistent with the phase of increasing stabilisation of the stress fibres due to their elongation and orientation in the direction of the underlying pattern.

In agreement with the static case (see Chapter 2), the rectangular cells that perceived the linear topographic nanopattern showed higher average moduli than the circular cells. Therefore, modifying the cell shape and more specifically making a previously isotropic cell an anisotropic one, may be effective in modifying cell mechanics and exhibiting a more rigid nuclear region.

Furthermore, these results concerning the variation of mechanical properties between initially circular and subsequently elongated cells agree with our previous work[15]. In the latter, we evaluated the behaviour of spread cells (unconfined) on flat substrates and subsequently forced them to adapt to the underlying curvature induced by topographic signals. Again, the cells were able to detect and reconfigure their shape as early as 2-3 hours after pattern inscription. But since (local) coalignment with the direction of the pattern required the cytoskeleton to adapt to the underlying curvature, we observed that cells cultured on circular patterns consistently expressed a rather diffuse cytoskeleton with the presence of small FA. A weakly mature cytoskeleton endowed cells with a decreased cytoplasmic stiffness, as measured by nanoindentation.

4.2.5 Nuclear Deformation

The change in cell morphology induced by the nanotopographical signals indicates that the imposed constraints cause a different distribution of stress fibres and thus of internal cell forces that regulate the deformation and morphology of the nuclei. To this aim, the morphology of the nuclei of cells cultured on flat and patterned surfaces was examined using immunofluorescence staining and confocal microscopy.

At first, we observed that the nuclei of circular cells at t=0 appeared mostly spherical in shape (**Figure 4.4 a**). In this regard, considering the two-dimensional projection, we calculated the A/R and roundness of the nuclei at the initial time whose average values measured 1.4 and 0.8 respectively (**Figure 4.6 a, b**). One hour after the perception of the underlying pattern, the nuclei still maintained a spherical shape, even if they had a smaller area (**Figure 4.6 d**). Only 24 hours after pattern inscription the nuclei appeared significantly more elongated ($p<0.03$) and less round ($p<0.1$) than the nuclei of cells observed on a flat substrate (t=0). In fact, the rectangular shape that the cell was assuming 24 hours after the nanopattern inscription implied the gradual elongation of the membrane over time and the assembly of stress fibres which in turn exerted mechanical stress on the nuclear envelope, thus determining the more elongated shape of the nucleus.

Elongating cells exerted increasing cytoskeletal tension over time along the major axis of the cell. This involved the formation of stress fibres able to exert vertical and lateral compressive forces on the nucleus. We subsequently verified that this action certainly influenced the shape of the nuclei but also their orientation. In this regard, by calculating the angle formed between the major axis of the nuclei and the reference axis of the image (x axis), we observed that if at time zero the shape was spherical, i.e. randomly oriented, as the hours following the nanopatterns inscription increased, the major axis of the nucleus formed smaller angles, indicating a larger orientation of the nuclei in the direction of the underlying pattern (**Figure 4.6 c**).

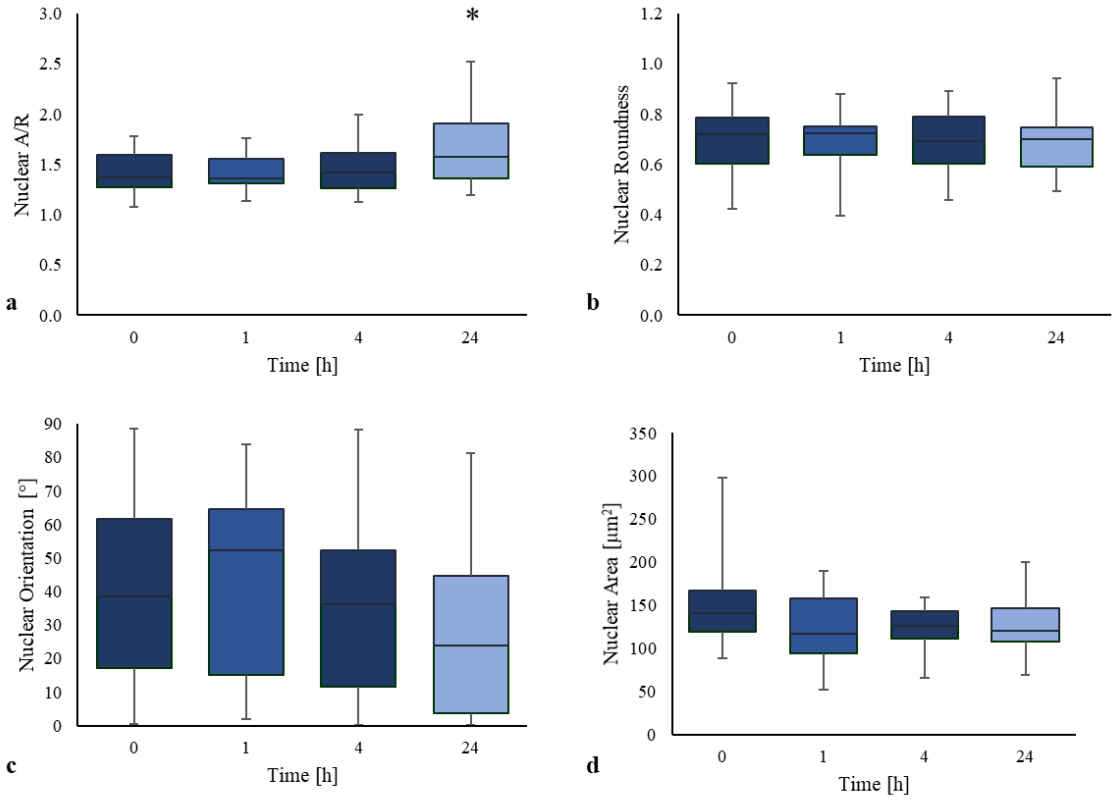

Figure 4.6: *Box and whiskers of* ***(a)*** *the nuclear A/R,* ***(b)*** *nucleus roundness,* ***(c)*** *the nuclear orientation and* ***(d)*** *the nuclear projected area of circular shaped cells in time evolution. t= 0 indicates rectangular cells on flat pDR1m substrate, t= 1, 4 and 24 h indicate cells on nanopatterned pDR1m substrate respectively 1, 4 and 24 hours after the pattern inscription. Asterisks indicate significant difference with respect to t=0.*

To sum up, forcing the cells to spread unidirectionally on elongated patterns the nuclear A/R increased significantly, indicating a relation between cell and nuclear shape. As the cell A/R increased, nuclei became increasingly aligned with respect to the long axis of the cell, to finally reach a well-oriented state for the more pronounced elongated cell shape. These results indicated that the nucleus, initially rounded and randomly oriented in circular-shaped cells, became progressively deformed and anisotropically oriented as the cell elongates and spreads. As far as the nuclear area is concerned, the measure showed that it was not significantly influenced by topographic signals. This parameter decreased slightly as soon as the cell perceived the topographic signal and then remained constant over the following hours. This observation could be explained by a shrinkage of the nucleus due to the highly folded structure of the nuclear membrane.

4.2.6 Influence of cell elongation on chromatin assembly

In the previous sections, we have observed that changes in cell shape, inducted by topographical signal, can affect nuclear architecture and mechanics. At this point, we asked whether large-scale changes in cell shape (from circular to elongated cell shape) could induce a change in chromatin condensation. To answer this question, chromatin conformation was analysed by high-resolution imaging techniques. Combinations of fluorochromes were used to distinguish differently coloured targets simultaneously in a single cell. Cytoskeleton and cell nucleus staining using conventional immunofluorescence techniques and high-resolution confocal imaging was used to achieve the 3D reconstruction of deformed nuclei. Firstly, we examined chromatin organisation using a quantitative procedure based on DAPI staining. Indeed, DAPI uptake depends on the total amount of DNA, but also on its level of condensation. To this end, we initially quantified the volume and number of DAPI spots. As shown in the figure, an increase in volume and a decrease in the number of DAPI spots indicated a marked reorganisation of the chromatin distribution associated with nuclear deformation (**Figure 4.7 c**). More in details, this trend suggested that adjacent HC spots fused with each other to form larger HC spots representative of a denser chromatin. Highly condensed chromatin domains showed greater size and fluorescence intensity than less condensed ones (**Figure 4.7 d**). Therefore, the increase in chromatin compaction was detected as both an increase in DAPI density within heterochromatin, as well as an increase in heterochromatin (spot) volume. From the fluorescence images we qualitatively observed that when the cells were disc-shaped, the chromatin was largely extended within a rounded nucleus, with a few small, centrally located condensed domains (**Figure 4.7 a**). When the cell elongated, the nucleus deformed, and chromatin tended to condense in the nuclear periphery (**Figure 4.7 b**). Moreover, to confirm this behaviour, we quantified the fluorescence intensity of the antibody against the H3K9ac (euchromatin marker) both when the cell had a circular shape on a flat surface and when the cell had an elongated shape 24 h after pattern inscription. The clear reduction in mean fluorescence intensity of histone in the nucleus indicated a reduction in acetylation or an increase in chromatin condensation (**Figure 4.7 e, f**).

In addition, we observed that this increasing trend in chromatin condensation correlated with the increase in mechanical properties measured in the proximity of the nucleus. We think that this behaviour is explained by the progressive condensation of chromatin, which occurred from the first to 24 hours after the pattern inscription, resulted in the stiffening of the nucleus of hTERT cells (**Figure 4.5**).

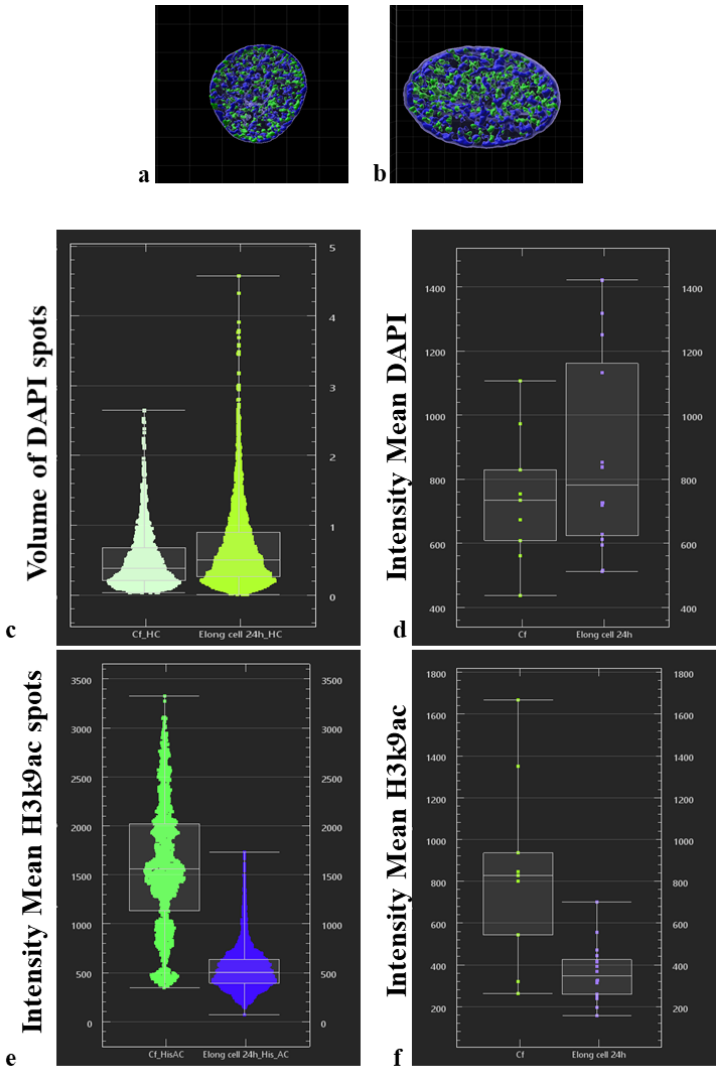

Figure 4.7: *3D reconstruction of* ***(a)*** *circular cell nucleus on flat surface (t=0) and* ***(b)*** *elongated cell nucleus 24 hours after pattern inscription. Nuclei are immunostained for DAPI (blue) and H3k9ac (green). Box and whiskers of* ***(c)*** *volume of DAPI spots [μm^3]* ***(d)*** *the intensity mean of DAPI in the whole nuclei* ***(e)*** *the intensity mean of H3k9ac spot and* ***(f)*** *the intensity mean of H3k9ac in the whole nuclei at t=0 on flat surface (Cf) and 24 hours after the pattern inscription (Elong cell 24h).*

We thus found that hTERTs, initially circular in shape and subsequently elongated by topographical stimuli, entered in a less transcriptionally active state as soon as they changed shape. This probably occurred because the remodelling of the actin cytoskeletal structure resulted in changes in cell morphology. The elongated nuclear shape probably caused a difference in nuclear pores, which in turn affected the rate of nucleocytoplasmic transport of epigenetic modifiers and thus the condensation state of chromatin. In this respect, in agreement with chromatin condensation, we observed a change in nuclear morphology, in particular a significant decrease in nuclear volume ($p<0.04$) from 0 to 24 hours after the pattern inscription (**Figure 4.8**). This observation could be explained by a shrinkage of the nucleus due to the highly folded structure of the nuclear membrane.

These results confirm that the morphological change experienced by hTERTs when interacting with the nanoscale features of adhesive cellular materials is sufficient to induce epigenetic changes.

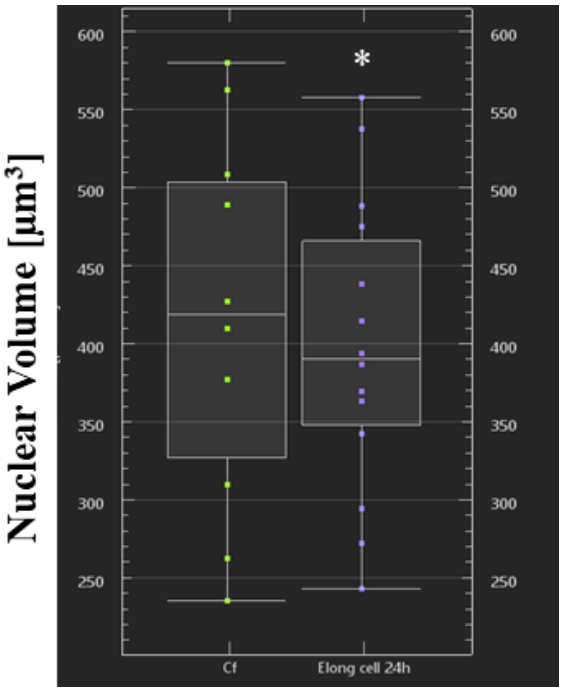

Figure 4.8: *Box and whiskers of the nuclear volume of circular shaped cells in time evolution. "Cf" indicates circular cells on flat pDR1m substrate (t=0), "Elong cell 24h" indicates the same cells elongated on nanopatterned pDR1m substrate 24 hours after the pattern inscription. Asterisks indicate significant difference with respect to t=0.*

4.3 Conclusion and Future prospective

The investigation of the stem cells response to microenvironmental cues is an area that is attracting great interest from the scientific community. Most of the literature reports, have focused on the use of static culture platforms[16]. With the system introduced in this chapter, we have observed how hTERT cells behave in a material microenvironment where biophysical properties change over time when passing from a flat to a nanopatterned substrate. The extracellular microenvironment exerts a powerful regulatory effect on cellular mechanics and morphology as well as on stem cell fate decisions. In particular, the delicate balance between cell-matrix interactions and cell geometry plays a key role during embryogenesis. In vitro, the characteristics of culture materials that regulate cell adhesion and spreading, including substrate topography, are effective in directing cell behaviour.

The interest for studying cell behaviour on pattern showing complex shapes lies in the fact that the presence of surface topography might influence contractility-mediated responses, including cell adhesion, motility and even gene expression. In this regard, it has also been shown that the presence of the pattern can coordinate the spatial arrangement of cancer cells and such a coordination promotes the activation of a stem cell-like phenotype with improved tumorigenic potential[17]. Since cell-generated forces are important triggers and regulators of signalling pathways that eventually dictate cell functions and fates, embossing topographic patterns can in principle enable controlling cell mechanics and mechano-transduction events. We have therefore presented a novel optical technique that superposes topographic patterns with submicron scale resolution on a biochemically micropatterned azopolymer films. The modular technique can implement drastic changes in cell morphology, cytoskeleton assemblies and cell mechanics consequently. This technique enables embossing topographic patterns on azopolymer films in a straightforward manner by controlling the position and movement of a focused laser beam. The possibility of writing-erasing patterns on the same substrate in the presence of cells confined in specific shapes paves the way to provide topographic stimuli according to time-space controlled programs, which is a key aspect to study time-dependent cell behaviour such as stem cell plasticity, cancer progression and morphogenesis. The reported method is useful to manipulate cell shape and mechanics in a facile and cost-effective manner and most importantly enables to investigate mechanotransduction events dynamically. We investigated how hTERT stem cells reacted to the transition flat-patterned surface in terms of changes in alignment, cell shape, mechanical properties using of immunofluorescence imaging and atomic force microscopy. We asked if and to what extent the pattern features we inscribed on the

azopolymers mostly affected cell adhesion in terms of area, morphology, nuclear mechanics, and chromatin assembly. For this reason, in this work it was interesting to note that by appropriately engineering cell culture substrates, it is possible not only to provide a conceptual picture of the mechanical coupling between cell shape and nuclear shape, but it is also possible to predict a nuclear stiffening and different epigenetic responses when the cell elongates.

Again, our experimental results could be incorporated into a mathematical model to be able to predict the development over time of the mechanical characteristics of the cells from the geometric and nanotopographic constraints imposed on the cells.

Recently, Heydari et al.[18] developed a computational multicomponent cell model, called the "virtual cell model" that had the capability to predict changes in whole cell and cell nucleus features in terms of shape, direction, and chromatin conformation on a range of cell substrates. Consistently with our experimental results, the virtual cell elongated along the grooves, and this led to change in nuclear morphology from spherical to ellipsoidal and the degree of orientation was evident on micropatterned surfaces rather than flat ones. In addition, this model allowed to predict the effect of cell confining geometry on the chain arrangement of simulated chromatin fibres in the nuclei, which may have roles in the several cellular processes. The virtual cell model was implemented as an integrated program via the C++ platform, and it was mainly developed to capture the cell mechanics on the substrates with different elastic properties and morphologies. It consisted of various components to simulate the outer membrane of the cell and nuclear envelope, cytoplasmic area, chromatin fibres, and extracellular matrix. A triangulated fluidic membrane was utilized to model the outer membrane of the cell and the nuclear envelope. The cell and nuclear membrane geometry were initially considered spherical with different volume. The cytoplasm and cytoskeleton network were modelled by a network of distributed and interconnected mass particles, which fill the space between the nucleus and the cell membrane. A bead-spring model with excluded volume interaction was used to simulate the chromatin fibres. The adhesion of the cell membrane to the substrate was modelled through a generic potential such that when the membrane elements were close enough to the substrate elements, they interact through the Lennard-Jones potential.

Once we have observed how topographical biophysical signals are able to radically change the morphology and stress state of the cell, in subsequent studies we could focus on assessing the molecular mechanisms that regulate the transduction of material signals in terms of transcription factor flux and the expression of specific genes. Subsequently, it would be interesting to evaluate the cellular response to multiple shape variations and to investigate whether there will be a "memory effect" of the shape-variation undergone.

Along these lines, specific matrices of time-varying topographic signals may eventually overcome the requirement for soluble factors to govern the cell differentiation programme. In this respect, we would like to demonstrate the importance of the timing of topographic signal delivery and subsequent cell differentiation. These data can clearly illustrate that the sequential application of biophysical signals can be a powerful tool to study dynamic changes in biological processes, an approach that can be useful to study tissue development, wound healing, and disease progression.

4.4 Experimental Section

4.4.1 General Materials

Trypsin and paraformaldehyde were provided from Thermo Fisher Scientific. Poly-Disperse Red 1-methacrylate (pDR1m), Chloroform, TRITC phalloidin, Triton X-100, bovine serum albumin (BSA), fibronectin solution and anti-paxillin monoclonal antibody were provided by Sigma-Aldrich.
Alexa Fluor 488 Phalloidin, Alexa Fluor 546 conjugated goat anti-mouse antibody, Rabbit pAb to Histone H3 (acetyl K9) - ChIP Grade (Cat. No. ab4441) and DAPI were purchased from Abcam. ASC52telo, hTERT immortalized adipose derived Mesenchymal stem cells were purchased from ATCC.

4.4.2 Dynamic Sample Preparation

10 μm diameter cover glasses are washed three times in acetone and sonicated for 15 minutes, then dried on a heated plate. Spin coating technique was used to produce thin films of pDR1m on cover glasses. pDR1m was initially dried overnight and then dissolved in chloroform at a 3% w/v concentration, sonicated and heated to 37°. 15 μl of this solution was used for each cover glass. The solution was spun over the cover glass using a Laurell spin coater (Laurell Technologies Co.) at 5000 rpm. The film thickness was assessed with a Dektak 150 Veeco profilometer. Only those samples display a uniform coating thickness of (approximately) 300 nm were used for the experimentations and analyses.

4.4.3 Micropatterning protocol

pDR1m substrates are activated by exposure to deep UV Printer (4D cell, Montreuil, France) for 15 min. Then the samples are incubated for 1 h with 0.1 mg ml^{-1} poly-L-lysine-g-poly(ethyleneglycol) (PLL(20)-g[3.5]-PEG(2); SuSoS Surface Technology, Dubendorf, Switzerland) at room temperature

(40 µL for each sample). After washing with distilled water, the treated surface was illuminated with deep UV light through a photomask.

The 4Dcell photomask is a quartz mask with a chromium designed coating for the aim of the micropatterning experiment. It is used for the printing of the micropatterns on slides, with deep UV. In this section we used only the region of the mask characterized by circular geometry (area =1300µm^2). The 4Dcell quartz mask is washed with absolute ethanol and it is illuminated for 10 min using the deep UV Printer, with its brown side facing the lamp. This makes the brown side of the mask hydrophilic. 2.5µL of millipore H_2O are added onto the brown side of the 4Dcell quartz mask and the PEGylated side of the sample is gently dropped onto the mask. Using the deep UV Printer, the 4Dcell mask is illuminated for 8 min with the silver side facing the lamp. 5 mL of distilled water are added on the mask to help detach the slides from it. The activated side is than incubated 1h at room temperature with 50 µL of fibronectin (final concentration of 50 µg ml^{-1}) and after it is rinsed with PBS.

4.4.4 Plating of the cells

hTERT are cultured in Mesenchymal Stem Cell Basal Medium (ATCC PCS-500-030). To make the complete growth medium, Mesenchymal Stem Cell Growth Kit (ATCC PCS-500-040) for Adipose and Umbilical-derived MSCs – Low Serum Components and G418 is added to the base medium. Cells are detached from the culture plate and centrifuged to remove traces of trypsin; the enzyme used to detach the cells. They are then resuspended in the culture medium and 35.000 cells are seeded per sample. Cells were cultured at 37 °C in a humidified atmosphere of 95% air and 5% CO_2. Cells should be spread on the patterns 2h after plating.

4.4.5 Dynamic Topographic Pattern Inscription

hTERT were cultured on pDR1m coated glass slides previously micropatterned (method described above) for 24 hours. Afterwards, real-time pattern inscription on cell-populated samples was performed by using a Axio Observer Z1 microscope (Zeiss, Germany). The isomerization of the azopolymer and its consequent mass transport were activated using an Argon laser at 488 nm and 1.3 mW of intensity with a 10x (N.A. 1.4) objective lens. Patterns were embossed on the pDR1m

substrates by illuminating with the laser light in specifically drawn regions-of-interest (ROIs). Parallel arrays of linear ROIs 100 µm long, separated by 700 nm and approximately were inscribed by placing the circular cell in the centre. The exposure time was 60 seconds.

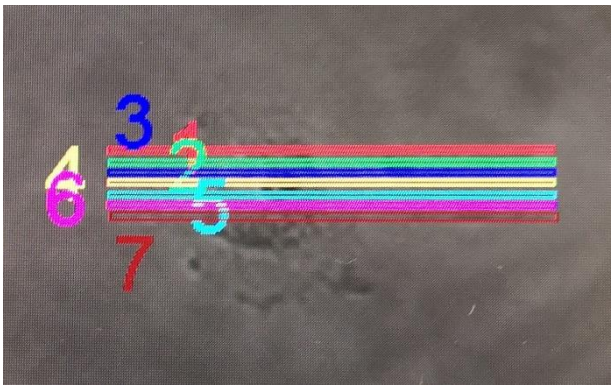

Figure 4.9: *Parallel ROI used to fabricate linear nanopattern on circular cell.*

4.4.6 AFM for Sample Surface Characterization

An atomic force microscope JPK NanoWizard II (JPK Instruments, Germany) was used to acquire images of pDR1m samples. An Axio Observer Z1 microscope (Zeiss, Germany) was combined to the AFM to control tips and sample position. Silicon Nitride probes (MLCT, Bruker, USA), with a spring constant of 0.01 N/m, were used in contact mode, in air, at room temperature. Raw images were corrected by the JPK data processing software using a standard procedure (flatten, planefit and artifact lines caused by the tip attachment and removal). The scale indicating the sample height or deflection was adjusted to limit the gap between high and low regions. Using this software, we measured the cross sections through the images, and we obtained the samples 3D views.

4.4.7 Fixed-cell Staining

Cells were fixed at different time-points: flat and 1 h, 4 h and 24 h after pattern inscription. Cell fixation was performed by incubating cells in a 4% paraformaldehyde solution for 15 minutes. Then, cells were permeabilized with 0.1% Triton X-100 in PBS for 15 min. Samples were blocked in 3% bovine serum albumin in PBS (Sigma-Aldrich) for 1 hour to avoid non-specific binding. FAs were labelled by incubating samples with an anti-paxillin monoclonal antibody (dilution 1: 400) for 1 h at

room temperature or histones were marked by incubating samples with an anti-histone H3(ACK9) in monoclonal antibody (dilution 1: 400) for 1.30 h at room temperature. After incubation, substrates were washed three times with Triton-PBS (3 min per wash) and incubated with Alexa Fluor 546 conjugated goat anti-mouse antibody (dilution 1: 1000) for 1 h at room temperature. Actin filaments were stained by incubating samples with Alexa Fluor 488 phalloidin (dilution 1: 200) for 1 h at room temperature. Finally, cells were incubated for 15 min in DAPI solution (dilution 1:1000) to stain nuclei. Samples were thoroughly rinsed in PBS and placed upside down on the glass. Fluorescent images of FAs and actin bundles were collected with an Axio Observer Z1 confocal microscope (Zeiss, Germany). Samples were excited at 488 nm (phalloidin), 543 nm (paxillin) and 405 (DAPI), and the emissions were collected in the 500-530 nm, 560-610 nm and 420-480 nm ranges, respectively.

4.4.8 AFM for Cell Mechanics

The Young's modulus of the live cells constrained on flat and elongated on patterned substrates were determined by probing the cells with an AFM (JPK NanoWizard II). For this purpose, the probes used were soft silicon nitride cantilevers with a square pyramid tip incorporated at the free end (PNP-DB, NanoWorld, nominal spring constant 0.06 N/m). Spring constants of the cantilevers were measured independently for each experiment. The AFM was mounted on a Zeiss LM 510 confocal microscope to enable coaligning the AFM tip with cells. All probe indentations were performed over the central region of the cell in an area where the nucleus was present by performing a force mapping. Contact between the AFM tip and cell was defined by visually noting when the cantilever deflection deviated from a linear extrapolation of zero force. Force curves were typically recorded at a scan rate of 1 Hz, corresponding to a maximum loading rate of 1 nN/s and a maximum force of 1 nN. Typically, 64 force curves were measured over a cell area of 10 x 10 μm. Five separate experiments were performed on each topography for each timepoint, with 64 force-versus-indentation curves measured from each of ten aligned cells per pitch (indentation speed, 1 μm /s). Mechanical properties of cells, in terms of Young's modulus (E) values were estimated by fitting the force-indentation curve with Hertzian model for linearly elastic materials. The Young's modulus of the hTERT cells on each sample was quantified by calculating the median of the eight values with the greatest distance from the substrate (approximately corresponding to the nucleus).

thirty cells were indented for each time point. The individual elasticity values for a sample were collected via the JPK data processing software providing the distribution of elasticity values. Once collected the data, we used Microsoft Excel in order to compute the average, the median and the standard deviation of each cell's Young's modulus, corresponding to 64 force curves. We consider the points in which the nucleus was visible in order to compute its mechanical properties (the 8 points with the greatest distance from the substrate). Young's moduli at the subsequent times were normalized respect to the elasticity values of the flat specimen (t=0-).

4.4.9 Analysis of FAs, cytoskeleton, and nuclear morphology

Information on cell area, orientation and elongation was obtained by analysing a set of 15 single isolated cells for each timepoint, stained using immunofluorescence techniques. The qualitative study was evaluated on flat and linear pattern. The analysed set of cells came from different samples carried out in analogous conditions, form different patterns inscribed in various regions of the azopolymer thin films. Morphometric analysis was performed using ImageJ software. Cell polarization was assessed from confocal images using the script "analyse particles". This allows to extract information about, area, A/R and shape of the cells, nuclei and FAs. Moreover, cell/nuclei/FAs orientation on linear pattern, was defined as the angle that the principal axis of inertia formed with a reference axis, i.e. the pattern direction in the case of linear or the horizontal axis for flat surfaces. Nucleus volume was calculated via a custom written script in ImageJ. Briefly, Z-stack sections of nuclei were binarized. The area of each section was multiplied by the voxel height (Vh) and the volume was expressed as the sum of the areas*Vh comprising the stack. The (local and global) DAPI intensity mean, the H3K9AC intensity mean and the DAPI spots volume were quantified using Imaris software. For Imaris analysis we collected 15 z-stacks per each sample (sections 0.4). The average, median and standard deviation values of all the parameters listed above were calculated. Statistical significance was assessed through Kruskal-Wallis test (run in Matlab) with level of significance $p < 0.05$.

4.5 References

1. Brock, A. *et al.* Geometric Determinants of Directional Cell Motility Revealed Using Microcontact Printing †. *Langmuir* **19**, 1611–1617 (2003).

2. Théry, M., Pépin, A., Dressaire, E., Chen, Y. & Bornens, M. Cell distribution of stress fibres in response to the geometry of the adhesive environment. *Cell Motil. Cytoskeleton* **63**, 341–355 (2006).

3. Desai, R. A., Gao, L., Raghavan, S., Liu, W. F. & Chen, C. S. Cell polarity triggered by cell-cell adhesion via E-cadherin. *J. Cell Sci.* **122**, 905–911 (2009).

4. Lombardi, M. L. *et al.* The interaction between nesprins and sun proteins at the nuclear envelope is critical for force transmission between the nucleus and cytoskeleton. *J. Biol. Chem.* **286**, 26743–26753 (2011).

5. Pitaval, A., Tseng, Q., Bornens, M. & Théry, M. Cell shape and contractility regulate ciliogenesis in cell cycle–arrested cells. *J. Cell Biol.* **191**, 303–312 (2010).

6. Pouthas, F. *et al.* In migrating cells, the Golgi complex and the position of the centrosome depend on geometrical constraints of the substratum. *J. Cell Sci.* **121**, 2406–2414 (2008).

7. Doyle, A. D., Wang, F. W., Matsumoto, K. & Yamada, K. M. One-dimensional topography underlies three-dimensional fibrillar cell migration. *J. Cell Biol.* **184**, 481–490 (2009).

8. Dupont, S. *et al.* Role of YAP/TAZ in mechanotransduction. *Nature* **474**, 179–183 (2011).

9. Kilian, K. A., Bugarija, B., Lahn, B. T. & Mrksich, M. Geometric cues for directing the differentiation of mesenchymal stem cells. *Proc. Natl. Acad. Sci.* **107**, 4872–4877 (2010).

10. Ingber, D. E., Wang, N. & Stamenović, D. Tensegrity, cellular biophysics, and the mechanics of living systems. *Rep. Prog. Phys.* **77**, 046603 (2014).

11. Vignaud, T. *et al.* Reprogramming cell shape with laser nano-patterning. *J. Cell Sci.* jcs.104901 (2012) doi:10.1242/jcs.104901.

12. Davidson, M. R., Mitchell, S. A. & Bradley, R. H. UV-ozone modification of plasma-polymerised acetonitrile films for enhanced cell attachment. *Colloids Surf. B Biointerfaces* **34**, 213–219 (2004).

13. Rafelski, S. M. & Theriot, J. A. Crawling Toward a Unified Model of Cell Motility: Spatial and Temporal Regulation of Actin Dynamics. *Annu. Rev. Biochem.* **73**, 209–239 (2004).

14. Natansohn, A. & Rochon, P. Photoinduced Motions in Azo-Containing Polymers. *Chem. Rev.* **102**, 4139–4176 (2002).

15. Rossano, L., Cimmino, C., Cavalli, S., Ventre, M. & Netti, P. A. Regulating Fibroblast Shape and Mechanics through Photoresponsive Surfaces with Concentric Circular Topographic Patterns. *Adv. Mater. Interfaces* **5**, 1800890 (2018).

16. Hosseinkhani, H., Hosseinkhani, M. & Kobayashi, H. Proliferation and differentiation of mesenchymal stem cells using self-assembled peptide amphiphile nanofibers. *Biomed. Mater.* **1**, 8–15 (2006).

17. Lee, J., Abdeen, A. A., Wycislo, K. L., Fan, T. M. & Kilian, K. A. Interfacial geometry dictates cancer cell tumorigenicity. *Nat. Mater.* **15**, 856–862 (2016).

18. Heydari, T. *et al.* Development of a Virtual Cell Model to Predict Cell Response to Substrate Topography. *ACS Nano* **11**, 9084–9092 (2017).

Chapter 5

5 Conclusion

The extracellular microenvironment exerts a powerful regulatory effect on cellular mechanics and morphology as well as on stem cell fate decisions. In particular, the delicate balance between cell-matrix interactions and cell geometry plays a key role during embryogenesis. *In vitro*, the characteristics of culture materials that regulate cell adhesion and spreading, including substrate topography, are effective in directing cell behaviour. In particular, cell adhesion phenomena has a direct impact on focal adhesions (FAs) formation, cytoskeleton arrangement, cell contractility and nucleus shape, which altogether affect several cell functions including morphology, proliferation, and gene expression. Therefore, cell adhesion, cytoskeleton assemblies and cell contractility are considered three closely related parameters in which changes in one element invariably induce alterations in the other thus affecting cell behaviour.

In this thesis, we shed light on the design concepts and fabrication technologies that allow the development of engineered platforms capable of delivering spatio-temporal controlled stimuli to study the effects of static and dynamic presentation of adhesive signals on cell morphology, mechanics and nucleus features. More in details, we focused our attention on the evaluation of how the physical properties of the microenvironment, in particular the geometry and nanotopography of the cell substrate, affect the properties of the cytoskeleton assembly that in turn regulate the FAs formation, the polymerization of actin filaments and mainly the nuclear structures and mechanical properties.

To take these issues, in **Chapter I**, we reported the main known effects of soluble and insoluble signals on cell behaviour, together with the applications of biomaterials as a cell culture platform and a brief overview of the main methods to measure nuclear mechanical properties. We highlighted some of the main works in the literature studying the influence of dynamic topographic patterns on cell response and the limitation of proposed static substrates.

Subsequently, in **Chapter II** we focused on the evaluation of stem cell adhesion events in response to static micro- and nanometric topographic stimuli. We exerted a fine control on various aspects of hTERT behaviour by fabricating culturing devices that capture the multiscale complexity of the

extracellular microenvironment, which may in principle affect the adhesion events that ultimately regulate cells function and fate. We used the micropatterning technique to fabricate culture substrates able to exert a constraining action at the cell body level. Four different geometries of adhesive islets were produced (rectangular, elliptical, circular, and square) on either flat or linearly nanopatterned polycarbonate substrates, thus introducing an additional control on adhesion at the receptor, i.e. FA, level. We explored how these micro- and nanotopographical signals dictate and define the formation, spatial positioning, and orientation of FAs, the formation and organization of actin fibres and cytoskeleton. Our results showed that the growth of confined FAs is more evident on nanopatterns, as these limit the adhesion area of FAs and constrain their growth in a specific direction. In this regard, cells cultured on anisotropic adhesive islands formed FAs more aligned and larger in size than those of isotropic shapes, and more specifically FAs formed on nanopatterned substrates appeared more oriented and significantly longer than those on flat substrates. Subsequently, we demonstrated that the structure of the cytoskeleton, influenced by the substrate conditions, defines the magnitude and orientation of tensile forces exerted on the nuclear envelope and together with the signalling proteins of FAs affect the nuclear mechanical properties. Indeed, the anisotropic shapes appeared effective in altering cell mechanics so that the cells showed a stiffer nuclear region. When shape confinement cooperated with FA confinement, the mechanical stability of the cells was disrupted by the presence of the topographic nanopattern, which presumably reduced the space available for FA formation and growth. This event was not observed on rectangular micropatterns where the presence of a coaligned nanopattern induced the formation of parallel FAs and actin bundles that stiffened the nuclear region. Finally, we observed that the forces exerted by the stress fibres on the nuclear envelope influenced the morphology and deformation of the nucleus. Indeed, the nucleus appeared elongated in the anisotropic cells and with an almost rounded morphology in the isotropic cells; moreover, the nuclei were subject to plane/axial contraction (flattening) under all the culture conditions.

Once known the cellular response in an environment displaying static adhesive signals, in **Chapter III** we studied the events of cell adhesion in response to topographic stimuli in a dynamic contest. Since several literature data have provided convincing evidence that cell function and fate are not dictated by a single type of signal, but it is rather a complex interaction of several signals acting on different length and time scales that determines the final cell state, we considered it appropriate to use light-sensitive polymers to fabricate platforms displaying signal arrays whose features can be controlled dynamically. We developed a topography-embossing technique on a micropatterned substrate with a confocal microscope. The technique was effective in superimposing a submicron scale topographic pattern onto a micropatterned surface with well defined, micronscale, adhesive

areas, in a highly versatile, straightforward and rapid manner. We showed how cells sensed topographical signals from their microenvironment and transmitted them to the nucleus to regulate mechanical and morphological properties and gene expression programmes. Our results highlight how biophysical cues in the form of parallel nano-grooves on the surface of cell-adhesive substrates (circular or rectangular adhesion area) impact the properties of the cytoskeleton and nucleus by regulating the dynamic reciprocities between the tension-dependent formation of FAs, the polymerisation of actin filaments, the condensation of chromatin, the stiffening of the nuclear envelope lamina network and the nucleus-cytoplasmic displacement of epigenetic factors.

Based on the results we obtained from the dynamic platform fabrication through confocal microscopy, we further exploited the technique to induce extensive cell shape changes that are expected to dramatically affect cytoskeleton assemblies and nucleus change, thus possibly affecting cell's epigenetic state. Therefore, in **Chapter IV**, we illustrated a novel optical technique capable of imprinting topographic patterns on azopolymer films in a simple way by controlling the position and movement of a focused laser beam. We observed how hTERT cells behaved in a material microenvironment where biophysical properties change over time when moving from a flat to a nanopatterned substrate in terms of changes in alignment, cell shape, mechanical properties and chromatin assembly. In particular, we found an increase in chromatin compaction when the cell elongated demonstrated by both an increase in DAPI fluorescence density and an increase in heterochromatin volume (DAPI spots). In addition, the clear reduction in fluorescence intensity mean of histone in the nucleus, passing from flat to nanopatterned substrates, indicated a reduction in acetylation confirming an increase in chromatin condensation correlated with the stiffening of the nucleus of hTERT cells. Moreover, when the cells were disc-shaped, the chromatin appeared largely extended within a rounded nucleus with a few small, condensed domains located in the centre; in contrast, when the cell became elongated, the nucleus became deformed, and the chromatin tended to condense in the nuclear periphery.

In conclusion, in this work, we demonstrated that by appropriately engineering cell culture substrates, it is not only possible to provide a conceptual picture of the mechanical coupling between cell shape and nuclear shape, but it is also possible to predict nuclear stiffening and different epigenetic responses when the cell elongates.

These data have clearly illustrated that the sequential application of biophysical signals can be a powerful tool for studying dynamic changes in biological processes, an approach that can be useful for studying intrinsically dynamic events such as tissue development, wound healing and disease progression. Moreover, this study could find effective applications to expand stem cell populations

or to guide a homogeneous differentiation or self-renewal in vitro for stem cell-based therapies, for which the spatiotemporal integration of adhesive signals dictates cell functions and fate. Additionally, the results concerning the effect of material signals in changing the epigenetic state could be exploited to describe abnormal nuclear morphology in various diseases such as progeria, cancer, fibrosis, and dilated cardiomyopathy. In the next future, these techniques could eventually replace the effects of small-molecule epigenetic modifiers, offer new ways to maximize the potential of stem cell technologies, and greatly improve the design of next-generation biomaterials. For this purpose, in subsequent studies we could focus on assessing the molecular mechanisms that regulate the transduction of material signals in terms of transcription factor flux and the expression of specific genes. Subsequently, it would be interesting to evaluate the cellular response to multiple shape variations and to investigate whether there will be a “memory effect” of the shape-variation undergone.